NOVEL THEORETICAL AND EXPERIMENTAL FRAMEWORKS FOR MULTISCALE QUANTIFICATION OF ARTERIAL MECHANICS

A Dissertation
Presented to
The Academic Faculty

by

Ruoya Wang

In Partial Fulfillment
of the Requirements for the Degree
Doctor of Philosophy in the
School of Mechanical Engineering

Georgia Institute of Technology
May 2013

NOVEL THEORETICAL AND EXPERIMENTAL FRAMEWORKS FOR MULTISCALE QUANTIFICATION OF ARTERIAL MECHANICS

Approved by:

Dr. Rudolph L. Gleason Jr., Advisor
School of Mechanical Engineering
Department of Biomedical Engineering
Georgia Institute of Technology

Dr. C. Ross Ethier
Department of Biomedical Engineering
Georgia Institute of Technology

Dr. Luke P. Brewster
Department of Vascular Surgery
School of Medicine
Emory University

Dr. Alexander Rachev
School of Mechanical Engineering
Georgia Institute of Technology

Dr. J. Brandon Dixon
School of Mechanical Engineering
Georgia Institute of Technology

Date Approved: November 2, 2012

To my family for all their love and support

ACKNOWLEDGEMENTS

This dissertation encompasses work that was made possible only through the help and support of numerous colleagues, mentors, friends, and family. Foremost, my advisor and mentor, Dr. Rudy Gleason, was instrumental in providing a research atmosphere that highly encouraged independent thinking. Despite his independent approach, Dr. Gleason would always provide consistent encouragements and make time to discuss problems. I would also like to thank the members of my reading committee, Drs. Luke Brewster, Brandon Dixon, Ross Ethier, and Alexander Rachev for taking their time to review and discuss my research. Dr. Brewster was incredibly generous and helpful in providing access to his lab, clinical equipment, conference funds, and numerous insightful discussions. His clinical background has been invaluable in providing relevancy to my research. I would like to thank Dr. Dixon along with Dr. Wan for their help in developing the fiber alignment algorithms used in this study and Dr. Ethier for his biomechanical insights and agreeing to join my committee on a short notice. Finally, Dr. Rachev's incredible knowledge of mechanics was invaluable in helping to develop the theories in this work; his life lessons were a constant source of inspiration.

I would like to thank the staff of IBB at Georgia Tech and Emory University School of Medicine in particular Aqua Ashbury and Haiyan Li for their help with histology and Andrew Shaw for his help with the optical microscopy. I would also like to thank the staff of the mechanical engineering machine shop at Georgia Tech including John Graham, Louis Boulanger, and the countless co-ops that machined the mechanical components used in this study.

All porcine tissues in this study were generous provided by Holifield Farms in Covington, GA. I would like to thank Mr. Holifield and all the workers at the slaughterhouse for their help. I would also like to thank the Yerkes National Primate Research Center for providing primate arteries and the staff members for their help in harvesting the arteries.

I would like to thank all my colleagues that have helped me throughout the years. Past and present members of the Gleason lab in particular Dr. William Wan, Julia Raykin, Laura Hansen, and Alex Caulk. The assistance of Julia Raykin during my experiments has been invaluable. I would also like to thank Swetha Rathan and Dr. Yap Choon Hwai for their help in transporting hearts from the slaughterhouse. Their company made many of the early morning trips to the slaughterhouse much more pleasant. Numerous other graduate and undergraduate students, particularly members of Wing 2A, have made graduate school very enjoyable.

I would like to thank my mom Li, dad Xiao-Jun, and sister Georgia for their love and support. Both of my parents are PhDs and their parental and scientific guidance have helped me throughout graduate school. Finally, my fiancé Jan has been a constant source of love and encouragement throughout the years. She has been incredibly dedicated to the advancement of my career.

TABLE OF CONTENTS

LIST OF TABLES

LIST OF FIGURES

LIST OF SYMBOLS

ψ_o	Longitudinal Closing Angle
ξ_o	Longitudinal Opening Angle
Φ_o	Circumferential Opening Angle
Θ_o	Circumferential Arch Angle
α_o	Longitudinal Arch Angle
ω_i	Residual Shear Angle at the Intimal Surface
Λ	Stretch Ratio: Stress-Free to Traction-Free
λ	Stretch Ratio: Traction-Free to Current
λ^*	Local Stretch Ratio: Traction-Free to Current
C	Compliance
W	Strain Energy Density Function
$\boldsymbol{\sigma}, \mathbf{t}$	Cauchy Stress Tensor
$\mathbf{E}$	Green Strain Tensor
$\mathbf{F_1}$	Deformation Gradient Tensor: Stress-Free to Traction-Free
$\mathbf{F_2}$	Deformation Gradient Tensor: Traction-Free to Current
$\mathbf{F}$	Deformation Gradient Tensor: Stress-Free to Current
$\mathbf{I}$	Identity Tensor
p	Lagrange Multiplier
P	Pressure
$F, f, \mathcal{L}$	Axial Force
ϕ	Axial Twist

γ	Axial Twist Per Unit Traction-Free Length
Υ	Axial Twist Per Unit Stress-Free Length
L_u	Local Unloaded or Traction-Free Axial Length
L_n	Local Natural or Stress-Free Axial Length
ℓ	Loaded or Current Vessel Length
β_n	Natural or Stress-Free Configuration
β_u	Unloaded or Traction-Free Configuration
β_t	Loaded or Current Configuration
β_t	Loaded or Current Configuration
R	Circumferential Stress-Free Radius
S	Longitudinal Stress-Free Radius
ρ	Traction-Free Radius
r	Current or Loaded Radius
d	Current or Loaded Diameter
e	Eccentricity
H	Traction-Free Wall Thickness
p-d	Pressure - Diameter
p-f	Pressure - Force

LIST OF ABBREVIATIONS

ECM	Extracellular Matrix
LADCA	Left Anterior Descending Coronary Artery
CCA	Common Carotid Artery
LOA	Longitudinal Opening Angle
COA	Circumferential Opening Angle
OA	Opening Angle
LCA	Longitudinal Closing Angle
RSA	Residual Shear Angle
RSD	Residual Shear Deformations
LRS	Longitudinal Residual Strain or Stress
CRS	Circumferential Residual Strain or Stress
SRS	Shearing Residual Strain or Stress
SMC	Smooth Muscle Cells
IVUS	Intravascular Ultrasound
TPEM	Two-Photon Excitation Microscopy
FWHM	Full-Width at Half-Maximum
FFT	Fast-Fourier Transform
SD	Standard Deviation
SEM	Standard Error of Means
ANOVA	Analysis of Variance
DPBS	Dulbecco's Phosphate Buffered Saline

CAD	Coronary Artery Disease
H&E	Hematoxylin and Eosin
MT	Masson’s Trichrome
VVG	Verhoeff-Van Gieson
DIC	Digital Image Correlation
VST	Very Soft Tissues
ROI	Region of Interest
PS	Perivascular Support
TF	Traction-Free
SF	Stress-Free
NLO	Non-Linear Optical
SHG	Second Harmonic Generation

SUMMARY

The mechanical behavior of the arterial wall is determined by the composition and structure of its internal constituents as well as the applied traction-forces, such as pressure, axial stretch, and torsion. The purpose of this work is to develop new theoretical frameworks and experimental methodologies to further the understanding of arterial mechanics and role of the various intrinsic and extrinsic mechanically influencing factors. Specifically, residual deformations, matrix organizations, and perivascular support are investigated in the context of their effects on the overall and local mechanical behavior of the artery. New kinematic frameworks for analyzing residual deformations are proposed, distinct microstructural differences between functionally different arteries are found, and the effect of perivascular constriction on the coronary artery is quantified.

The current paradigm for quantifying residual deformations is insufficient and does not fully characterize the artery's stress-free configuration. Residual deformations, an adaptive response of arteries for maintaining intramural mechanical homeostasis, serve as an essential link between the biological and mechanical mechanisms of the artery. Furthermore, arterial constitutive models are formulated with respect to a reference configuration, generally taken to be the artery's stress-free state; identifying this state requires determining the residual deformations. In this work, residual deformations are found to exist in shear and the longitudinal direction of major arteries. New frameworks for the kinematics are proposed to quantify the new residual deformation fields. Stress analyses predict a significant change to the local mechanical

environment of the arterial wall when the new residual deformation frameworks are utilized.

The organization of the structural constituents of the arterial wall, particularly of collagen fibers, serves as an important determinant of an artery's mechanical response. Establishing this relationship between the microstructure and macro-response is fundamentally important in arterial mechanics. The microstructures of two functionally different arteries are examined in this work, the femoral and carotid arteries. These arteries exhibit differences in mechanical responses but similarities in geometry and composition. We found that medial collagen fibers in the femoral arteries are significantly more aligned in the circumferential direction than the fibers of the carotid arteries, corresponding to the direction of strain-stiffening. Furthermore, we found that elastin exhibits uniform transmural distributions in the carotid arteries but are highly concentrated around the external elastic lamina in the femoral arteries. Mechanical testing revealed that the femoral arteries are stiffer across most of the loading regime, but quantitative assays found no differences in the mass content of collagen and elastin between the two arteries. Thus, the difference in the organization of medial collagen between the femoral and carotid arteries may be associated with the difference in their macro-response.

Lastly, we found that adipose perivascular support, which encases nearly all coronary arteries, is a significant source of mechanical constriction on the artery. The perivascular constriction is quantified by comparing the mechanical responses of the coronary artery before and after surgical exposure. Expressed in the context of an adventitial or external pressure, we found that the perivascular constriction can be as high

as 24 mmHg. This constriction reduces the strain-stiffening response of the coronary artery *in-situ* compared to the *in-vitro* mechanical response in which the artery is absent of perivascular support. Furthermore, this constriction indicates that *in-vitro* mechanical testing subjects the artery to a significantly higher transmural pressure than what it experiences *in-situ*, suggesting redesign of *in-vitro* tests for arteries with extensive perivascular support is needed.

CHAPTER 1

INTRODUCTION

Arterial diseases are major contributors of morbidity and mortality worldwide [1]. The successes or failures of various clinical interventions depend on a critical understanding of the mechanical behavior of the artery being treated. For instance, minimizing compliance mismatch [2, 3] and reducing acute overstretching [4-6] in arterial vein grafts during implantation are essential for maintaining long-term patency when treating occlusive peripheral and coronary artery diseases. Overinflation of stents can result in high radial and circumferential stresses, promoting intimal hyperplasia [7] and compromising long-term arterial patency as well. Additionally, the progression of arterial diseases is strongly correlated to changes in the mechanical behavior and properties of the afflicted artery [8-11]. For instance, atherosclerotic arteries exhibit gradual, but pronounced thickening and stiffening of the wall, while aneurysmal arteries exhibit thinning and structural weakening of the wall that can eventually lead to rupture. These mechanical changes are brought on through adaptive and maladaptive biological responses mediated at the cellular and microstructural level [12, 13]. These may include the proliferation of smooth muscle cells (SMC) [14], the increase in production or degradation of critical extracellular matrix (ECM) proteins [15], or the reorganization of the ECM [16]. As a result, multi-scale experimental and theoretical approaches are needed to further the understanding of the arterial mechanical behavior.

An artery's mechanical behavior is determined through both intrinsic and extrinsic physical factors. Intrinsic factors include ones such as the geometry and

composition of the arterial wall, organization and transmural distribution of the ECM constituents, and residual strains. Extrinsic factors consist of the traction forces that act on the artery. These forces are multi-axial and may include luminal pressure, shear force from blood flow, axial stretch, torsion, and perivascular tethering. The intrinsic and extrinsic factors are intricately linked through physical laws. However, in the case of living materials such as arteries, mechanically mediated biological mechanisms play an important role in regulating the mechanical behavior as well. Cells are known to sense and respond to their local mechanical environment [17, 18]. For instance, acute hypertensive arteries initially stiffen due to the strain-stiffening response of the arterial wall, but over time, the artery also increases its stiffness through thickening of the wall and reorganization of the ECM [19, 20].

One of the central aims of arterial mechanics is to quantify the relationship between the extrinsic and intrinsic physical factors through mechanical testing and mathematical modeling. Quantifying all physical factors that may have mechano-biological implications in an artery into a unifying model is foreseeable in the future and will serve as a critical tool for predicting the progression of arterial diseases. Current advancements in microstructurally motivated constitutive models and microstructural imaging have allowed the limited prediction of an artery's macro-level responses based on the microstructural characterization of important ECM constituents such as collagen and elastin [21, 22]. However, gaps of knowledge continue to exist that hinder a more thorough understanding of arterial mechanics, even of healthy arteries.

This study applies a multi-scale approach to investigate overlooked intrinsic and extrinsic mechanically motivating factors that can critically affect the mechanical

behavior of healthy conduit arteries. The successful realization of the study's specific aims establishes fundamental preliminaries that will allow for a more accurate prediction of an artery's mechanical behavior. These specific aims are given below:

Specific Aim 1: Characterize the kinematics of longitudinal and shearing residual deformations in arteries. Our *working hypothesis* is that the stress-free configuration of an artery can be described through independent stress-relieving cuts. The deformations of the stress-relieving cuts can be mapped from the independent stress-free configurations to a single traction-free configuration.

Appropriate determination of the stress-free configuration is fundamentally important when performing stress analysis. The single circumferential opening angle method is widely used to quantify the stress-free configuration in arteries [23]. This method assumes that arterial residual stresses can be relieved through a single cut. We have found evidence to suggest significant residual deformations exist in the longitudinal direction of arteries [24]. Furthermore, we have discovered shearing residual deformations in the coronary arteries, which are subjected to significant axial twists *in-vivo*. These findings suggest that the stress-free state of an artery is more complex then previously thought. A novel kinematic framework that incorporates these novel residual deformations is proposed. Stress analyses are performed to assess the effect of the additional residual deformations on the local mechanical environment of the artery.

Specific Aim 2: Assess differences in matrix microstructural organizations and mechanical responses in non-human primate femoral and carotid arteries. Our *working hypothesis* is that differences in the mechanical behavior between geometrically similar arteries such as primate femoral and carotid arteries can be associated to differences in the microstructural organizations of their ECM.

The femoral and carotid arteries are major conduits for blood flow to peripheral tissue beds. They are known to exhibit differences in mechanical behavior both *in-vivo* and *in-vitro* as well as differences in response to disease and after surgical intervention. However, the matrix composition of the structurally relevant constituents, elastin and collagen, have been shown to be similar between the arteries [25], leading to speculation that differences in their microstructure organization may be responsible for their macro-level mechanical differences. This aim seeks to quantify the microstructure of the femoral and carotid arteries from non-human primates using non-linear optical imaging. In series, biaxial mechanical tests are performed to assess mechanical differences between the arteries. Differences in their collagen and elastin contents and transmural distributions are assessed using quantitative assays and histology, respectively.

Specific Aim 3: Assess the mechanical role of perivascular support in the coronary artery. Our *working hypotheses* are 1) perivascular support significantly constricts the dilation of the coronary arteries when subjected to physiologic loading conditions and 2) *in-vitro* mechanical testing overprescribes the pressure and axial stretch due to a lack of perivascular support, resulting in stiffer mechanical behaviors.

The coronary arteries are deeply embedded in perivascular tissue. Perivascular support has been shown to exert multi-axial constraints on an artery [26-28]. The mechanical effects of these constraints are difficult to quantify experimentally and may be problematic for determining the actual mechanical properties of the artery. In this aim, we seek to measure the pressure-diameter response of the coronary arteries with and without perivascular support *in-situ* in porcine hearts. In series, the arteries are completely freed of perivascular support and mechanically tested *in-vitro* under cylindrical biaxial loading conditions. This allows for the direct assessment of differences between the *in-situ* and *in-vitro* mechanical responses. As a result, this aim not only provides valuable insights into the mechanical environment of the coronary artery with perivascular support, but also helps to design *in-vitro* mechanical tests to more accurately mimic *in-vivo* environments.

Summary

This study investigates three fundamental areas that modulate the mechanical behavior of arteries (**Figure 1.1**). The successful accomplishment of these aims will provide new experimental insights and theoretical frameworks for understanding arterial mechanics in the context of both normal and diseased conditions. The *long-term* goal is to formulate multi-scale models that can describe the mechanical behavior of arteries as well as temporal changes in the mechanics due to disease or normal vascular development.

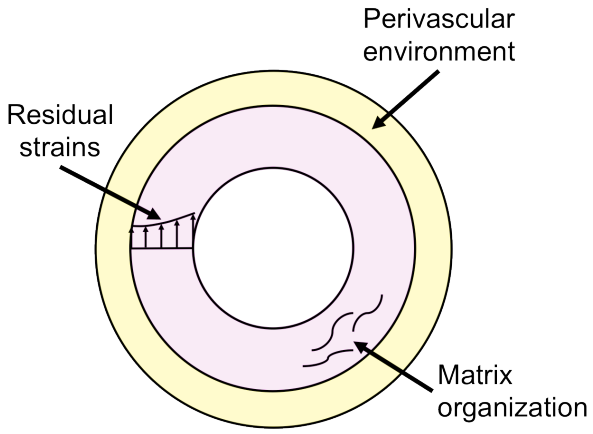

Figure 1.1: Mechanical factors that motivate the aims of this study. These include novel characterization of residual strains, determining the mechanical role of perivascular support, and quantifying the microstructural organization and its effects on macro-level responses.

Background

The Zero-Stress Configuration: Residual Strains and Stresses

An artery without traction forces (i.e., pressure, axial stretch, etc.) is not free of stresses due to the presence of residual strains. Residual strains were observed as early as 1960 by Bergel [29], but it was not until the seminal works by Chuong and Fung [30] and independently with Vaishnav and Vossoughi [31] in 1983 that the importance of arterial residual strains was recognized. Prior to their studies, stress analysis performed on arteries subjected to physiologic loads predicted a large circumferential stress gradient across the arterial wall, with the stress concentration residing along the inner wall [32]. This finding led to a premature assumption that arteriosclerosis was a consequence of prolonged exposure of the wall to this high stress gradient. However, when residual strains were incorporated into the stress analysis, the intramural stress gradient was reduced significantly to a nearly homogeneous level [23]. This finding suggested that under normal conditions and loads, cells situated across the arterial wall experienced the

same mechanical environment. Subsequently, it was shown that perturbation from this homogenous mechanical environment could initiate various growth and remodeling responses aimed at restoring mechanical homeostasis [33-35]. Thus, residual strains serve as a crucial link between the mechanical and biological responses of an artery. The importance of residual strains has been further established in numerous studies that have examined them in various arteries and animals [29, 36, 37]. Residual deformations have been shown to change with various diseases [34, 38, 39] as well as with aging [40-42] (see Rachev and Greenwald [29] for a comprehensive review on vascular residual strains). Furthermore, accurately quantifying residual strains is fundamentally important for establishing a reference configuration when performing stress analysis, since the reference configuration is generally considered to be free of stresses [43].

Quantifying Residual Strains

Destructive cuts are generally required to reveal residual strains. If properly implemented, these cuts allow the material to relieve its stored elastic energy and achieve a stress-free configuration. The corresponding displacement field due to the cut can then be determined by mapping the motions from the stress-free to the traction-free configurations. In vascular mechanics, the single radial cut method on an arterial ring is undoubtedly the most widely used method to reveal residual deformations [23]. In response to the cut, the ring springs open into a nearly circular sector. Although the sector shape is generally agreed to be the stress-free (or nearly stress-free) configuration of the artery, cuts made in the axial and radial directions have revealed additional significant residual deformations [44-47]. Given the important mechano-biological implications of

vascular residual strains and despite numerous studies of the phenomenon, there is a need to ensure that residual deformations are fully captured in order to accurately characterize the stress-free configuration.

The Extracellular Matrix

The arterial wall consists of cells surrounded by an extracellular matrix (ECM). The ECM has numerous functions including but not limited to acting as a: a) structural scaffold for cells, growth factors, proteases, etc.; b) structural conduit for blood flow and nutrient transport; and c) dampener of blood flow pulsations to peripheral tissues and organs such as the brain. The ECM is comprised of numerous proteins and macromolecules (i.e., collagen, elastin, laminin, fibronectin, and proteoglycans [43]) of which collagen and elastin are the mechanically dominant constituents. Although their local mass fractions and organizations can vary throughout the arterial tree [48], in general collagen fibers are organized in a helical arrangement in the adventitia [21, 49] and nearly circumferentially in the media [12, 13]. Elastin is more prominent in the arterial media and is arranged in concentric lamellar units interspaced between concentric layers of SMC [50].

Collagen is the most abundant protein in the body. The high tensile strength of collagen fibers ($E \sim 10^9$ Pa [51] for collagen versus 10^5 for elastin [52]), suggests that collagen serves as the primary load bearing constituent of the arterial wall, particularly at resisting arterial over-dilation at high blood pressures [21]. Elastin imparts compliance to the artery, allowing it to recoil in response to cyclic pulse pressures. At low pressures, collagen fibers are largely undulating and do not contribute significantly to the

mechanical response of the artery (the effect of the presence of undulating collagen fibers on the mechanical behavior is unknown). The low-pressure response is instead dominated by elastin. However, as loading or pressure increases, undulating collagen fibers begin to engage (or straighten) at different loading points, initiating the strain-stiffening response of the artery. As physiological pressures are approached, most collagen fibers become engaged, and the artery stiffens significantly. Compliance can be as high as ~90 %/mmHg $\times 10^{-2}$ at low pressures but decrease to ~5 %/mmHg $\times 10^{-2}$ at physiological pressures (see Chapter 4).

Quantifying the Organization of Collagen Fibers

The mechanical behavior of the arterial wall is highly dependent on the underlying organization of the collagen fibers [53]. Not surprisingly, numerous studies have been devoted to quantifying the organization of collagen fibers. Early experiments largely relied on histological techniques where arterial collagen was stained using picrosirius red. When combined with circular polarized light microscopy and a rotational jig, fiber alignments could be determined based on the direction of polarity. Finlay *et al.* further added techniques of serial sectioning and a 3-axis rotational jig to characterize the 3-dimensional organization of the fibers [54, 55]. However, histology is limited by unknown damage imparted to the tissue during the embedding and sectioning process. Furthermore, as it is a destructive technique, it is not possible to visualize the kinematics of the fibers during loading using histology, important for understanding affine or non-affine fiber deformations [56, 57]. The emergence of non-linear optical (NLO) imaging and second harmonic generation (SHG) imaging of collagen fibers have allowed for non-

destructive 3-dimensional visualizations of the fibers [58, 59]. Furthermore, advanced image processing techniques (i.e., fast Fourier or Hough transform algorithms [60, 61]) have allowed for the automated extraction of fiber angles. Since NLO is non-destructive, the artery can be mechanically tested in parallel or series, thus allowing for multi-scale observations and characterizations of the arterial mechanical behavior.

Modeling Assumptions

In this study, mathematical models are formulated to describe the mechanical behavior of arteries based on physical laws. Confounding factors such as local material heterogeneity, natural variability between specimens, and unknown mechanical interactions cannot be taken into consideration. These models are meant to provide generalized descriptions of the mechanical observations and thus certain assumptions must be made.

We modeled the artery as a thick-walled cylindrical tube composed of an incompressible, orthotropic, homogeneous material undergoing a pseudo-elastic deformation (following appropriate preconditioning cycles) [43]. Mathematical frameworks were developed based on theories of finite elasticity and continuum mechanics. All measurements were made on specimens kept in an isothermal environment at 37 ^{o}C. Furthermore, all measurements were made in the passive state of the artery; vasotone was deactivated using Ca^{+2} and Mg^{+2}-free solutions. Any additional assumptions are described in specific experiments.

References

1. Roger, V.L., et al., *Heart Disease and Stroke Statistics—2011 Update.* Circulation, 2011. **123**(4): p. e18-e209.

2. Abbott, W.M., et al., *Effect of compliance mismatch on vascular graft patency.* Journal of vascular surgery, 1987. **5**(2): p. 376-382.

3. Walden, R., et al., *Matched elastic properties and successful arterial grafting.* Archives of Surgery, 1980. **115**(10): p. 1166.

4. Liu, S., M. Moore, and C. Yap, *Prevention of mechanical stretch-induced endothelial and smooth muscle cell injury in experimental vein grafts.* Journal of biomechanical engineering, 2000. **122**: p. 31.

5. Dobrin, P.B., et al., *Mechanical and histologic changes in canine vein grafts.* Journal of Surgical Research, 1988. **44**(3): p. 259-265.

6. Shuhaiber, J.H., et al., *Mechanisms and future directions for prevention of vein graft failure in coronary bypass surgery.* European journal of cardio-thoracic surgery, 2002. **22**(3): p. 387-396.

7. Timmins, L.H., et al., *Increased artery wall stress post-stenting leads to greater intimal thickening.* Laboratory Investigation, 2011. **91**(6): p. 955-967.

8. Rourke, O., *Mechanical principles in arterial disease.* Hypertension, 1995. **26**(1): p. 2-9.

9. Safar, M., B. Levy, and H. Struijker-Boudier, *Current perspectives on arterial stiffness and pulse pressure in hypertension and cardiovascular diseases.* Circulation, 2003. **107**(22): p. 2864-2869.

10. Safar, M.E., et al., *Arterial mechanics predict cardiovascular risk in hypertension.* Journal of hypertension, 1997. **15**(12): p. 1605-1611.

11. Sonesson, B., T. Sandgren, and T. Lanne, *Abdominal aortic aneurysm wall mechanics and their relation to risk of rupture.* European journal of vascular and endovascular surgery, 1999. **18**(6): p. 487-493.

12. Canham, P.B., et al., *Measurements from light and polarised light microscopy of human coronary arteries fixed at distending pressure.* Cardiovascular research, 1989. **23**(11): p. 973-982.

13. Canham, P., et al., *Medial collagen organization in human arteries of the heart and brain by polarized light microscopy.* Connective tissue research, 1991. **26**(1-2): p. 121-134.

14. Epstein, F.H. and R. Ross, *Atherosclerosis, an inflammatory disease.* New England Journal of Medicine, 1999. **340**(2): p. 115-126.

15. Kuzuya, M. and A. Iguchi, *Role of matrix metalloproteinases in vascular remodeling.* Journal of atherosclerosis and thrombosis, 2003. **10**(5): p. 275.

16. Galis, Z.S., et al., *Targeted disruption of the matrix metalloproteinase-9 gene impairs smooth muscle cell migration and geometrical arterial remodeling.* Circulation research, 2002. **91**(9): p. 852-859.

17. Discher, D.E., P. Janmey, and Y. Wang, *Tissue cells feel and respond to the stiffness of their substrate.* Science, 2005. **310**(5751): p. 1139-1143.

18. Hariton, I., et al., *Stress-driven collagen fiber remodeling in arterial walls.* Biomechanics and Modeling in Mechanobiology, 2007. **6**(3): p. 163-175.

19. Matsumoto, T. and K. Hayashi, *Stress and strain distribution in hypertensive and normotensive rat aorta considering residual strain.* J Biomech Eng, 1996. **118**: p. 62.

20. Armentano, R., et al., *Effects of hypertension on viscoelasticity of carotid and femoral arteries in humans.* Hypertension, 1995. **26**(1): p. 48-54.

21. Holzapfel, G., T. Gasser, and R. Ogden, *A new constitutive framework for arterial wall mechanics and a comparative study of material models.* J Elasticity, 2000. **61**(1): p. 1-48.

22. Gasser, T.C., R.W. Ogden, and G.A. Holzapfel, *Hyperelastic Modelling of Arterial Layers with Distributed Collagen Fibre Orientations.* Journal of the Royal Society Interface, 2006. **3**(6): p. 15-35.

23. Chuong, C. and Y. Fung, *On residual stresses in arteries.* J Biomech Eng, 1986. **108**(2): p. 189-192.

24. Wang, R. and R.L. Gleason, *A Mechanical Analysis of Conduit Arteries Accounting for Longitudinal Residual Strains.* Annals of biomedical engineering, 2010. **38**(4): p. 1377-1387.

25. Benetos, A., et al., *Arterial alterations with aging and high blood pressure. A noninvasive study of carotid and femoral arteries.* Arterioscler Thromb Vasc Biol, 1993. **13**(1): p. 90-97.

26. Steelman, S.M., et al., *Perivascular tethering modulates the geometry and biomechanics of cerebral arterioles.* Journal of biomechanics, 2010. **43**(14): p. 2717-2721.

27. Liu, Y., W. Zhang, and G.S. Kassab, *Effects of myocardial constraint on the passive mechanical behaviors of the coronary vessel wall.* American Journal of Physiology-Heart and Circulatory Physiology, 2008. **294**(1): p. H514.

28. Liu, Y., et al., *Surrounding tissues affect the passive mechanics of the vessel wall: theory and experiment.* American Journal of Physiology-Heart and Circulatory Physiology, 2007. **293**(6): p. H3290.

29. Rachev, A. and S. Greenwald, *Residual strains in conduit arteries.* Journal of biomechanics, 2003. **36**(5): p. 661-670.

30. Fung, Y. and C. Chuong. *Threedimensional stress distributions in arteries*. in *ASME*. 1983.

31. Vaishnav, R.N. and J. Vossoughi, *Estimation of residual strains in aortic segments.* Biomedical engineering II, recent developments, 1983. **2**: p. 330-333.

32. Demiray, H. and R.P. Vito, *A layered cylindrical shell model for an aorta.* International Journal of Engineering Science, 1991. **29**(1): p. 47-54.

33. Matsumoto, T. and K. Hayashi, *Stress and strain distribution in hypertensive and normotensive rat aorta considering residual strain.* Journal of biomechanical engineering, 1996. **118**(1): p. 62.

34. Liu, S. and Y. Fung, *Relationship between hypertension, hypertrophy, and opening angle of zero-stress state of arteries following aortic constriction.* Journal of biomechanical engineering, 1989. **111**(4): p. 325.

35. Humphrey, J., *Vascular adaptation and mechanical homeostasis at tissue, cellular, and sub-cellular levels.* Cell Biochem Biophys, 2008. **50**(2): p. 53-78.

36. Huang, W. and R. Yen, *Zero-stress states of human pulmonary arteries and veins.* Journal of applied physiology, 1998. **85**(3): p. 867-873.

37. Han, H.C., S. Marita, and D.N. Ku, *Changes of opening angle in hypertensive and hypotensive arteries in 3-day organ culture.* Journal of biomechanics, 2006. **39**(13): p. 2410-2418.

38. Zhao, J., et al., *Biomechanical and morphometric properties of the arterial wall referenced to the zero-stress state in experimental diabetes.* Biorheology, 2000. **37**(6): p. 385-400.

39. Lu, X., et al., *Remodeling of the zero-stress state of femoral arteries in response to flow overload.* American Journal of Physiology-Heart and Circulatory Physiology, 2001. **280**(4): p. H1547-H1559.

40. Valenta, J., et al., *Age related constitutive laws and stress distribution in human main coronary arteries with reference to residual strain.* Bio-medical materials and engineering, 2002. **12**(2): p. 121-134.

41. Valenta, J., et al., *Residual strain in human atherosclerotic coronary arteries and age related geometrical changes.* Biomedical Materails and Engineering, 1999. **9**(5/6): p. 311-318.

42. Badreck-Amoudi, A., et al., *The effect of age on residual strain in the rat aorta.* Journal of biomechanical engineering, 1996. **118**(4): p. 440-444.

43. Humphrey, J., *Cardiovascular solid mechanics: cells, tissues, and organs* 2002, New York: Springer Verlag.

44. Greenwald, S., et al., *Experimental investigation of the distribution of residual strains in the artery wall.* J Biomech Eng, 1997. **119**(4): p. 438-444.

45. Vossoughi, J., Z. Hedjazi, and F. Borris, *Intimal residual stress and strain in large arteries.* ASME-PUBLICATIONS-BED, 1993. **24**: p. 434-434.

46. Vossoughi, J. *Longitudinal residual strains in arteries*. 1992.

47. Holzapfel, G.A., et al., *Layer-specific 3D residual deformations of human aortas with non-atherosclerotic intimal thickening.* Annals of biomedical engineering, 2007. **35**(4): p. 530-545.

48. Hayashi, K., et al., *Stiffness and elastic behavior of human intracranial and extracranial arteries.* J Biomech, 1980. **13**(2): p. 175-179, 181-184.

49. Smith, J., P.B. Canham, and J. Starkey, *Orientation of collagen in the tunica adventitia of the human cerebral artery measured with polarized light and the universal stage.* Journal of ultrastructure research, 1981. **77**(2): p. 133-145.

50. Clark, J.M. and S. Glagov, *Transmural organization of the arterial media. The lamellar unit revisited.* Arteriosclerosis, Thrombosis, and Vascular Biology, 1985. **5**(1): p. 19-34.

51. Sasaki, N. and S. Odajima, *Stress-strain curve and Young's modulus of a collagen molecule as determined by the X-ray diffraction technique.* Journal of biomechanics, 1996. **29**(5): p. 655-658.

52. Burton, A., *Relation of structure to function of the tissues of the wall of blood vessels.* Physiol Rev, 1954. **34**(4): p. 619-642.

53. Timmins, L., et al., *Structural inhomogeneity and fiber orientation in the inner arterial media.* Am J Physiol Heart Circ Physiol, 2010. **298**(5): p. H1537-H1545.

54. Finlay, H., L. McCullough, and P. Canham, *Three-dimensional collagen organization of human brain arteries at different transmural pressures.* Journal of vascular research, 1995. **32**(5): p. 301-312.

55. Finlay, H.M., P. Whittaker, and P.B. Canham, *Collagen organization in the branching region of human brain arteries.* Stroke, 1998. **29**(8): p. 1595-1601.

56. Hepworth, D., et al., *Affine versus non-affine deformation in soft biological tissues, measured by the reorientation and stretching of collagen fibres through the thickness of compressed porcine skin.* Journal of biomechanics, 2001. **34**(3): p. 341-346.

57. Billiar, K. and M. Sacks, *A method to quantify the fiber kinematics of planar tissues under biaxial stretch.* Journal of biomechanics, 1997. **30**(7): p. 753-756.

58. Cox, G., et al., *3-dimensional imaging of collagen using second harmonic generation.* Journal of structural biology, 2003. **141**(1): p. 53-62.

59. Wan, W., J.B. Dixon, and R.L. Gleason, *Constitutive modeling of mouse carotid arteries using experimentally measured microstructural parameters.* Biophysical journal, 2012. **102**(12): p. 2916-2925.

60. Nishimura, T. and M. Ansell, *Fast Fourier transform and filtered image analyses of fiber orientation in OSB.* Wood Sci and Technol, 2002. **36**(4): p. 287-307.

61. D'Amore, A., et al., *Characterization of the complete fiber network topology of planar fibrous tissues and scaffolds.* Biomaterials, 2010. **31**(20): p. 5345-5354.

CHAPTER 2

LONGITUDINAL RESIDUAL DEFORMATIONS IN CONDUIT ARTERIES: EXPERIMENTAL AND THEORETICAL FRAMEWORKS*

Introduction

Identification of an appropriate stress-free reference configuration is critically important for providing a reasonable prediction of the intramural stress distributions when performing mechanical analysis on arteries [1-4]. The stress-free state is commonly approximated as a radially cut arterial ring that opens into a nearly circular sector. An opening angle is often used to characterize the shape of this sector. In this study, we present experimental findings that demonstrate significant residual deformations in the longitudinal direction of two conduit arteries, the common carotid artery (CCA) and the left anterior descending coronary artery (LADCA). We suggest that a single radially cut ring is insufficient in achieving the stress-free configuration of an artery. Instead, we propose the use of a longitudinal opening angle (LOA), in combination with the circumferential opening angle (COA), to more appropriately characterize the stress-free configuration of an artery. With the inclusion of longitudinal residual deformations (LRD) in the stress analysis, the predicted circumferential stress gradient decreased by 3-fold while the longitudinal stress gradient increased by 5.7-fold. Thus, the inclusion of LRD has a significant effect on the predicted stress distributions across the arterial wall.

*Modified from [5] with permission from Springer.

The seminal works by Choung and Fung [6, 7] and Vaishnav and Vossoughi [8, 9] recognized the importance of residual strains and the identification of an appropriate stress-free reference configuration when performing stress analysis on arteries. They showed that incorporating residual strains using the single radial cut method into the stress analysis served to reduce the circumferential stress gradient across the arterial wall to a homogenous level. Thus, this prediction suggested that cells situated at different locations across the arterial wall experienced the same mechanical environment. Although the single radial cut method may not relieve all residual stresses, it is generally accepted that this method is sufficient in approximating the stress-free configuration of an artery [10], and is therefore widely used in the field of vascular mechanics [11].

There has been evidence to suggest that residual strains can also exist along the axial (or longitudinal) direction of an artery, putting into question the use of only a single opening angle in describing the stress-free configuration. In fact it was Vossoughi [12] that first determined these longitudinal residual strains (LRS) in the bovine aorta through the curling of rectangular strips cut from the vessel. He noted that when cut out, these strips curled away from the lumen, signifying compression along the inner wall and tension along the outer wall in the artery's traction-free state. By calculating the ratio of the arc lengths of the stress-free intima to the undeformed length of the rectangular strip, he reported an intimal engineering strain of 6%. Holzapfel *et al.* [13, 14] investigated 3-dimensional residual deformations in strips of intact and mechanically separated intima, media, and adventitia from human aortas with non-atherosclerotic intimal thickening. They noted that in the longitudinal strips, the media curled away from the lumen while the intima and adventitia remained flat, indicating LRS was localized to the media layer.

The curling was found to be non-circular; therefore they measured the local curvatures along the curled strips to quantify the deformation. They concluded that a single opening angle parameter was insufficient in describing the 3-dimensional residual deformations of arteries.

In this study, we measured LRD and CRD in healthy porcine coronary and carotid arteries. We found that the LRD exhibited similar characteristics to the previous studies [12, 13]. In addition, we determined that if short longitudinal strips were cut, nearly circular sectors could be achieved, allowing the use of an opening angle to quantify the deformations (**Figure 2.1**). We hypothesize that COA and LOA can be measured from independent stress-relieving cuts taken from the circumferential and longitudinal directions, respectively. The deformations from these independent cuts can then be mapped to a single traction-free configuration.

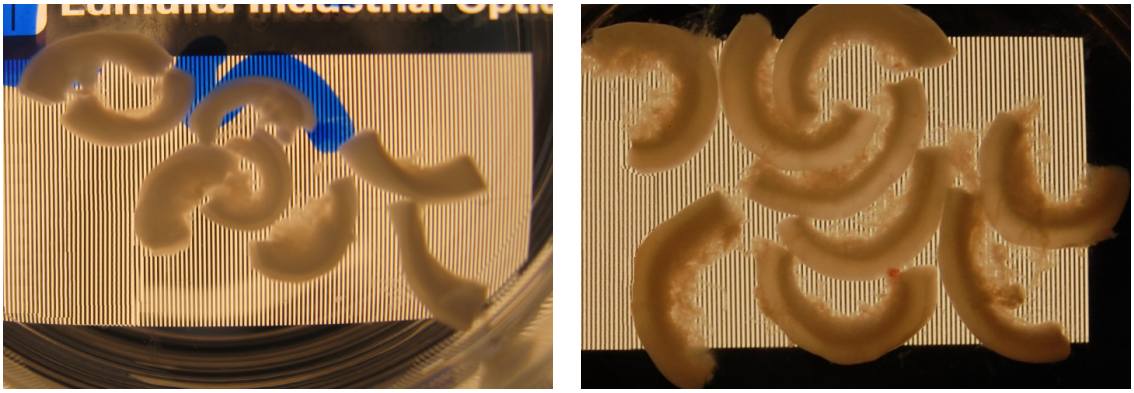

(**A**) (**B**)

Figure 2.1: LRD in the coronary and carotid arteries. These longitudinal stress-free sectors from (**A**) a coronary artery and (**B**) a carotid artery were taken circumferentially around the arteries at one axial location. All sectors are bending away from the lumen (the intima is the smooth side). Note that the sectors are nearly circular and are similar in shape to circumferential stress-free sectors. Out-of-plane warping in some of the coronary artery sectors suggests the presence of residual shear strains. The pictures were taken over a calibration slide.

Methods

Tissue Harvest and Preparation

In this study we measured the COA and LOA in the LADCA (n = 6) and CCA (n = 6) of the pig. An additional CCA was used for cylindrical biaxial mechanical testing to estimate material parameters and calculate the intramural wall stresses using the newly developed kinematics. Hearts weighing 0.76 ± 0.10 kg (mean ± SD) and CCA were obtained at a local abattoir (Holifield Farms, Covington, GA) from normal farm pigs (2 – 3 years of age, 150 – 200 kg in weight) immediately following exsanguination. Following the removal of the heart from the animal, the left coronary vasculature was flushed with ice-cold Mg^{2+} and Ca^{2+}-free Dulbecco's phosphate buffered saline (DPBS) through the coronary sinus. The CCA were rinsed with DPBS to remove the blood. The samples were transported back to the laboratory on ice, upon which the LADCA were carefully dissected out of the heart and the CCA were cleared of adherent perivascular tissues. The arteries were then circumferentially sectioned into 12 LADCA segments and 16 CCA segments per artery. The lengths of these cylindrical segments alternated between long (7.2 mm for LADCA, 9.1 mm for CCA) and short (3.0 mm in length for both LADCA and CCA). Thin longitudinal strips were then cut around each long segment, resulting in 5 to 6 strips for the LADCA and 7 to 9 strips for the CCA (**Figure 2.2**). The time between slaughterhouse and final sectioning did not exceed 5 hrs.

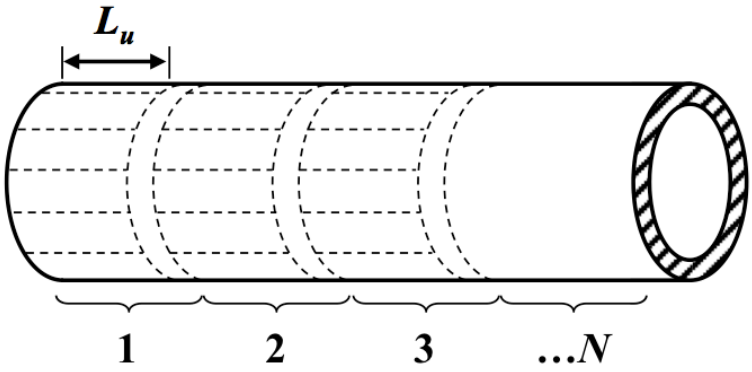

Figure 2.2: **Schema of the sectioning protocol.** Each section 1, 2, 3, …*N*, consisted of longitudinal strips of length L_u ($N = 6$, $L_u = 7.2$ mm for LADCA and $N = 8$, $L_u = 9.1$ mm for CCA) cut circumferentially around the artery and one circumferential ring 3 mm wide. The number of longitudinal strips per section varied between 5 to 6 for the LADCA and 7 to 9 for the CCA. The section numbers increase with the direction of flow.

The lengths of the longitudinal strips were optimized so that the sectors could achieve a nearly circular shape without the ends closing or overlapping. The LOA was averaged for all the sectors around one section; therefore circumferential variations of the LOA were not recorded. A total of 226 longitudinal strips and 36 circumferential rings were cut from the LADCA and 367 strips and 46 rings were cut from the CCA.

Opening Angle Measurements

The longitudinal strips and circumferential rings were placed in DPBS at 37 ^{o}C. Images of the rings were collected after 30 mins with a CCD camera to quantify their traction-free configuration (i.e., outer radius and wall thickness). A single radial cut was then made on the rings allowing them to spring open into sectors. These sectors, along with the deformed longitudinal sectors, were further incubated for 3 hrs allowing them to reach a state of geometric equilibrium after which the sectors were photographed. To

ensure proper dimensional calibration, all sectors were photographed with a calibration slide in view.

The opening angle has been defined previously as an angle that increases in response to a stress-relieving cut. The COA (Φ_0) is the angle between two lines that bisect the midpoint of the inner sector wall and extend to the inner edges of the circumferential sector (**Figure 2.3, left panel**) [15]. In the longitudinal direction, we define an analogous longitudinal closing angle (LCA), ψ_o, as an angle that decreases or 'closes' in response to a stress-relieving cut (**Figure 2.3, right panel**). The longitudinal opening angle (LOA, ξ_0) is therefore:

$$\xi_0 = \pi - \psi_0 \tag{2.1}$$

Note that the magnitude of the LOA varies depending on the length of the longitudinal strip. Assuming minimal axial variations, the LOA increases with increasing length of the undeformed axial strip. Although a length-independent measurement, such as curvature, may be used to quantify the shape of the sectors, we believe that the kinematics may be more clearly understood using the opening angle approach.

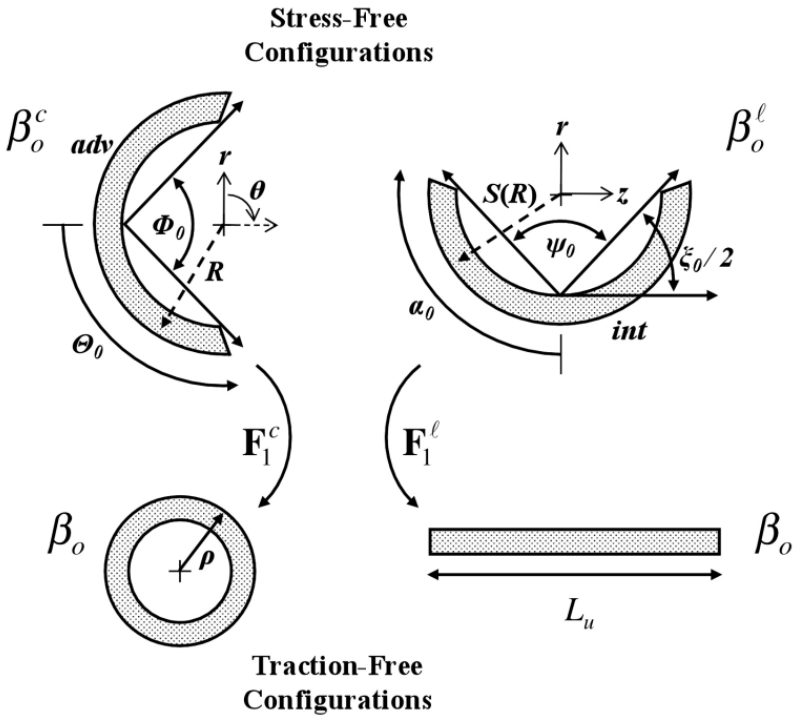

Figure 2.3: Mapping the deformations from the stress-free to the traction-free configurations. Mapping from the experimentally tractable, nearly stress-free configurations β_o^c and β_o^ℓ to traction-free configuration is accomplished by deformation gradient tensors $\mathbf{F}_1^c$ and $\mathbf{F}_1^\ell$. The stress-free configurations consist of a circumferential sector described by radius R, opening angle Φ_o or arc angle Θ_o and a longitudinal sector described by radius $S(R)$, closing angle ψ_o, opening angle ξ_o, or arc angle α_o. The traction-free configurations consist of a circumferential ring of radius ρ and a longitudinal strip of length L_u. The adventitia (*adv*) and intima (*int*) surfaces for the stress-free configurations are labeled accordingly.

The geometry of the stress-free configurations was measured using a custom MATLAB (MathWorks) routine. First, points along the intima and adventitia boundaries were manually selected. These boundary points were then used to calculate the inner and outer arc lengths as well as the cross-sectional area of the vessel wall. Determining the COA and LCA from the bisecting midpoint angle is subjective due to the user selection of the midpoint location at the inner wall, particularly in sectors that are not circular. Since the adventitia and intima are clearly defined in the images, we use the arc lengths

of these boundaries and the cross-sectional area of the wall to calculate a less user-subjective COA and LCA using the following equation (2.2):

$$\text{COA, LCA} = \pi - \frac{L_o - L_i}{2t}, \qquad t = \frac{2A}{L_o - L_i} \tag{2.2}$$

where A is the cross-sectional area of the wall, $L_o$and L_i are the outer and inner arc lengths, respectively, and t is the wall thickness. Note that L_o is the arc length of the adventitia in circumferential sectors and the intima in longitudinal sectors.

Mechanical Testing

Cylindrical biaxial mechanical testing was performed on one CCA. In brief, the artery was pressurized quasi-statically from 0 to 120 mmHg at axial stretches of λ_z = 1.4, 1.5, and 1.6. At each axial stretch, the artery was preconditioned with four pressurization cycles to achieve repeatable loading – unloading curves. Two pressure transducers (FPG, Honeywell, 5 psig 0.1% accuracy) measured the distal and proximal pressures. Axial force was measured with a force transducer (XLU68f, Delta Metrics, 5 lbs 0.1% accuracy) and diameter was monitored with a CMOS digital video camera (F131B, Allied Vision, 1280 × 1024 resolution). Data collection and device control was performed through a data acquisition unit (USB6259, National Instruments) connected to a personal computer running a custom LABVIEW routine (National Instruments).

Statistical Analysis

Experimental results were analyzed with one-way analysis of variance between groups (ANOVA), with results being judged statistically significant if $P < 0.05$. In conjunction with ANOVA, we utilized post-hoc Tukey's test, accounting for multiple

comparisons, to determine which means were statistically different. Student's *t*-test was used to analyze for significance between two means. Data is provided as mean ± SD.

Theoretical Framework

Kinematics

Consider a local neighborhood κ_t about a point with position $\mathbf{x}(r, \theta, z)$ in the loaded configuration β_t. Let this neighborhood be denoted κ_n in the locally stress-free (or natural) configuration β_n, which has position $\mathbf{X}_n(R_n, \Theta_n, Z_n)$ (**Figure 2.3**). Let the gradient of the map $\mathbf{X}_n(R_n, \Theta_\mathrm{n}, Z_n) \mapsto \mathbf{x}(r, \theta, z)$ be denoted $\mathbf{F}$. The natural configuration β_n is defined such that the local neighborhood about every point in the body is stress-free; in general, this configuration may be thought of as a set of discontinuous elements (**Figure 2.4**). Note that β_n is not experimentally tractable. It is often convenient to decompose the map $\mathbf{X}_n(R_n, \Theta_\mathrm{n}, Z_n) \mapsto \mathbf{x}(r, \theta, z)$ into a map from $\mathbf{X}_n(R_n, \Theta_\mathrm{n}, Z_n) \mapsto \mathbf{p}(\rho, \vartheta, \zeta)$ and a map from $\mathbf{p}(\rho, \vartheta, \zeta) \mapsto \mathbf{x}(r, \theta, z)$, where $\mathbf{p}(\rho, \vartheta, \zeta)$ is the location of this material point in the traction-free (unloaded) configuration β_u; let the gradient of these maps be $\mathbf{F}_1$ and $\mathbf{F}_2$, respectively, where:

$$\mathbf{F} = \mathbf{F}_2 \cdot \mathbf{F}_1 \tag{2.3}$$

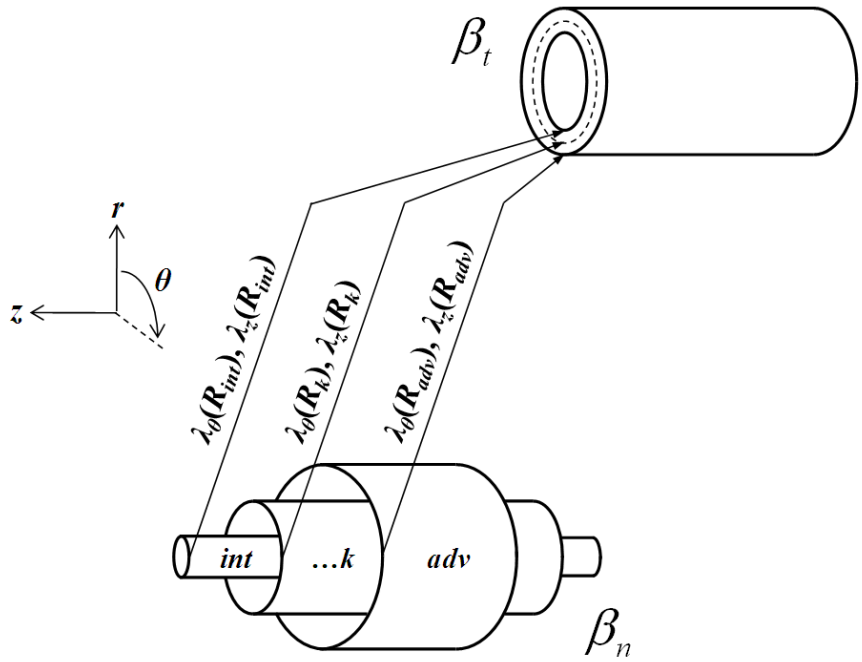

Figure 2.4: Mapping of theoretical stress-free state $\boldsymbol{\beta_n}$ to traction-free state $\boldsymbol{\beta_t}$. Each shell is infinitesimally thin and therefore stress-free. Circumferential and longitudinal residual strains develop as a result of circumferential and axial incompatibilities of the cylindrical shells as they are mapped to the traction-free state.

For the inflation and extension of a long, straight, axisymmetric tube, neglecting variations along the axial direction, the gradient of the map $\mathbf{p}(\rho, \vartheta, \zeta) \mapsto \mathbf{x}(r, \theta, z)$ is:

$$[\mathbf{F}_2] = diag\left\{\frac{\partial r}{\partial \rho}, \frac{r}{\rho}, \lambda_z\right\} \tag{2.4}$$

where $\lambda_z = \ell / L_u$ is the axial stretch ratio, ℓ is the local current length of the artery, and L_u is the local traction-free length of the artery (**Figure 2.2**).

For a straight, axisymmetric tube, neglecting variations along the axial direction, since each material point at a given radius r has the same deformation gradient, β_n may be thought of as a set of discontinuous cylinders with radius R_n, axial length L_n, and infinitesimal thickness dR_n. Since each ring is infinitesimally thin, they cannot support a residual stress; thus, each cylinder is stress-free. The map from $\mathbf{X}_n(R_n, \Theta_n, Z_n) \mapsto$

$\mathbf{p}(\rho, \vartheta, \zeta)$ serves to 'assemble' the discontinuous stress-free cylinders into a continuous, albeit residually stressed, tube; the gradient of this map may be defined as:

$$\mathbf{F}_1 = diag\{\Lambda_r(\rho), \Lambda_\theta(\rho), \Lambda_z(\rho)\} \tag{2.5}$$

where $\Lambda_r(\rho), \Lambda_\theta(\rho),$ and $\Lambda_z(\rho)$ are the stretch ratios of the infinitesimally thin cylinder that passes through point ρ in β_u. If the stress-free configuration is known, then these stretch ratios may be calculated as:

$$\Lambda_\theta(\rho) = \frac{\rho}{R_n(\rho)}, \quad \Lambda_z(\rho) = \frac{L_u}{L_n(\rho)}, \quad \text{and} \quad \Lambda_r(\rho) = \frac{\partial \rho}{\partial R_n} = \frac{R_n(\rho) L_n(\rho)}{\rho L_u} \tag{2.6}$$

where $R_n(\rho)$ and $L_n(\rho)$ are the radius and axial length of the stress-free cylinder in β_n that passes through radial location ρ in β_n, respectively. Since $R_n(\rho)$ and $L_n(\rho)$ are not measurable, experimentalists are forced to approximate the components of $\Lambda_r(\rho), \Lambda_\theta(\rho),$ and $\Lambda_z(\rho)$ from experimentally tractable quantities.

In traditional vascular mechanics, one typically considers an experimentally-measurable (nearly) stress-free configuration β_o^c taken as an excised arterial ring that springs open when cut radially to relieve a large part of the residual stress (**Figure 2.3**; see [16]). The mapping of points $\mathbf{X}_o^c(R, \Theta, Z) \mapsto \mathbf{p}(\rho, \vartheta, \zeta)$ from β_0^c to β_u is defined as $\rho = \rho(R)$, $\vartheta = (\pi/\Theta_o)\Theta$, and $\zeta = \overline{\Lambda}_z Z$. Given this map, the deformation gradient $\mathbf{F}_1^c$, has the components:

$$\mathbf{F}_1^c = diag\left\{\frac{\partial \rho}{\partial R}, \frac{\pi \rho}{\Theta_o R}, \overline{\Lambda}_z\right\} \tag{2.7}$$

The mean axial stretch ratio $\overline{\Lambda}_z$ is assumed to be constant. That is, the changes in axial stretch with radial location are ignored in this configuration and the configuration β_0^c is assumed to be a cylindrical sector (with straight side walls). The incompressibility constraint requires that:

$$R(\rho) = \sqrt{\frac{\pi\overline{\Lambda}_z}{\Theta_o}(\rho^2 - \rho_i^2) + R_i^2} \tag{2.8}$$

It is clear, however, that when thin longitudinal strips are cut from arteries, these strips bend to relieve LRS. The mapping of points $\mathbf{X}_o^\ell(R, \Theta, S) \mapsto \mathbf{p}(\rho, \vartheta, \zeta)$ from β_0^ℓ to β_u is defined as $\rho = \rho(S)$, $\vartheta = \overline{\Lambda}_\Theta \Theta$, and $\zeta = 2\alpha_o S$ (**Figure 2.3**). Given this map, the deformation gradient $\mathbf{F}_1^\ell$, has the components:

$$\mathbf{F}_1^\ell = diag\left\{\frac{\partial\rho}{\partial S}, \overline{\Lambda}_\Theta, \frac{L_u}{2\alpha_o S}\right\} \tag{2.9}$$

where α_o is the longitudinal arc angle, S the radius of curvature for the axial strip after bending, and variations in the 'circumferential' stretch ratio are neglected; thus, the local circumferential stretch ratio is taken as the mean circumferential stretch $\overline{\Lambda}_\Theta$. Furthermore, the incompressibility constraint requires that:

$$S(\rho) = \sqrt{\frac{\overline{\Lambda}_\Theta L_u}{\alpha_o}(\rho - \rho_i) + S_i^2} \tag{2.10}$$

Note that CRS and LRS can coexist along the arterial tree. One consequence of this is that neither a cylindrical sector (β_o^c) representing a radially cut ring nor a cylindrical sector representing a curved longitudinal strip (β_o^ℓ) accurately represents a truly stress-free configuration. Indeed, when both circumferential and longitudinal residual strains are present, an experimentally tractable stress-free configuration does not exist. Rather, a traction-free sector deforms into a saddle shape, which is residually stressed (**Figure 2.5**).

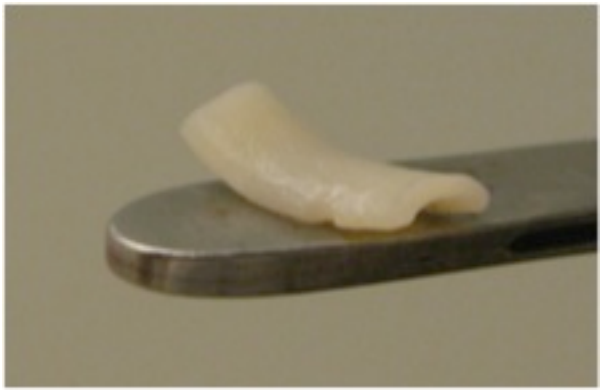

Figure 2.5: A saddle shape is created due to the colocalization of CRS and LRS in a carotid artery. Although not residually stress-free, this shape clearly demonstrates the combined effects of CRS and LRS. The shorter axis aligns with the longitudinal direction, while the longer axis aligns with the circumferential direction.

Nevertheless, when the ratio of circumferential arc length to axial arc length is small (e.g., for a thin axial strip) the axial bending is only negligibly affected by the CRS. Thus, a thin axial strip may be used to quantify the axial stretch $\Lambda_z(\rho)$ from equation (2.6). Similarly, when this aspect ratio becomes large (e.g., for a thin radially-cut ring), circumferential bending is only negligibly affected by longitudinal residual strains. Thus, a thin radially-cut ring may be used to quantify the circumferential stretch $\Lambda_\Theta(\rho)$ (as done by [16]). Taken together, we may approximate the components of $\mathbf{F}_1$ as:

$$\Lambda_\theta = \frac{\pi\rho}{\Theta_o R(\rho)}, \quad \Lambda_z = \frac{L_u}{2\alpha_o S(\rho)}, \text{ and } \Lambda_r = \frac{\partial\rho}{\partial R_n} = \frac{(\Theta_o R(\rho))(2\alpha_o S(\rho))}{\pi\rho L_u} \tag{2.11}$$

where $R(\rho)$ and $S(\rho)$ are given in equations (2.8) and (2.10) respectively. The radial component is calculated assuming incompressibility, with $\Lambda_r\Lambda_\theta\Lambda_z = 1$. The incompressibility constraint also requires that:

$$\int_{\rho_i}^{\rho} \frac{\rho}{R(\rho)S(\rho)}\, d\rho = \frac{2\Theta_o\alpha_o}{\pi L_u}\int_{R_i}^{R} dR_n \tag{2.12}$$

which may be solved with numerical integration techniques.

Stress Analysis

We modeled the artery as a thick-walled cylindrical tube composed of an incompressible, orthotropic, homogeneous material undergoing an elastic deformation of inflation and axial extension. The material property is approximated using a seven-parameter exponential-type strain energy density function by Chuong and Fung [16] given as:

$$W(\mathbf{E}) = \frac{c_0}{2}(e^Q - 1) \tag{2.13}$$

where $\mathbf{E} = \frac{1}{2}(\mathbf{F}^T\mathbf{F} - \mathbf{I})$ is the Green strain tensor, $\mathbf{I}$ is the identity tensor, and the exponential factor is given by:

$$Q = c_1E_{rr}^2 + c_2E_{\theta\theta}^2 + c_3E_{zz}^2 + 2c_4E_{\theta\theta}E_{rr} + 2c_5E_{\theta\theta}E_{zz} + 2c_6E_{zz}E_{rr}$$

The general Cauchy stress relationship is given by:

$$\mathbf{t} = -p\mathbf{I} + \mathbf{F}\cdot\frac{\partial W(\mathbf{E})}{\partial \mathbf{E}}\cdot\mathbf{F}^T \tag{2.14}$$

where p is the Lagrange multiplier that enforces incompressibility [17]. From equilibrium, luminal pressure and axial force are given by:

$$P_i = \int_{r_i}^{r_a}(t_{\theta\theta} + t_{rr})\frac{1}{r}dr \quad \text{and} \quad f = \pi\int_{r_i}^{r_a}(2t_{zz} - t_{rr} - t_{\theta\theta})\,rdr \tag{2.15}$$

A nonlinear least-square fitting algorithm is implemented in MATLAB using `lsqnonlin` function (Levenberg-Marquardt optimization algorithm) to solve for the material constants by minimizing the error between the theoretical and experimental pressure and force data [17].

Results

LADCA Opening Angles

LRD was present in all sections of the LADCA (**Figure 2.6A**). The LOA increased with increasing section number; statistical significance was observed between sections 1 and 6 (*$P < 0.05$). In one vessel, a negative LOA was observed at section 1 (plus symbol) indicating that the sector curled into lumen; all other sections curled into the adventitia. No statistically significant trends were observed in the COA measurements (**Figure 2.6B**).

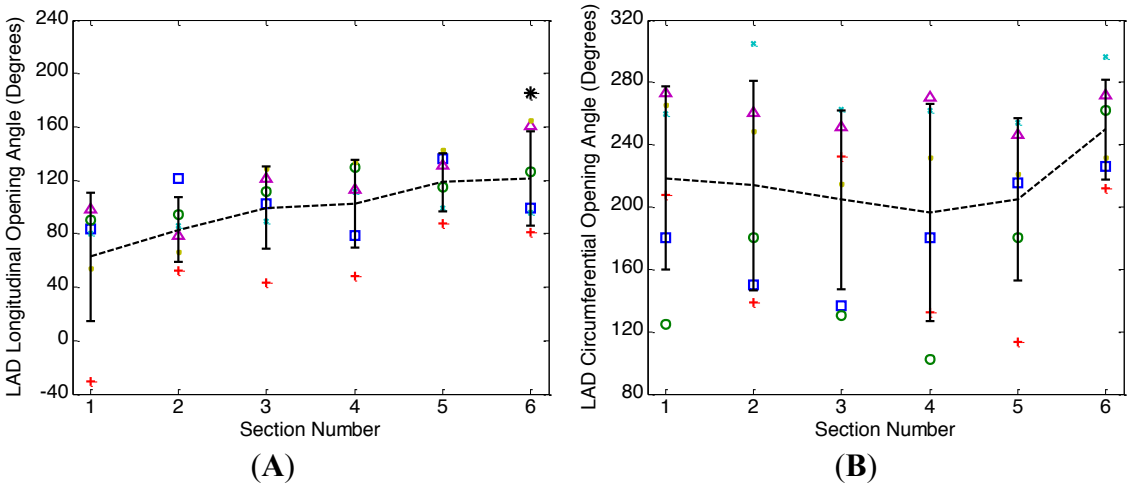

Figure 2.6: LOA and COA measurements from the coronary arteries. (**A**) The LOA exhibits an increasing trend with section number (*$P < 0.05$ for section 6 compared to 1). (**B**) No significant trends are found in the COA measurements. Each symbol type represents a single artery.

CCA Opening Angles

In the carotid arteries, LOA were nearly absent in the first two sections but appeared at section 3 and increased significantly thereafter, achieving a maximum value of ~90^{o} at section 8 (**Figure 2.7B**).

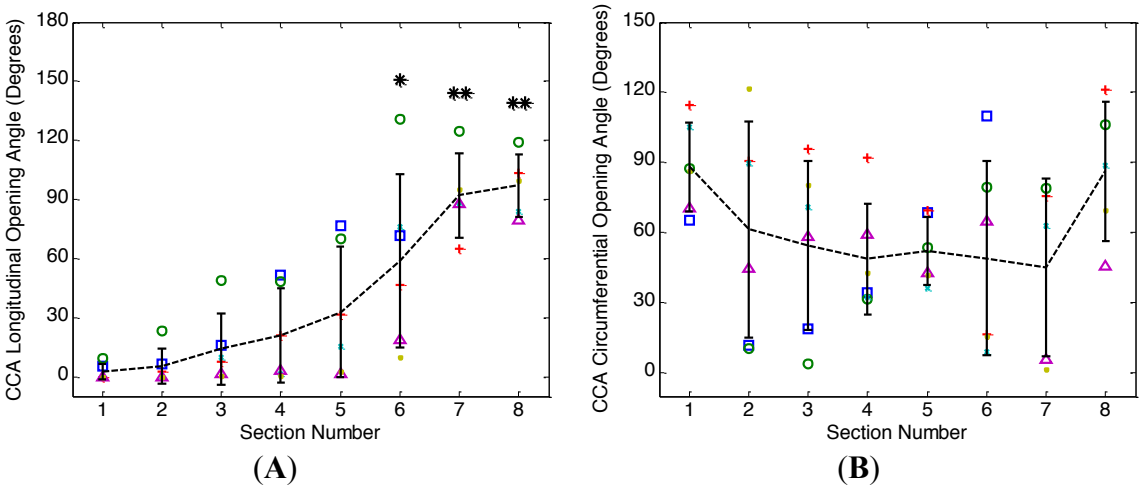

Figure 2.7: LOA and COA measurements from the carotid arteries. (**A**) The LOA increases significantly from nearly zero to 90° with increasing section numbers (*P < 0.05 compared to sections 1, 2, and 3 and **P < 0.001 compared to sections 1, 2, 3, and 4). (**B**) No significant trends exist in the COA measurements.

Thickness

The LADCA and CCA wall thicknesses were measured from the traction-free rings. Both LADCA and CCA thicknesses decreased with increasing section numbers (**Figure 2.8**).

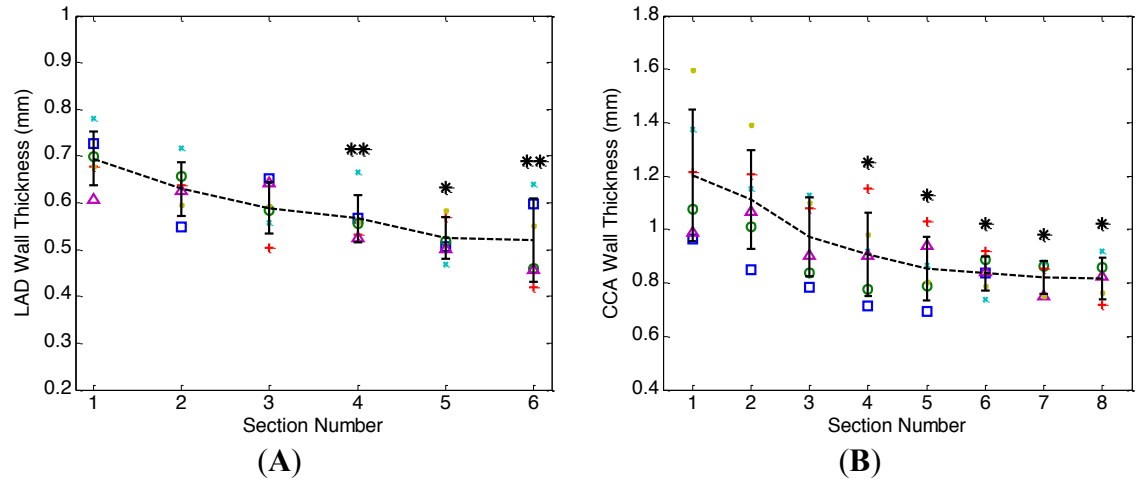

Figure 2.8: Wall thickness in the LADCA and CCA. In both the LADCA (**A**) and CCA (**B**), the wall thickness decreases with increasing section numbers (*P < 0.05 and **P < 0.001 compared to section 1 for LADCA and CCA).

Stress Analysis

The traction-free inner and outer radii from the artery used for the stress-analysis were ρ_i = 2.18 mm and ρ_a = 3.46 mm, respectively. The segment length was L_u = 10.1 mm. The inner radius of the circumferential stress-free sector was R_i = 4.43 mm and the inner radius of the longitudinal stress-free section was S_i = 5.34 mm. The COA and LOA were $\Phi_o = 79.4^{o}$ and ξ_o = 117.9^{o}, respectively, corresponding to a segment between sections 7 and 8 (**Figure 2.7**). Measurements were made on a ring cut from the location where diameter was monitored during mechanical testing. The LRS measurements were taken on strips cut adjacent to the ring. All stress-free geometry measurements were collected following mechanical testing. The unloaded length of the vessel measured suture to suture was 26 mm. The estimated *in-vivo* axial stretch was λ_z = 1.5; in agreement with literature value of the porcine CCA [18]. The thickness was larger than that of the nominal CCA. The mean circumferential ($\overline{\Lambda}_\Theta$) and axial ($\overline{\Lambda}_z$) stretch ratios were assumed to be 1.

The stretch ratios without LRS (i.e., diagonal components of the deformation gradient $\mathbf{F_1^c}$) agreed with results of Choung and Fung [16], $\Lambda_z = 1$. Inclusion of LRS dramatically altered the stretch ratios (**Figure 2.9**). Most notably, the altered longitudinal stretch ratio exhibited a transmural variation from a compressive inner wall to a tensile outer wall. This agreed intuitively with the bending of a longitudinal circular sector into a straight beam. The bending would require that the top of the beam (outer wall) to be under tension and the bottom (inner wall) to be under compression.

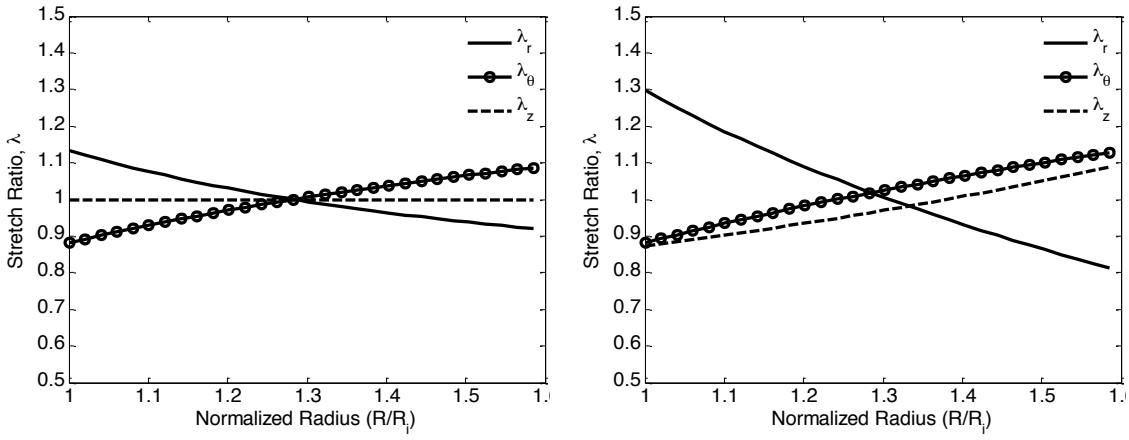

Figure 2.9: Distributions of stretches through the arterial wall in the traction-free configuration. (**A**) Transmural variations without LRS. (**B**) Accounting for LRS alters the stretch distributions, with the inner portion of the wall now under compressive stretch and outer wall under tensile stretch.

Material parameters were solved by regression analysis without LRS (− LRS) and with LRS (+ LRS); results are given in **Table 2.1**. The Fung model achieved good fits to the experimental data. The error is defined as the difference between the model and experimental values normalized to the latter.

Table 2.1: Material parameters determined through non-linear regression fitting of the experimental data.

	c (kPa)	c_1	c_2	c_3	c_4	c_5	c_6	% Error
− LRS	93.37	1.075	0.452	0.612	0.491	0.248	0.416	3.27
+ LRS	137.93	1.019	0.350	0.518	0.463	0.232	0.438	3.49

In the circumferential direction, the stress gradient without LRS was $\Delta t_{\theta\theta}$ = 73.6 kPa and with LRS was $\Delta t_{\theta\theta}$ = 23.9 kPa, a 3-fold reduction (circular markers, **Figure 2.10**). In the longitudinal direction, with LRS resulted in Δt_{zz} = 28.8 kPa and without

LRS resulted in Δt_{zz} = 163.7 kPa, a 5.7-fold increase in the longitudinal stress gradient (dashed lines, **Figure 2.10**).

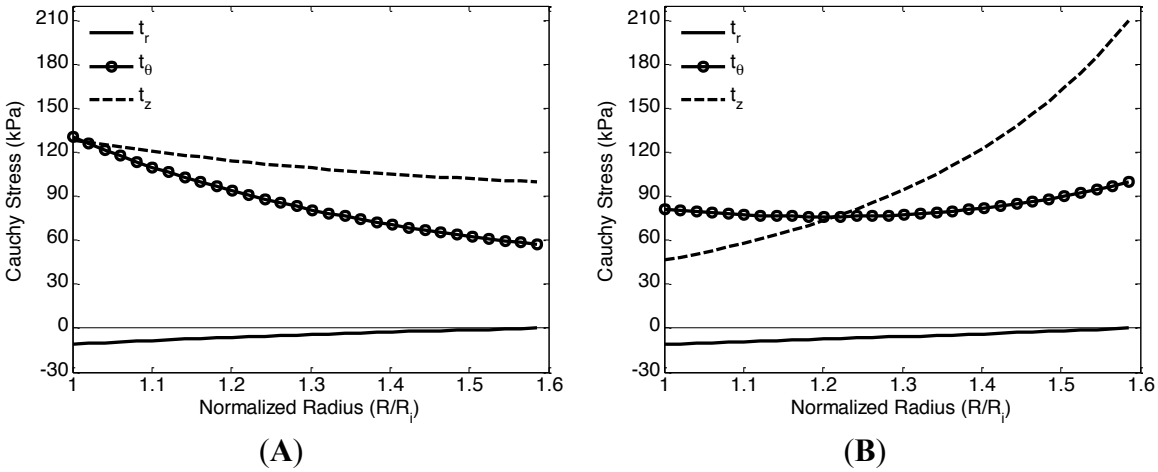

Figure 2.10: Predicted wall stress distributions of the carotid artery. Stresses are calculated at P_i = 120 mmHg and λ_z = 1.5 without (**A**) and with (**B**) LRS. LRS reduces the circumferential stress gradient, however the longitudinal stress gradient is dramatically increased.

Discussion

Numerous studies have demonstrated that vascular cells possess a remarkable ability to sense and respond to changes in their local mechanical environment (e.g., [19, 20]). These mechano-biological mechanisms play a key role in many physiological and pathophysiological processes, as well as the success or failure of many clinical interventions. Fundamental to quantifying mechanically mediated biological mechanisms is the quantification of the local mechanical environment within tissue and how this mechanical environment evolves as the tissue grows and remodels [21-23]. Whereas universal solutions (e.g., Laplace's law) may be used to determine the mean stresses within a tissue, stress analysis is required to predict the local stresses within a tissue under applied loads [17].

The experimental results of this study clearly show the existence of LRS in porcine coronary and carotid arteries. We have characterized the LRS through measuring the LOA of thin strips cut around the artery. We have also investigated the change in the LOA along the artery. For the LADCA, LRS were found along the entire length of the artery, with a slight increasing trend with higher section numbers. The LADCA exhibited out-of-plane twists in the longitudinal sectors, indicating additional complexities in the residual deformations (**Figure 2.1A**). The variability in the COA was too large to observe any statistical significance. As a result, we are not able to extract any relationship between the LOA and COA in the LADCA.

In the CCA, the LOA exhibited strong increasing trends with the section number. However, we did not find any statistically significant dependence of the COA with section number. Observed individually, however, we found that each vessel had a unique location of minimum COA that was significantly different from the surrounding segments. The section number of this minimum COA varied between the arteries. However, we determined that this variation was localized to two groups, one between section numbers 2 – 3 and another between section numbers 6 – 7. Previous studies have found that the magnitude of the COA exhibited a parabolic trend along the length of the aorta [11, 12]. In those studies, the COA was measured in reference to a percentage of the aortic length; as a result, the location of the minimum COA was consistent between arteries. In the present study, it was not possible to harvest the entire length of the CCA and consequently the COA could not be measured using an absolute reference. As a result, the measurements appeared more scattered. This is a possible explanation for the two minimum COA groups. To reduce this variability we shifted the COA and LOA

based on the lowest COA for each artery and equally shifted the non-minimum COA and LOA values (**Figure 2.11A**).

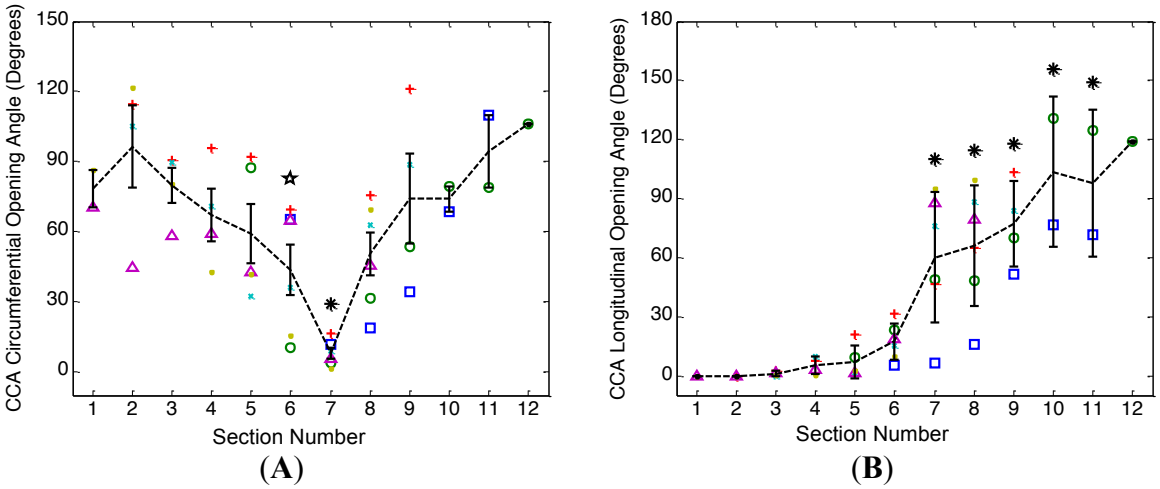

Figure 2.11: Shifting of the section numbers. Shifting location of minimal COA in each artery to a common section number reveals a more apparent trend between the COA (**A**) and LOA (**B**) in the carotid arteries. Statistical significance is observed for the COA and LOA between sections 1 and 11 (ANOVA, $P \leq 0.0005$). Further analysis reveals that the COA from sections 1 to 5 and 6 to 11 are greater than ones from section 7 ($*P < 0.05$). COA from sections 1 to 5 are statistically greater than section 6 as well ($\bigstar P < 0.05$). The LOA from higher section numbers beginning from section 7 are statistically greater than ones from lower section numbers ($*P < 0.05$). This suggests that the LOA increases as the COA approaches a minimum, possibly as a compensatory mechanism for maintaining the circumferential stress gradient. Each symbol type represents a single artery.

This shifting scheme revealed an apparent trend in both the COA and LOA. The COA does indeed decrease to a consistent minimum value (around section 7) as shown in the previous studies. A limitation of this shifting scheme is that it reduced the amount of data points for the lower and higher sections, as a result section 12 was not included in the analysis because it only had one data point. Shifting the LOA revealed a significant increase in the section number beginning from section 6. The most important relationship to note is that the LOA increased as the COA decreased. We speculate that this exchange between the COA and LOA could be a compensatory mechanism attempting to preserve

the homeostatic circumferential stress distribution as the COA decreased. The reason for the decrease in the COA is unknown, but it may be due to a decrease in the pulse pressure as the pressure wave is attenuated further away from the heart. A decrease in the pulse pressure would suggest a decrease in the pulse diameter; therefore a smaller opening angle would be needed to maintain the same homeostatic circumferential stress distribution. This speculation assumes minimal axial variations in the mechanical properties. Our stress analysis does indeed show that the circumferential stress gradient is reduced if the LRS is taken into account. The exchange of the LOA and COA is an exciting find and the underlying mechanisms warrant further investigations.

There are a few limitations of this study that should be addressed. First, we modeled the arteries as a homogeneous material; clearly, however, these arteries are heterogeneous. One possible extension of this study would be to dissect the apart the media and adventitia (as done by [24]) and test each layer individually. In healthy porcine arteries, the mechanical contribution of the intima may be neglected. In preliminary work, we removed the adventitial layer and measured the COA and LOA in the media and found that they were comparable to the intact measurements. Thus, it appears that both COA and LOA are localized in the media (which may be nearly homogeneous). The experimental and computational approaches presented herein could be extended to multi-layered vessels [25].

The existence of residual strains in the traction-free state is a consequence of tissue development, growth, and remodeling that occurs in the physiologically loaded state [26]. It has been argued that cells grow and remodel to restore the mechanical environment in the local neighborhood in which they reside [27]. The consequence of this

hypothesis is that the stresses (or perhaps the strains [28]) in the physiologically loaded configuration would be uniform throughout the tissue. Indeed, our findings suggest that the circumferential stress is nearly uniform across the vessel wall under physiological loads. The axial stress, however, is highly non-uniform across the wall. Limitations of the assumption that the material is homogeneous aside, these results suggest that the smooth muscle cells, which are oriented in the circumferential direction, preferentially restore tractions in the circumferential direction, compared to the axial direction [29].

The non-uniform axial stress results in high tension in the outer wall. For the carotids, which do not have much perivascular support, an outer wall under tension in the axial direction may be favorable in stabilizing the artery from buckling during physiological loads [30]. This, however, does not explain why the coronary arteries, which are sufficiently embedded in perivascular support, also contain LRS.

In conclusion, we present evidence that circumferential and longitudinal residual strains coexist at many locations in the porcine LADCA and CCA, and that incorporating these residual strains into the stress analysis significantly modulates the stress distributions across the artery wall at physiological loads. Future studies should take into consideration multi-axial residual deformations to more accurately characterize the stress-free configuration.

References

1. Taber, L.A. and J.D. Humphrey, *Stress-modulated growth, residual stress, and vascular heterogeneity.* Journal of biomechanical engineering, 2001. **123**(6): p. 528.

2. Delfino, A., et al., *Residual strain effects on the stress field in a thick wall finite element model of the human carotid bifurcation.* Journal of biomechanics, 1997. **30**(8): p. 777-786.

3. Matsumoto, T. and K. Hayashi, *Stress and strain distribution in hypertensive and normotensive rat aorta considering residual strain.* Journal of biomechanical engineering, 1996. **118**(1): p. 62.

4. Raghavan, M., et al., *Three-dimensional finite element analysis of residual stress in arteries.* Annals of biomedical engineering, 2004. **32**(2): p. 257-263.

5. Wang, R. and R.L. Gleason, *A Mechanical Analysis of Conduit Arteries Accounting for Longitudinal Residual Strains.* Annals of biomedical engineering, 2010. **38**(4): p. 1377-1387.

6. Weizsäcker, H., H. Lambert, and K. Pascale, *Analysis of the passive mechanical properties of rat carotid arteries.* J Biomech, 1983. **16**(9): p. 703-715.

7. Chuong, C. and Y. Fung, *On residual stresses in arteries.* J Biomech Eng, 1986. **108**(2): p. 189-192.

8. Vaishnav, R.N. and J. Vossoughi, *Residual stress and strain in aortic segments.* Journal of Biomechanics, 1987. **20**: p. 235-239.

9. Vaishnav, R.N. and J. Vossoughi, *Estimation of residual strains in aortic segments.* Biomedical engineering II, recent developments, 1983. **2**: p. 330-333.

10. Humphrey, J.D., *Cardiovascular Solid Mechanics: Cells, Tissues, and Organs.*2001, New York: Springer-Verlag.

11. Rachev, A. and S. Greenwald, *Residual strains in conduit arteries.* Journal of biomechanics, 2003. **36**(5): p. 661-670.

12. Vossoughi, J. *Longitudinal residual strains in arteries.* in *Proceedings of the 11th Southern Biomedical Engineering Conference, Memphis, TN*. 1992.

13. Holzapfel, G.A., et al., *Layer-specific 3D residual deformations of human aortas with non-atherosclerotic intimal thickening.* Annals of Biomedical Engineering, 2007. **35**(4): p. 530-545.

14. Holzapfel, G.A. and R.W. Ogden, *Modelling the layer-specific three-dimensional residual stresses in arteries, with an application to the human aorta.* Journal of the Royal Society Interface, 2010. **7**(46): p. 787-799.

15. Lui, S. and Y.-C. Fung, *Zero-stress states of arteries.* Journal of Biomechanical Engineering, 1988. **110**: p. 82-84.

16. Chuong, C.J. and Y.-C. Fung, *On residual stress in arteries.* Journal of Biomechanical Engineering, 1986. **108**: p. 189-192.

17. Humphrey, J., *Cardiovascular solid mechanics: cells, tissues, and organs*2002, New York: Springer Verlag.

18. Han, H.C. and D.N. Ku, *Contractile responses in arteries subjected to hypertensive pressure in seven-day organ culture.* Annals of Biomedical Engineering, 2001. **29**(467-475).

19. Davies, P.F., *Flow-mediated endothelial mechanotransduction.* Physiological Reviews, 1995. **75**: p. 519-560.

20. Dzau, V.J. and G.H. Gibbons, *Vascular remodeling - Mechanisms and implications.* Journal of Cardiovascular Pharmacology, 1993. **21**: p. S1-S2.

21. Humphrey, J. and K. Rajagopal, *A constrained mixture model for growth and remodeling of soft tissues.* Mathematical models and methods in applied sciences, 2002. **12**(03): p. 407-430.

22. Hariton, I., et al., *Stress-driven collagen fiber remodeling in arterial walls.* Biomechanics and Modeling in Mechanobiology, 2007. **6**(3): p. 163-175.

23. Wan, W., L. Hansen, and R.L. Gleason, *A 3-D constrained mixture model for mechanically mediated vascular growth and remodeling.* Biomechanics and Modeling in Mechanobiology, 2010. **9**(4): p. 403-419.

24. Holzapfel, G.A., et al., *Layer-specific 3D residual deformations of human aortas with non-atherosclerotic intimal thickening.* Annals of biomedical engineering, 2007. **35**(4): p. 530-545.

25. Berry, J.L., et al. *Analysis of the effects of a non-circular two layer stress-free state on arterial wall stresses*. in *Engineering in Medicine and Biology Society, 1992 14th Annual International Conference of the IEEE*. 1992. IEEE.

26. Cardamone, L., et al., *Origin of axial prestretch and residual stress in arteries.* Biomech Model Mechanobiol, 2009. **8**(6): p. 431-446.

27. Takamizawa, K. and K. Hayashi, *Strain energy density function and uniform strain hypothesis for arterial mechanics.* Journal of Biomechanics, 1987. **20**(7-17).

28. Takamizawa, K. and K. Hayashi, *Strain energy density function and uniform strain hypothesis for arterial mechanics.* Journal of biomechanics, 1987. **20**(1): p. 7-17.

29. Humphrey, J., et al., *Fundamental role of axial stress in compensatory adaptations by arteries.* Journal of biomechanics, 2009. **42**(1): p. 1-8.

30. Rachev, A., *A theoretical study of mechanical stability of arteries.* Journal of biomechanical engineering, 2009. **131**(5): p. 051006.

CHAPTER 3

RESIDUAL SHEAR DEFORMATIONS IN CORONARY ARTERIES: EXPERIMENTAL AND THEORETICAL FRAMEWORKS

Introduction

This study presents novel findings on residual shear deformations (RSD) in the left anterior descending coronary artery (LADCA). RSD are most evident when thin, long axial strips are cut from the artery. These strips deform into helical shapes when placed in a neutrally buoyant environment. A residual shear angle (RSA) is introduced as a parameter to quantify RSD. Stress analyses were performed to analyze the effects of RSD on the intramural shear stress distribution of an artery subjected to pressure, axial stretch, and torsion. The results from the stress analyses suggest that RSD significantly reduces the intramural shear stress across the arterial wall.

It is well recognized that arteries are residually stressed and strained following the removal of all traction forces (i.e., pressure or axial stretch). The single opening angle method was generally believed to be adequate for quantifying the stress-free configuration. Although the single opening angle method has become the standard method of quantifying circumferential residual strains, the presence of longitudinal residual deformations (see Chapter 2) demonstrates that this method does not fully characterize the stress-free configuration [1]. We observed that when long, thin axial strips are cut from the coronary artery, the strips deform into helical spring-like shapes suggesting a combination of longitudinal and shearing residual deformations. Coronary arteries are extensively embedded in perivascular support and are therefore subjected to

dynamic and multi-axial deformations from the beating heart. These deformations, along with circumferential dilation and axial stretch, include a significant amount of torsion, up to 30 degrees of rotation at certain locations [2-5]. Segments of abnormally high torsion have been shown to correlate with higher incidences of atherosclerotic lesions, suggesting a potential pathological role of large torsional deformations [6]. Given that vascular cells possess a remarkable ability to sense and adapt to their local mechanical environment, RSD may be a compensatory development in response to torsional loadings induced by the heart, analogous to the concept that circumferential residual strains normalize the circumferential stresses across the arterial wall at physiologic pressures. RSD have previously been observed in transverse equatorial ring slices of the rat myocardium [7, 8]. When a single radial cut was made in the myocardial rings, they opened into a sector that deformed out of plane. Since it is known that the ventricle undergoes twisting and untwisting in the cardiac cycle [9, 10], this deformation may be associated with the myocardial RSD. This study presents the first observations and mechanical modeling of RSD in blood vessels.

In this study, we show that RSD exist in the coronary artery but the magnitude and direction can vary significantly along the axis. We establish kinematics preliminaries for analyzing the deformation field of RSD. The kinematics of the RSD is combined with that of circumferential and longitudinal residual deformations into a single framework. Different combinations of RSD and axial torsions are analyzed using numerical modeling to demonstrate the effect of RSD on the intramural shear stress of the artery under physiologic loads. Our analyses indicate that with certain combinations, the intramural shear stress could be reduced to nearly zero. Conversely, it can also be greatly increased,

resulting in a high shear stress gradient. Quantifying RSD furthers the understanding of the local mechanical environment of arterial cells, which in turn may help to better understand various mechanically mediated biological responses of arteries in normal and diseased states.

Methods

Tissue Preparation and Cutting Protocol

Hearts of similar sizes (n = 10) from female American Yorkshire farm pigs (2 years of age) were harvested immediately following exsanguination at a local abattoir (Holifield Farms, Covington, GA). The LADCA were carefully dissected and freed of perivascular support on-site. Arteries that exhibited high tortuosity from gross examinations were discarded. The vessels were flushed with Ca^{2+} and Mg^{2+}-free Dulbecco's phosphate buffered saline (DPBS, Mediatech) and placed in ice-chilled DPBS for transport to the laboratory. Ten LADCA were collected, averaging 7.1 ± 0.8 cm (mean ± SD) in length.

A destructive cutting protocol was developed to reveal RSD in the arteries (**Figure 3.1**). In brief, a single straight cut was made down the center of the artery. The artery was then opened and laid flat. A parallel strip running the full length of the flattened artery was then stamped out using a pair of microtome blades spaced 2 mm apart. The excised strip deformed instantly into a complex tortuous configuration when suspended in DPBS. The long strip was further sectioned into thirds, designated as S1, S2, and S3, with S1 being the most proximal section; and each section was incubated in DPBS, resulting in the final helical configuration in **Figure 3.1D**. The sections were

further incubated in DPBS for 3 hrs at 37 ^{o}C to achieve a state of geometric equilibrium. For this preliminary study, the circumferential location of the strip was arbitrary selected.

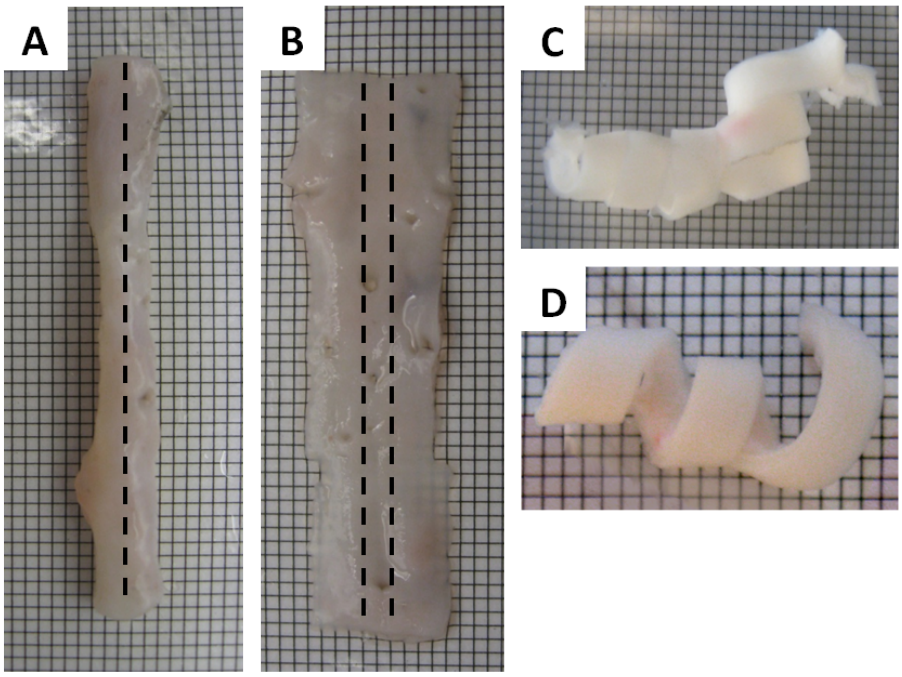

Figure 3.1: Destructive cutting method to reveal RSD in the coronary artery. (**A**) A single straight cut along length of the artery is made. (**B**) The artery is laid flat and a parallel strip is stamped down the center. (**C**) The arterial strip is placed in DPBS, and immediately deforms into the tortuous shape. (**D**) The final configuration is reached following further sectioning.

To ensure that the helical configuration was not an artifact of the cutting method, we performed the same cutting protocol on similarly sized porcine carotid arteries. We found that the carotid strips deformed into a flat watch spring-like shape, indicating only the presence of longitudinal residual deformations and not RSD.

Kinematics

Consider a straight, cylindrical section of an artery in the loaded configuration, β_t, and the traction-free configuration, β_u; let κ_t and κ_u denote a local neighborhood about a

point p, with positions $\mathbf{x_t}(r,\theta,z)$ and $\mathbf{x_u}(\rho,\phi,\zeta)$ within the body in the loaded and traction-free configurations, respectively. Let this neighborhood be denoted κ_n with position $\mathbf{X_n}(R_n, \Theta_n, Z_n)$ in a locally stress-free configuration β_n. Let the gradient of the map $\mathbf{X}_n(R_n, \Theta_n, Z_n) \mapsto \mathbf{x}(r,\theta,z)$ be denoted by $\mathbf{F}$, which may be decomposed into a map from $\mathbf{X}_n(R_n, \Theta_n, Z_n) \mapsto \mathbf{x}_u(\rho,\vartheta,\zeta)$ with gradient $\mathbf{F_1}$ and a map from $\mathbf{x}_u(\rho,\vartheta,\zeta) \mapsto \mathbf{x}_t(r,\theta,z)$, with gradient $\mathbf{F_2}$; thus, $\mathbf{F} = \mathbf{F_2} \cdot \mathbf{F_1}$.

For the inflation, extension, and torsion of a long, straight, axisymmetric tube, neglecting variations along the axial direction, $\mathbf{x}_u(\rho,\vartheta,\zeta) \mapsto \mathbf{x}_t(r,\theta,z)$ is defined as: $r = r(\rho)$, $\theta = \vartheta + \gamma\zeta$, and $z = \lambda_z\zeta$, where $\gamma = \phi/L_u$ is the twist (in radians) per unit traction-free vessel length (L_u) and $\lambda_z = \ell/L_u$ is the axial stretch ratio with ℓ being the loaded vessel length [20]. The deformation gradient for this map is given by:

$$[\mathbf{F_2}] = \begin{bmatrix} \dfrac{\partial r}{\partial \rho} & 0 & 0 \\ 0 & \dfrac{r}{\rho} & r\gamma \\ 0 & 0 & \lambda_z \end{bmatrix} \tag{3.1}$$

Imagine dissecting this artery into infinitesimally thin cylindrical shells, allowing each shell to unload to an individual traction-free state, β_n; assuming an axisymmetric deformation, each shell may take on a different radius, length, and angle of twist from its configuration in β_u. Note that, in β_n the traction forces are:

$$2\pi T_{Z\Theta} dR_n = 0, \quad 2\pi T_{ZZ} dR_n = 0, \quad \text{and} \quad [(T_{\Theta\Theta} - T_{RR})/R_n] dR_n = 0; \tag{3.2}$$

thus, $T_{\Theta Z} = T_{ZZ} = 0$ and, since $P = T_{RR} = 0$, then $T_{\Theta\Theta} = 0$ as well. Also, since $T_{\Theta Z} = 0$, the shearing force along any $\Theta - Z$ plane also equals zero; i.e. $T_{\Theta Z} dR_n dZ_n = 0$. Thus, this configuration is indeed stress-free.

The map from $\mathbf{X}_n(R_n, \Theta_n, Z_n) \mapsto \mathbf{x_u}(\rho, \vartheta, \zeta)$ serves to 'assemble' the discontinuous stress-free cylinders into a continuous, traction-free, albeit residually stressed tube and is defined as: $\rho = \rho(R_n)$, $\vartheta = (\pi/\Theta_o)\Theta + \Upsilon(\rho)Z$, and $\zeta = \Lambda_z(\rho)Z$, where Θ_o is the circumferential arc angle, $\Upsilon = \Upsilon(\rho) = \Gamma(\rho)/L_n(\rho)$ is the twist (in radians) per unit stress-free vessel length $L_n(\rho)$, and $\Lambda_z = \Lambda_z(\rho) = L_u/L_n(\rho)$ is the longitudinal residual stretch ratio as previously set forth. The gradient of this map is defined as:

$$[\mathbf{F_1}] = \begin{bmatrix} \dfrac{\partial \rho}{\partial R_n} & 0 & 0 \\ 0 & \dfrac{\pi\rho}{\Theta_o R_n} & \rho\Upsilon \\ 0 & 0 & \Lambda_z \end{bmatrix} \tag{3.3}$$

The complete mapping from the stress-free to current configuration is therefore:

$$[\mathbf{F}] = [\mathbf{F_2}] \cdot [\mathbf{F_1}] = \begin{bmatrix} \dfrac{\partial r}{\partial R_n} & 0 & 0 \\ 0 & \dfrac{\pi r}{\Theta_o R_n} & r(\Upsilon + \gamma\Lambda_z) \\ 0 & 0 & \lambda_z\Lambda_z \end{bmatrix} \tag{3.4}$$

Note that the term $(\Upsilon + \gamma\Lambda_z)$ is the twist of a cylindrical shell, as it is deforms from the stress-free configuration to the current configuration.

Experimental Approximation of Residual Shear Strains

In Chapter 2, we proposed a method to experimentally approximate R_n and L_n from sectors cut independently from the artery. In this study, we extend the independent cut concept to approximating RSD from images taken of the helical configurations. Prior to imaging, each helical configuration is inspected to ensure that all the edges are freely suspended. A small amount of Indigo ink is applied to the adventitial side of the proximal

end of each section to distinguish the direction of shear (**Figure 3.2**). Images of the sections suspended in DPBS are captured with a tripod mounted CCD camera.

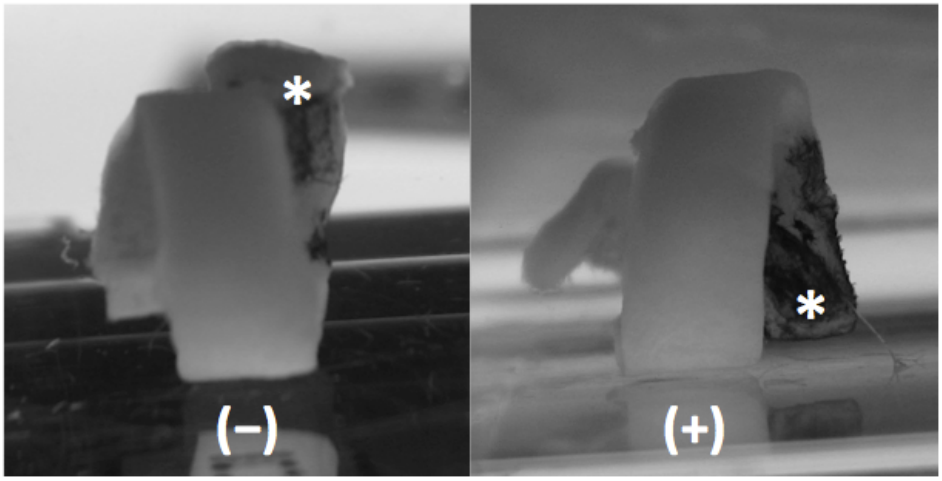

Figure 3.2: Helical configurations exhibiting negative and positive shearing directions. ∗ Denotes the ink-labeled adventitial side of the proximal end and this is used as a spatial reference for determining the shearing direction.

Once the shearing direction is determined, the four corner angles of the parallelogram-like shape (**Figure 3.3**) are measured using image-processing software (ImageJ, National Institute of Health) and the shear angle ω_i (in radians) is calculated using equation (3.5):

$$\omega_i = \frac{x}{4}\sum_{j=1}^{4}\left|\frac{\pi}{2} - \beta_j\right| \tag{3.5}$$

where x = 1 or -1 for either positive or negative shear, respectively. Note that the shear angle is measured along the inner (intima) surface of the artery.

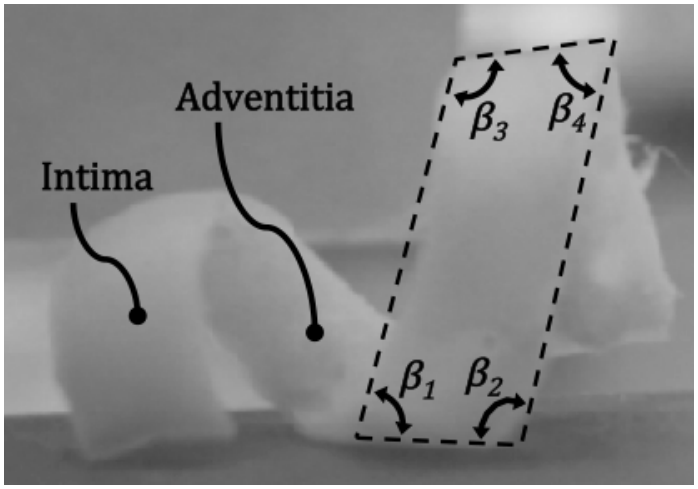

Figure 3.3: Template for measuring the RSA. A representative helical section with an angle measurement template superimposed. Angles $\beta_1 \rightarrow \beta_4$ are used to calculate the RSA (ω_i). Note that these angles are measured along the inner, intimal surface.

Although the stress-free axial twist, Γ, may exhibit radial variations, $\Gamma = \Gamma(\rho)$, the ability to measure only a single RSA forces us to approximate a constant stress-free axial twist (Γ^*) for all cylindrical shells using geometric relationships given in equation (3.6):

$$\Gamma \approx \Gamma^* = \frac{\tan(\omega_i) L_{n,i}}{R_i} \tag{3.6}$$

where $L_{n,i}$ is the stress-free axial length along the inner wall and R_i is the circumferential stress-free radius at the inner wall. This approach is akin to assuming a homogeneous distribution of residual shear stretches across the wall. Despite Γ^* being a constant, the twist per unit stress-free length (Υ) is radially varying since the stress-free length $L_n(\rho)$ is radially dependent.

Stress Analysis

A stress analysis is performed to investigate the effects of RSD on the intramural stresses in a coronary artery subjected to inflation, axial stretch, and torsion. The general Cauchy stress relationship is given by:

$$\mathbf{t} = -p\mathbf{I} + \mathbf{F} \cdot \frac{\partial W}{\partial \mathbf{E}} \cdot \mathbf{F}^{\mathbf{T}} \tag{3.7}$$

where p is the Lagrange multiplier, **I** is the identity tensor, W is the strain energy density function, and **E** is the Green strain tensor. An exponential Fung-type strain energy density function extended for shear is selected for the analysis due to the availability of parameters specific for the LADCA in the literature. This strain energy function is of the following form:

$$W = \frac{c_0}{2}(\exp^Q - 1) \tag{3.8}$$

where $Q = c_1E_{rr}^2 + c_2E_{\theta\theta}^2 + c_3E_{zz}^2 + 2c_4E_{\theta\theta}E_{rr} + 2c_5E_{\theta\theta}E_{zz} + 2c_6E_{zz}E_{rr} + 2c_7E_{\theta z}^2$

Materials parameters c_0 through c_6 were determined by Wang *et al.* [11] and the shear parameter c_7 was solved *in-silico* by Epps and Vorp [12] using data from the former study. The values for these parameters are given in **Table 3.1**.

Table 3.1: Fung-type material parameters from the literature.

c_0 (kPa)	c_1	c_2	c_3	c_4	c_5	c_6	c_7
8.92	0.55	1.25	2.46	0.08	0.36	0.06	0.0759

Furthermore, the traction-free configuration must satisfy the following boundary conditions:

$$P = \int_{\rho_i}^{\rho_o} \left[\frac{t_{\vartheta\vartheta} - t_{\rho\rho}}{\rho}\right] d\rho = 0; \quad \mathcal{L} = 2\pi \int_{\rho_i}^{\rho_o} t_{\zeta\zeta} \rho d\rho = 0; \quad T = 2\pi \int_{\rho_i}^{\rho_o} t_{\vartheta\zeta} \rho^2 d\rho = 0 \tag{3.9}$$

where P is the transmural pressure, $\mathcal{L}$ is the axial force, T is the torque, t_{ij} is the *i, j*-component of the Cauchy stress, where i and $j = \rho, \vartheta,$ or ζ. Note, however, that the normal (N) and shearing (K) forces along any $\vartheta - \zeta$ plane within the vessel wall as well as the normal (M) force along the $\rho - \vartheta$ plane, given as

$$N = L_u \int_{\rho_i}^{\rho_o} t_{\vartheta\vartheta} d\rho; \qquad K = L_u \int_{\rho_i}^{\rho_o} t_{\vartheta\zeta} d\rho; \qquad M = 2\pi \int_{\rho_i}^{\rho_o} \rho t_{\zeta\zeta} d\rho \tag{3.10}$$

are not necessarily equal to zero. Thus, if a dissecting cut was made along a $\vartheta - \zeta$ plane, the vessel may further deform to relieve these normal and shearing forces; namely, the ring springs open to relieve N and bends and shears to relieve M and V, respectively. The deformation to relieve N results in the circumferential sector and indicates that $t_{\vartheta\vartheta}(\rho) \neq 0$ for all $\rho \in [\rho_i, \rho_o]$. Likewise, the deformation to relieve M and V results in the helical sections and indicates $t_{\vartheta\zeta}(\rho) \neq 0$ and $t_{\zeta\zeta}(\rho) \neq 0$ for all $\rho \in [\rho_i, \rho_o]$.

The loaded geometric configuration is solved through minimization of the error between the model pressure, equation (3.11), and the desired pressure of 80 mmHg.

$$P_{mod} = \int_{r_i}^{r_a} (t_{\theta\theta} - t_{rr}) \frac{1}{r} dr \tag{3.11}$$

The axial stretch ratio is fixed at λ_z = 1.40, as prescribed in [17]. Five theoretical cases, representing various combinations of RSA and torsion angles are analyzed (**Table 3.2**). Case 1 represents the current understanding of arterial torsion, an axial twist of an artery without RSD. Conversely, case 2 represents a state of zero axial twist but the presence of a large RSD. Case 3 and 4 represents similar magnitudes but opposite directions of RSA

and axial twists. Finally, case 5 represents equal magnitude and direction of RSA and axial twist, which is expected to amplify the intramural shear stress of the artery.

Table 3.2: Combinations of RSA and torsion angles used in the stress analysis.

	Case 1	*Case 2*	*Case 3*	*Case 4*	*Case 5*
Residual Shear Angle (ω_i)	0^o	20^o	20^o	20^o	20^o
Torsion Angle (ϕ)	-30^o	0^o	-20^o	-30^o	20^o

Statistical Analysis

ANOVA is used to test for differences between multiple means. Statistical analysis is performed using commercial software Excel (Microsoft).

Results

Residual Shear Angle

RSD was observed in all sections of the artery (**Figure 3.4**). Interestingly, several arteries had adjacent sections with opposing shearing directions, suggesting a complex transition zone between those sections. A greater number of positive shears were detected (22 positive versus 8 negative). Seven out of the ten arteries exhibited both positive and negative shears, with the remaining three exhibiting only positive shears. The average RSA was generally consistent between the sections (**Table 3.3**). ANOVA found no statistical differences in the RSA between these sections. The average RSA was 15.6 ± 5.9 degrees (mean ± SD) across all sections.

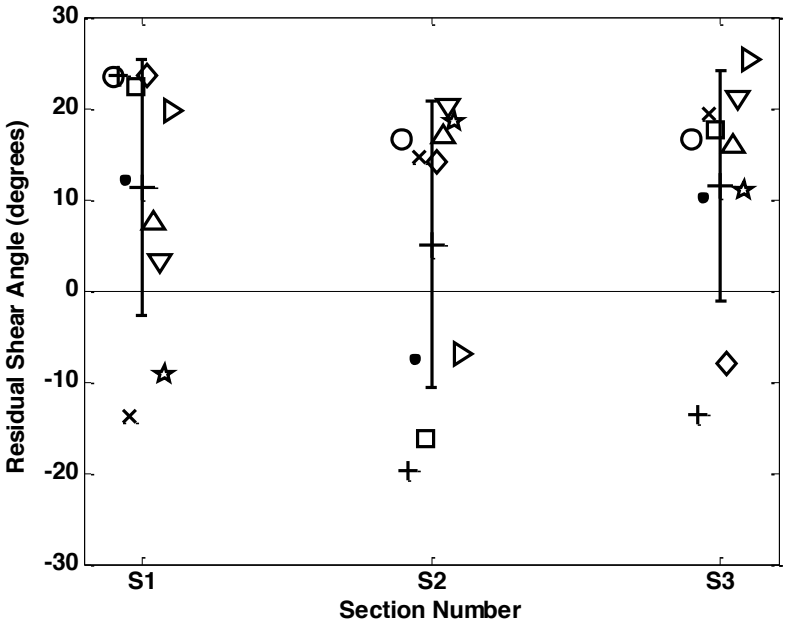

Figure 3.4: RSA experimental results. The RSA are shown relative to the section number. Each artery is divided into three segments of equal length S1, S2, and S3, with S1 being the most proximal section. All sections exhibit RSD. Both magnitude and direction of the RSD varies greatly along the length of the artery. Each symbol type represents a single artery.

Table 3.3: Summary of RSA measurements (in degrees) from each section.

	S1	*S2*	*S3*
Mean ± SD	11.2 ± 14.0	5.1 ± 15.8	11.6 ± 12.7
Max	23.6	20.2	25.3
Min	-13.8	-19.8	-13.7

Stress Analysis

The geometric parameters used for the stress analysis are provided in **Table 3.4**. These geometric parameters consist of previously reported values (traction-free parameters, see [11, 12]), along with ones measured in this study (stress-free parameters). The torsion angles are given in **Table 3.2**.

Table 3.4: Geometric parameters used in the stress analysis.

TF Outer Radius ρ_i	1.219 mm
TF Inner Radius ρ_a	0.963 mm
Circ. Opening Angle Θ_o	169.9 deg
Long. Opening Angle ψ_o	73.9 deg
SF Circ. Inner Radius R_i	20.4 mm
SF Long. Inner Radius S_i	5.5 mm
TF Axial Length	20 mm
Axial Stretch λ_z	1.40

TF: Traction-Free, SF: Stress-Free

Residual Stresses

The residual shear stress (RSS) gradient increased with increasing RSA (**Figure 3.5A**). The corresponding in-plane residual stresses (radial, circumferential, and longitudinal) are shown in **Figure 3.5B**. The circumferential and longitudinal residual stresses (green and blue lines, respectively) followed similar trends as the residual stretches presented in **Figure 2.9B**. However, it was apparent that the radial stress at the outer wall (solid line) failed to fully satisfy the boundary conditions imposed by equation (3.9). Since there were no traction-forces along the outer wall, the radial stress at that point should be zero. Poor predictive capability is an inherent problem of using material parameters from the literature that were not derived for the current conditions (see Discussion section).

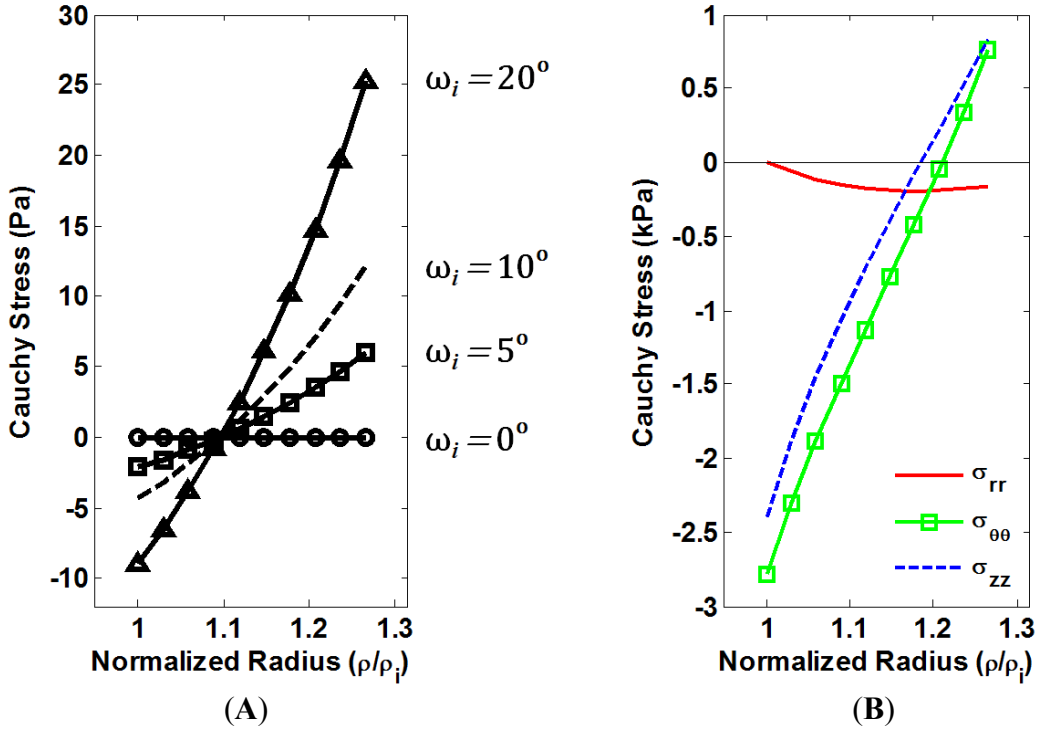

Figure 3.5: Intramural residual stresses. (**A**) Gradient of the intramural RSS increases with increasing RSA (ω_i). (**B**) In-plane intramural residual stresses for $\omega_i = 20^{\circ}$. Note that the radial boundary condition is not completely satisfied by using parameters in the literature; the radial stress (solid line) at outer wall should be zero.

The values for the remaining boundary conditions imposed by equations (3.9) and (3.10) are provided in **Table 3.5**. For a non-zero RSA, the torque T, luminal pressure P, and axial force $\mathcal{L}$ should be zero. Again, it is apparent that the boundary conditions are not fully satisfied using the available literature parameters, although the differences do not appear to be significant.

Table 3.5: Boundary conditions in the traction-free state. T is the torque, K is the shearing force along the $\vartheta - \zeta$ plane, P is the luminal pressure, and $\mathcal{L}$ is the axial force.

	$\omega_i = 0^{\circ}$	$\omega_i = 5^{\circ}$	$\omega_i = 10^{\circ}$	$\omega_i = 20^{\circ}$
T (μNm)	0	0.0032	0.0064	0.0131
K (μN)	0	6.75	13.64	28.5
P (mmHg)	-4.9	-3.9	-3.1	-2.4
$\mathcal{L}$ (N)	-0.0018	-0.0012	-0.0008	-0.0004

Loaded Stresses

The intramural shear stress distribution of the artery subjected to pressure, axial stretch, and torsion are highly depended on different combinations of RSA and torsion angles (**Figure 3.6**). Case 3, representing a condition in which the axial twist and RSA are equal in magnitude but opposite in direction, exhibits the lowest stress gradient and mean magnitude. Conversely, case 5, where the magnitude and direction of the RSA and torsion angle are equal, exhibits the highest gradient and mean stress. Case 1, without RSA, represents the simple torsion of a tube, where the outer wall experiences the highest shear stress and the inner wall experiences the lowest. Finally, case 2, which represents the presence of only RSA, demonstrates the amplification of stress from the traction-free to loaded configuration due to the nonlinearity of soft tissue [13]. The loaded shear stress is several times greater than the residual shear stress for the same RSA even in the absence of arterial torsion.

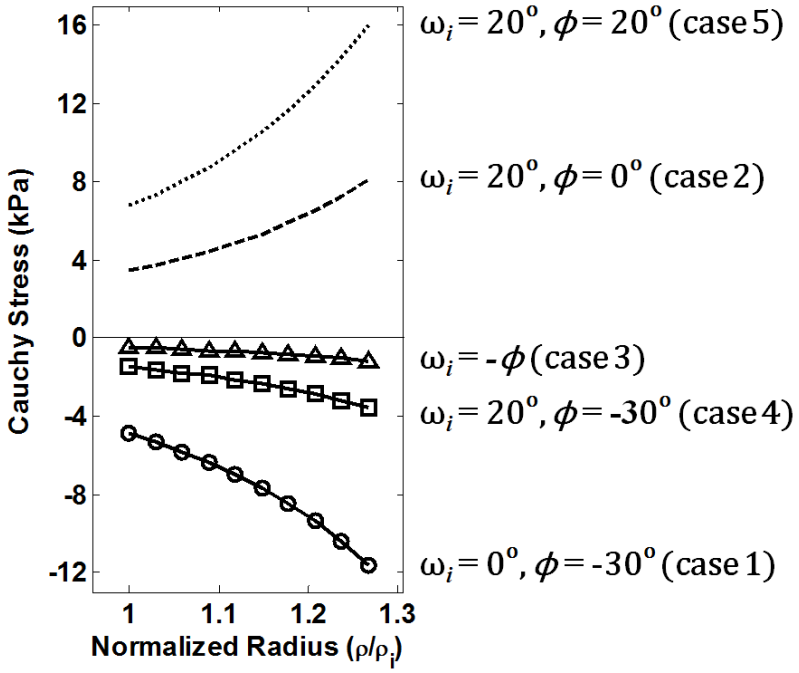

Figure 3.6: Intramural shear stresses with loading. The shear stress distributions change significantly with various combinations of RSA and twisting angles. The magnitudes of the angles are within the bounds of experimental measurements. Case 4 and 5 represent two extreme cases in which the residual shear and twist angles are either opposing or equal in direction. Case 1 is the shear stress distribution without RSA.

Discussion

Experimental evidence of RSD in porcine coronary arteries is presented in this study. We found that the RSA varies along the length of artery. Opposing residual shear directions between adjacent sections are a noteworthy find. A previous study that tracked the *in-vivo* twisting of the LADCA on beating hearts found adjacent sections of the artery that twisted in opposing directions, forming complex transition zones [3]. The opposing *in-vivo* twists may serve to explain the opposing residual shear directions, this furthers our speculation that RSD is a compensatory development that serves to normalize or reduce intramural shear stresses induced by torsional loads on the artery. However, correlating the actual direction of residual shear and local twists at the same axial location

is challenging. To do so would require *in-vivo* measurements of the axial twists, using biplanar angiography [4-6], at designated axial locations, then excising the artery and measuring the RSA at those locations.

Kinematics

We proposed that the true stress-free configuration of the artery consists of a series of concentric, infinitesimally thin cylindrical shells, each with a unique length and radius. The cylinders undergo axial and circumferential stretches as well as axial twists as they are being assembled into a continuous traction-free tube, and the incompatibility of the layers during assembly results in the formation of residual stresses. It is apparent that the infinitesimal cylinder configuration is experimentally intractable. As a result, we must approximate the stress-free configuration by making independent stress-relieving cuts. The deformations from each independent cut can then be mapped into a single traction-free configuration.

The central geometric assumption of this study is that the residual twist (Γ^*) is constant, exhibiting no transmural variation. This may be true if the artery is subjected to a constant twist angle throughout its lifetime. In other words, as each infinitesimal cylindrical shell is laid down during growth and development, the angle of twist for each shell is preserved. This assumption depends on a proportional growth and change in the deformation between the heart and the coronary artery [14].

The presence of RSD could suggest non-axisymmetric alignments of the arterial ECM, particularly of collagen fibers. Arterial collagen undergoes consistent and rapid turnover (on the order of weeks [15]). The cyclic twisting of the coronaries may allow for

off-axis depositions of new collagen. This speculation can be verified by imaging the collagen fibers using two-photon excitation microscopy and applying a fast-Fourier transform analysis to quantify the fiber angle distribution [16-18].

Likewise, RSD also suggest non-axisymmetric deformation of the artery during multi-axial loadings. Indeed, Carboni *et al.* observed this when they measured the twisting of the circumflex coronary artery under axially unconfined conditions. They found that the arteries can rotate both clockwise and counterclockwise with pressurization [19], although the shear stretch due to the rotation was significantly less than the in-plane stretches due to pressure and axial elongation.

Limitations

There are limitations to this study that need to be addressed in future investigations. First, we utilized material parameters found in the literature for the stress analysis. Although these material parameters were determined for the LADCA, they were solved considering only a single circumferential opening angle (Θ_o). The present study incorporates both LRD and RSD in addition; future works will need to refit the material parameters using the proposed kinematic framework. Nonetheless, the literature parameters are suitable for this preliminary analysis, given that the required boundary conditions are reasonably satisfied.

Second, as briefly mentioned above, we do not have the capability of correlating the direction and magnitude of the local *in-vivo* coronary twists to the corresponding local RSD. This precludes us from making any determination on the actual *in-vivo* intramural shear stresses. Unlike circumferential dilation and axial stretch, the *in-vivo*

axial twist needs to be measured *in-vivo*, which can be a considerable technical challenge. The different cases presented in this study (**Figure 3.6**) are not meant to represent physiologic combinations, but rather to showcase the possible effects of different combinations of RSD and arterial twists, but within the physiologic bounds.

Lastly, the RSA measurement technique can be improved. In this study, the axial strips are taken from one continuous arbitrary circumferential location. Circumferential variations should be investigated by cutting strips around the circumference of the artery. Cutting long axial strips to reveal RSD and measuring only one RSA per section reduces the ability to observe any significant axial trends. The difficulty in sampling more axial locations lies in the need to properly orientate the helical configuration to the camera plane.

With these limitations aside, this study presents the first evidence of residual shear deformations in blood vessels. Thus far, we believe that RSD is unique to the coronary arteries, the only vasculature that is subjected to consistent large cyclic torsions. We have proposed a kinematic framework that can incorporate multi-axial residual deformations in order to better predict the *in-vivo* mechanical environment of the artery. The preliminaries set forth by this study can be utilized to study mechanically mediated biological mechanisms of arteries in normal and diseased states.

References

1. Wang, R. and R.L. Gleason, *A Mechanical Analysis of Conduit Arteries Accounting for Longitudinal Residual Strains.* Annals of biomedical engineering, 2010. **38**(4): p. 1377-1387.

2. Pao, Y., J. Lu, and E. Ritman, *Bending and twisting of an in vivo coronary artery at a bifurcation.* Journal of biomechanics, 1992. **25**(3): p. 287-289.

3. Puentes, J., et al., *Dynamic feature extraction of coronary artery motion using DSA image sequences.* Medical Imaging, IEEE Transactions on, 1998. **17**(6): p. 857-871.

4. Ding, Z. and M.H. Friedman, *Quantification of 3-D coronary arterial motion using clinical biplane cineangiograms.* The International Journal of Cardiac Imaging, 2000. **16**(5): p. 331-346.

5. Ding, Z., H. Zhu, and M.H. Friedman, *Coronary artery dynamics in vivo.* Annals of biomedical engineering, 2002. **30**(4): p. 419-429.

6. Ding, Z. and M.H. Friedman, *Dynamics of human coronary arterial motion and its potential role in coronary atherogenesis.* Journal of biomechanical engineering, 2000. **122**(5): p. 488.

7. Omens, J.H., H.A. Rockman, and J.W. Covell, *Passive ventricular mechanics in tight-skin mice.* American Journal of Physiology-Heart and Circulatory Physiology, 1994. **266**(3): p. H1169-H1176.

8. Guccione, J., A. McCulloch, and L. Waldman, *Passive material properties of intact ventricular myocardium determined from a cylindrical model.* Journal of biomechanical engineering, 1991. **113**(1): p. 42.

9. Notomi, Y., et al., *Measurement of ventricular torsion by two-dimensional ultrasound speckle tracking imaging.* Journal of the American College of Cardiology, 2005. **45**(12): p. 2034-2041.

10. Helle-Valle, T., et al., *New noninvasive method for assessment of left ventricular rotation speckle tracking echocardiography.* Circulation, 2005. **112**(20): p. 3149-3156.

11. Wang, C., et al., *Three-dimensional mechanical properties of porcine coronary arteries: a validated two-layer model.* American Journal of Physiology-Heart and Circulatory Physiology, 2006. **291**(3): p. H1200.

12. Van Epps, J.S. and D.A. Vorp, *A New Three-Dimensional Exponential Material Model of the Coronary Arterial Wall to Include Shear Stress Due to Torsion.* Journal of biomechanical engineering, 2008. **130**: p. 051001.

13. Rachev, A. and S. Greenwald, *Residual strains in conduit arteries.* Journal of biomechanics, 2003. **36**(5): p. 661-670.

14. Hort, W., et al., *The size of human coronary arteries depending on the physiological and pathological growth of the heart the age, the size of the supplying areas and the degree of coronary sclerosis.* Virchows Archiv, 1982. **397**(1): p. 37-59.

15. Humphrey, J., *Cardiovascular solid mechanics: cells, tissues, and organs*2002, New York: Springer Verlag.

16. Timmins, L., et al., *Structural inhomogeneity and fiber orientation in the inner arterial media.* Am J Physiol Heart Circ Physiol, 2010. **298**(5): p. H1537-H1545.

17. Nishimura, T. and M. Ansell, *Fast Fourier transform and filtered image analyses of fiber orientation in OSB.* Wood Sci and Technol, 2002. **36**(4): p. 287-307.

18. Wan, W., J. Dixon, and R. Gleason, *Constitutive modeling of mouse carotid arteries using experimentally measured microstructural parameters.* Biophys J, 2012. **102**(12): p. 2916-2925.

19. Carboni, M., G.W. Desch, and H.W. Weizsacker, *Passive mechanical properties of porcine left circumflex artery and its mathematical description.* Medical engineering & physics, 2007. **29**(1): p. 8-16.

CHAPTER 4

DIFFERENTIAL MECHANICAL RESPONSES AND MICROSTRUCTURAL ORGANIZATIONS BETWEEN NON-HUMAN PRIMATE FEMORAL AND CAROTID ARTERIES

Introduction

Due to unique physiologic functions, arteries from different locations across the vasculature tree exhibit different mechanical behaviors. However, the underlying causes of these mechanical differences are not well understood. The objective of this study was to identify structural differences in the arterial matrix that would account for the mechanical differences between the femoral and carotid arteries. Carotid and femoral arteries were tested under biaxial loading conditions. Their microstructure was quantified using histology and two-photon microscopy. Their opening angles and collagen and elastin contents were determined as well. The femoral arteries were found to be less compliant than the carotid arteries, but their elastin and collagen compositions were very similar ($P > 0.05$). However, the femoral arteries exhibited significantly less circumferential dispersion of collagen fibers ($P < 0.0005$), but their mean fiber alignment direction did not differ from the carotid arteries. The elastic fibers in the femoral arteries were localized further outward in the wall, and this may be associated with their greater opening angles. The findings support an important role for microstructural organization on arterial stiffness in healthy vessels. Application of these findings may be utilized to develop artery-specific therapies to modulate the microstructure during arterial remodeling.

Arterial function in health and disease is closely associated with the artery's mechanical behavior. This behavior is largely dominated by two structurally relevant proteins in the arterial extracellular matrix (ECM), collagen and elastin [1, 2]. Collagen is considered the primary load-bearing constituent due to its high tensile strength, and serves to resist the distension of the arterial wall at elevated blood pressures [3]. Elastin confers compliance on the wall, allowing the artery to recoil and dampen pulsatile pressure waves [4]. The ECM is characterized by a complex organization and transmural distribution of these constituents. However, in general elastin is arranged as concentric lamellar units [5] and collagen fibers align with the direction of mechanical strain [6]. Despite the above consistencies, different arteries are known to exhibit different mechanical responses depending on their anatomical location [7], suggesting local differences in their microstructure. Thus, in order to better understand the origins of the macro-level mechanistic differences between arteries, their microstructures must first be examined and compared.

Normal carotid and femoral arteries are known to exhibit differences in compliance both *in-vivo* and *in-vitro* [8-10]. Quantitative and structural differences in their ECM are believed to contribute to their mechanical differences [8], and this difference may help to explain preferential responses of the arteries to disease and remodeling after surgical intervention [11, 12]. For instance, in subjects with essential hypertension, both femoral and carotid arteries exhibit an increase in stiffness. However, the carotid artery is believed to stiffen through a pressure-dependent strain-stiffening response, whereas the femoral artery stiffens through a pressure-independent, intrinsic wall compositional change [12].

The objective of this study was to identify microstructural features that might confer differential stiffness to non-human primate femoral and carotid arteries. This was accomplished by first characterizing the arteries' salient mechanical behaviors, including compliance and biaxial response in their respective *in-vivo* configurations. The organization of collagen and elastin between the arteries was then quantified using traditional histology and two-photon excitation microscopy (TPEM). Quantitative assays were used to assess content differences in collagen and elastin between the arteries.

Methods

Tissue Harvest and Preparation

Left and right common carotid and femoral arteries were harvested from eight healthy adult non-human primates (Rhesus Macaques, 10.6 ± 7.0 years old) during necropsy. The ages and genders of the animals are provided in **Table 4.1**. The arteries were transported to the laboratory in ice-chilled saline. Perivascular remnants were removed using sharp dissection and the vessels were frozen at -80 ^{o}C. Prior to testing, the arteries were thawed at room temperature. All arteries were subjected to the same freeze-thaw protocol. The arteries were cut into three segments, two 3 mm segments were used for histology and composition analysis, and a 14 mm segment was mechanically tested.

Table 4.1: The genders and ages of the non-human primates used in this study.

Specimen	*1*	*2*	*3*	*4*	*5*	*6*	*7*	*8*
Gender	M	M	M	F	F	M	M	F
Age (yrs)	9.8	6.3	7.5	25.6	5.3	4.7	6.3	16.0

Mechanical Characterization

The passive mechanical behavior of the arteries was assessed using a custom cylindrical biaxial testing device, which has been described in detail elsewhere [13, 14]. In brief, the artery was mounted between metal cannulae and submerged in a bath filled with Ca^{2+} and Mg^{2+}-free Dulbecco's Phosphate-Buffered Saline (DPBS, Cellgro), maintained at 37 ^{o}C. The artery was subjected to quasi-static, constant-rate pressurization cycles between 0 - 120 mmHg at fixed axial lengths while the outer diameter and axial force were monitored. At each axial length, the artery was preconditioned through several pressurization cycles to achieve a repeatable pressure-diameter (p - d) curve, after which representative data was collected. The axial stretch was incrementally increased until a nearly static axial force independent of the lumen pressure was achieved, thus establishing the *in-vivo* axial stretch of the artery [15]. Following the mechanical test, the traction-free wall thickness was measured photometrically from a ring cut from the central region of the artery. Finally, the circumferential stress-free configuration was revealed by making a radial cut down the length of the arterial ring, allowing it to spring open into a sector. The opening angle of the sector was then measured using established methods [16].

The local arterial compliance (C) was calculated from the p - d response at increments of 20 mmHg using equation (4.1):

$$C = \frac{\Delta d}{d_o \Delta P} \times 100\% \tag{4.1}$$

where $\Delta d/\Delta P$ is the slope of the p - d curve taken at a current outer diameter, d_o [17]. The inverse of compliance is referred to as stiffness. The mean circumferential or hoop ($\bar{\sigma}_\theta$) and axial ($\bar{\sigma}_z$) stresses were calculated using equation (4.2):

$$\bar{\sigma}_\theta = \frac{P d_i}{2h} \quad \text{and} \quad \bar{\sigma}_z = \frac{4F + \pi d_i^2 P}{2\pi h(d_o + d_i)} \tag{4.2}$$

where d_i and h are the inner diameter and thickness, respectively. P and F are the corresponding lumen pressure and axial force, respectively [17, 18]. The term $\pi d_i^2 P$ arises from the end-cap pressure. The inner diameter (d_i) was calculated by invoking the assumption of an incompressible arterial wall, namely:

$$d_i = \left[d_o^2 - \frac{1}{\lambda_z}(2HD_o - H^2) \right]^{1/2} \tag{4.3}$$

where λ_z is the axial stretch ratio defined as the ratio of the stretched to traction-free length. H and D_o are the traction-free wall thickness and outer diameter, respectively [17].

Microstructural Characterization

TPEM was used to image the microstructure of the medial collagen from five carotid and five femoral arteries. In brief, an additional arterial ring was cut from the artery following mechanical testing. The ring was cut open and laid flat with its lumen facing down on a glass cover slip. The flat arterial strip was orientated so that its

circumferential axis was aligned with *x*-axis of the microscope view plane. An area measuring 450 μm × 450 μm at the center of the strip was imaged through a 20X objective (Zeiss) on an inverted confocal microscope (LSM 510 META, Zeiss). The sample was excited using an 800 nm laser (Chameleon, Coherent) and the second-harmonic generation signal from the collagen was measured through a 380 – 420 nm bandpass filter. Once the basement membrane was identified, images were taken at 2 - 3 μm increments into the depth of the tissue up to 100 μm. Each frame was averaged 16 times to maximize the resolution and noisy images deeper into the wall were discarded. Image processing, based on a fast-Fourier transform (FFT) algorithm, was used to extract the distribution of fiber angles (θ) from each image [19, 20]. The distribution did not change appreciably across the imageable thickness; therefore a single distribution was calculated for each artery by averaging together the individual distributions across the wall. Each averaged distribution was fitted to a von Mises distribution of the form given by equation (4.4):

$$P(\theta) = \frac{e^{\kappa \cos(\theta - \mu)}}{2\pi I_0(\kappa)} \tag{4.4}$$

where $\theta \in [-\pi/2, \pi/2]$ is the fiber direction, μ is the location of the peak, κ is a measure of the concentration, and $I_0(\kappa)$ is a modified Bessel function of the first kind of order 0. The circumferential direction is designated as 0 rad.

The fit error between the model and experimental-FFT fiber distributions is defined by equation (4.5):

$$\text{Error} = \sqrt{\frac{\sum_{i=1}^{N}[P(\theta_i) - y_i]^2}{\sum_{i=1}^{N} y_i^2}} \tag{4.5}$$

where $P(\theta_i)$ and y_i are the model and experimental values taken at angle i, respectively.

Collagen and Elastin Content

The collagen and elastin contents in the femoral and carotid arteries were analyzed using commercial assay kits. For the collagen assay, the samples were dried and digested with 0.5 M acetic acid (Sigma) and 10 mg/mL pepsin (Sigma) for 48 hrs at 37 ^{o}C. The samples were centrifuged and the collagen content of the supernatant was analyzed using the Sircol Collagen Assay Kit (Biocolor). For the elastin assay, dried samples were incubated in 0.25 M oxalic acid (Sigma) at 100 ^{o}C for 1 hr. The samples were then centrifuged and the supernatant was saved. The process was repeated five times until all elastin had been isolated from the tissue. The supernatants were pooled and analyzed for elastin content using the Fastin Elastin Assay Kit (Biocolor). Each artery was analyzed three times and there were at least six samples of each type of artery.

Histology

Arteries were fixed in 10% formalin, embedded in paraffin, and sliced 5μm thick. Standard hematoxylin and eosin (H&E), Masson's trichrome (MT), and Verhoeff-Van Gieson (VVG) stains were used. Images of the stained arteries were captured under 10X bright field magnification.

Statistical Analysis

Student's *t*-test (two-tailed) was used to analyze for significance between means, where the significance threshold was defined as $P < 0.05$. Statistical analysis, post-processing, and plotting were performed using commercial software Excel (Microsoft) and MATLAB (MathWorks). Results are reported as mean ± SEM.

Results

Mechanical Testing

Biaxial mechanical testing was performed on 18 arteries, consisting of 9 common femoral arteries (3 left and 6 right) and 9 common carotid arteries (5 left and 4 right). There were no significant differences between their traction-free outer diameters (D_o = 3.16 ± 0.10 mm for femoral arteries and D_o = 3.02 ± 0.09 mm for carotid arteries, P = 0.38). Differences were also insignificant between their thickness-to-diameter ratios (H/D_o = 0.17 ± 0.01 for femoral arteries and H/D_o = 0.15 ± 0.01 for carotid arteries, P = 0.12). The femoral arteries exhibited a 13% higher *in-vivo* axial stretch ratio than the carotid arteries (λ_z = 1.64 ± 0.05 for femoral arteries and λ_z = 1.45 ± 0.06 for carotid arteries, P = 0.01). The p - d responses at the *in-vivo* stretches were different between the arteries as well. At low pressures (0 - 40mmHg) the femoral arteries distended more than the carotid arteries; however, as the pressure increased to physiologic levels, the femoral arteries underwent more pronounced strain stiffening and a crossover of their p - d responses occurred at approximately 60 mmHg, resulting in a greater final distension of the carotid arteries (**Figure 4.1A**). Femoral arteries exhibited greater initial compliance, but the compliance decreased rapidly as the pressure increased. The carotid arteries

exhibited a gradual monotonic decrease in compliance, resulting in greater compliance at physiologic pressures (**Figure 4.1B**).

The femoral and carotid arteries exhibited nearly identical circumferential stresses for the same pressures in their respective *in-vivo* axial stretch configurations (**Figure 1C**). However, the mean axial stress was significantly higher in the femoral arteries (**Figure 1D**). Lastly, the opening angles (*OA*) of the femoral arteries were found to be significantly higher ($OA = 113.3^{o} \pm 14.5^{o}$ for femoral arteries and $OA = 50.6^{o} \pm 4.8^{o}$ for carotid arteries, $P = 0.001$).

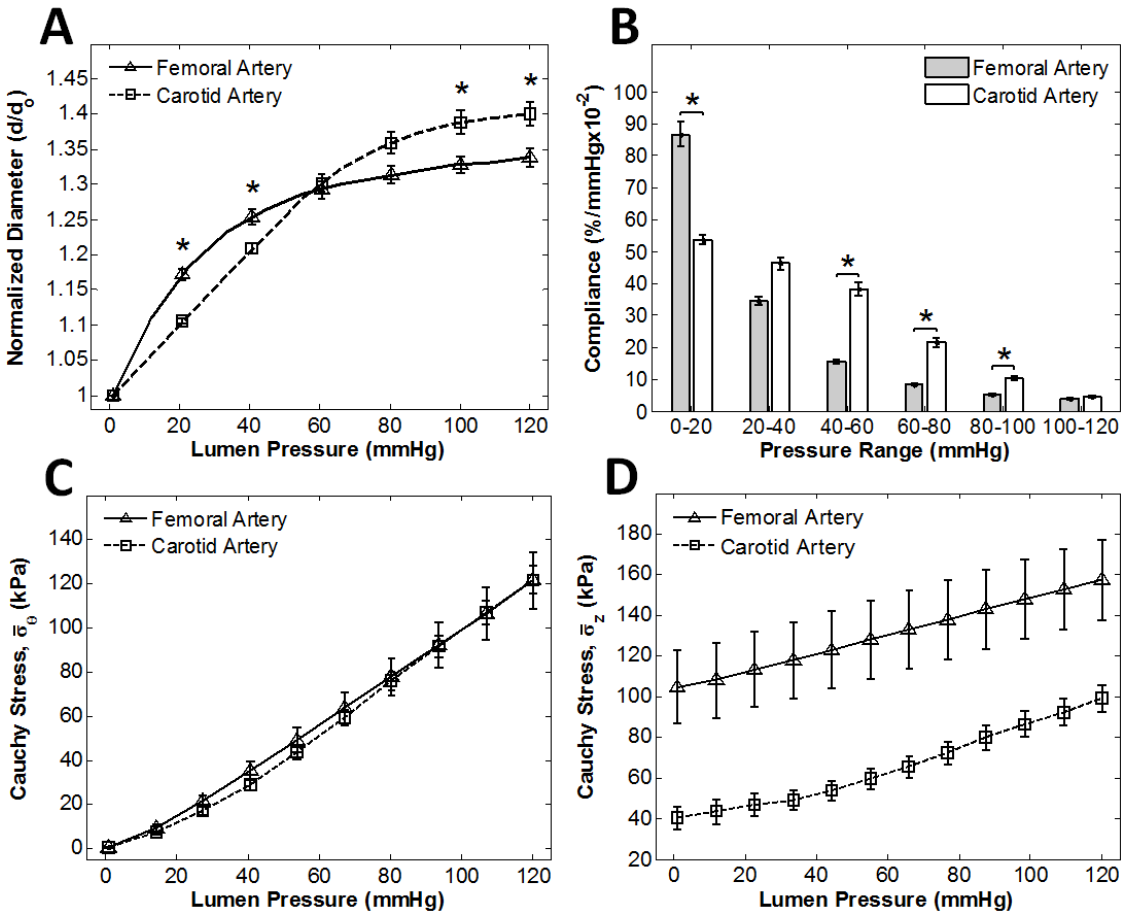

Figure 4.1: Mechanical responses of the femoral and carotid arteries. (**A**) Pressure-diameter relationship between the femoral and carotid arteries at their *in-vivo* axial stretches. The diameters are normalized to their initial values (*$P < 0.05$). (**B**) Local compliance differences between the femoral and carotid arteries at their *in-vivo* axial stretch assessed at increments of 20 mmHg (*$P < 0.05$). (**C**) Mean circumferential or hoop stress and pressure relationship between the femoral and carotid arteries. Significances between means were not found. (**D**) Mean axial stress and pressure relationship. Significant differences between mean axial stresses were found at all pressures.

Microstructural Characterization

TPEM revealed distinct differences in the organization of collagen fibers between the femoral and carotid arteries (**Figure 4.2A-B**). The microstructure of the femoral arteries appeared significantly more organized than the carotid arteries, and this finding was confirmed through the FFT-based image analysis (**Figure 4.2C-D**). The von Mises

distribution fits closely matched the raw FFT distributions (**Table 4.2**). The collagen microstructure from both arteries exhibited a mean fiber alignment in the circumferential direction (μ = -0.038 ± 0.052 rad for the femoral arteries and μ = -0.025 ± 0.060 rad for the carotid arteries, P = 0.802); however, the fiber distribution was appreciably more concentrated in the femoral than the carotid arteries (κ = 25.368 ± 10.728 for the femoral arteries and κ = 6.984 ± 1.228 for the carotid arteries, P = 0.025). Thus, there is significantly greater circumferential orientation of medial collagen fibers in the femoral arteries than in the carotid arteries.

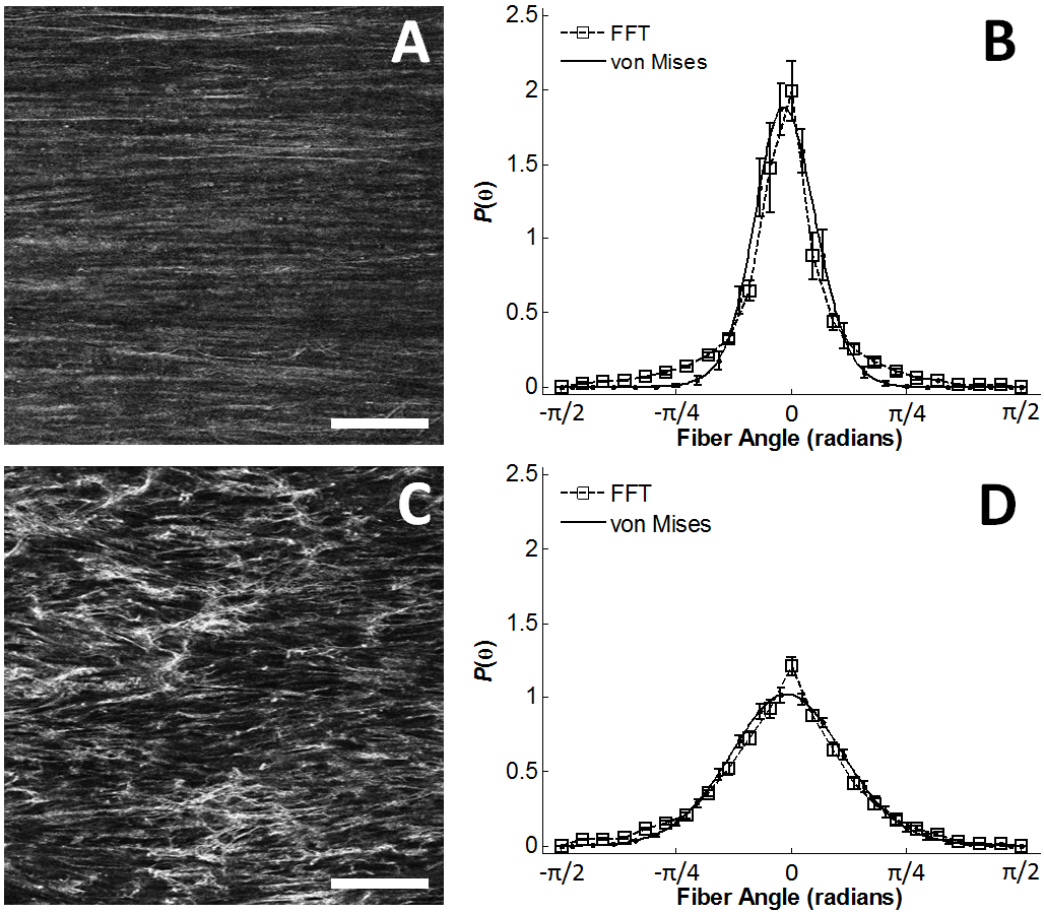

Figure 4.2: Microstructural differences between the femoral and carotid arteries. The microstructure of the femoral artery (**A**) appears more organized and aligned than the carotid artery (**B**). The horizontal axes of the images correspond to the circumferential axes of the arteries. While scale bar = 100μm. Femoral arteries exhibit a high, narrow peak centered on 0 rad (**C**), whereas the carotid arteries exhibit a broader peak, although still centered on 0 rad (**D**). The FFT distributions (dotted line, square markers) were fitted to a von Mises distribution (solid line).

Table 4.2. Parameters of the von Mises function.

Femoral Arteries	μ	κ	% Error
1	-0.036	21.550	7.24
2	-0.113	41.715	8.94
3	0.031	27.365	7.87
4	-0.049	12.298	5.01
5	-0.024	24.202	9.15
Mean ± SD	-0.038 ± 0.052	25.368 ± 10.728	7.64 ± 1.67

Carotid Arteries	μ	κ	% Error
1	-0.0020	6.6729	2.39
2	0.0514	5.1486	2.28
3	-0.1096	6.9511	2.59
4	-0.0500	7.7733	3.03
5	-0.0151	8.3758	3.48
Mean ± SD	-0.0251 ± 0.0597	6.9843 ± 1.2275	2.75 ± 0.50

μ and κ are parameters for the peak location and concentration, respectively.

Collagen and Elastin Content

Collagen and elastin contents were analyzed using the assay methods described previously. We found no significant differences in mass fractions of either collagen or elastin between the femoral and carotid arteries. Collagen constituted 46.5 ± 4.2% and 42.8 ± 4.3% (P = 0.21) of the dry weight in the femoral and carotid arteries, respectively. Elastin constituted 26.2 ± 1.4% and 27.2 ± 2.0% (P = 0.17) of the dry weight in the femoral and carotid arteries, respectively.

Histological Analysis

The H&E stains (**Figure 4.3A-B**) show similar microstructure between the two arteries; however, the VVG stains (**Figure 4.3C-D**) show distinctly different transmural distribution of elastic fibers. In the femoral arteries, the elastic fibers appear concentrated around the external elastic lamina (C), whereas the elastic fibers in the carotid arteries are

evenly distributed across the media (D). Lastly, MT stains (**Figure 4.3E-F**) show slightly more dense muscular fibers in the femoral arteries.

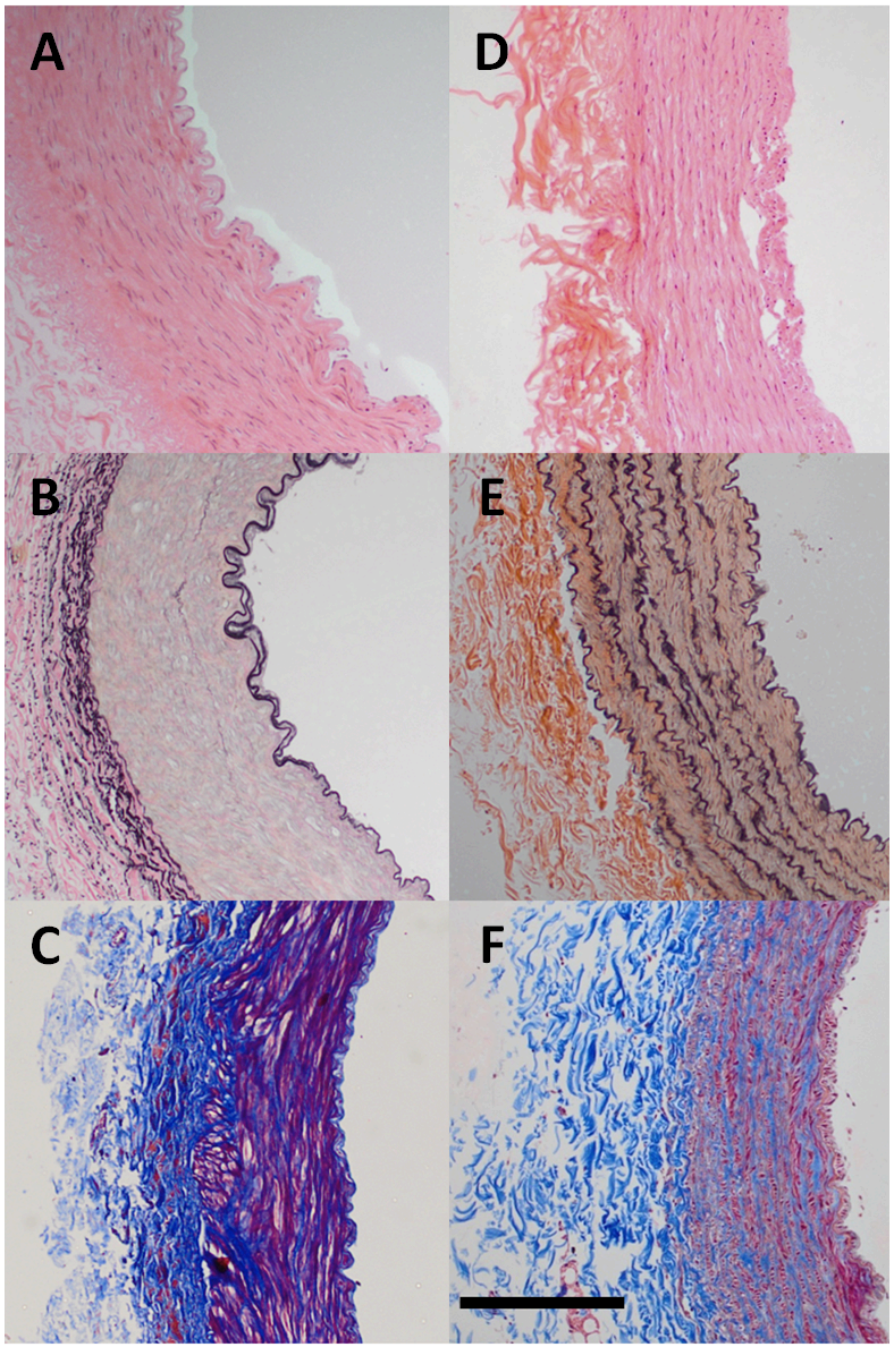

Figure 4.3: Histological stains of femoral and carotid arteries. **A**, **C**, and **E** show the carotid artery stained using hematoxylin and eosin (H&E), Verhoeff-Van Gieson (VVG), and Masson's Trichrome (MT), respectively. **B**, **D**, and **F** show the femoral artery stained using H&E, VVG, and MT respectively. The H&E stains show similar microstructure. The VVG stains show differential transmural distribution of elastin. The MT stains show higher concentration of muscular fibers in the femoral arteries. Black scale bar = 250μm.

Discussion

Collagen and elastin are the primary load bearing constituents of the arterial ECM. The microstructure and spatial distribution of these constituents has been established as an important mediator of the artery's mechanical behavior. The present study examined mechanical and microstructural differences between femoral and carotid arteries harvested from healthy non-human primates. These arteries are geometrically similar but are from different anatomical locations and thus exhibit different mechanical responses. The novel finding of this study is that the microstructure between the two arteries display significant variation in the dispersion of their medial collagen fibers, while maintaining nearly identical mean circumferential alignment of these fibers. The collagen fibers in the femoral arteries were significantly less dispersed, resulting in more fibers aligning in the circumferential direction when compared to the carotid arteries. This was associated with a greater circumferential stiffness of the femoral arteries assessed through *in-vitro* mechanical testing. In addition, histological analysis found that elastin localized along the external elastic lamina in the femoral arteries, whereas in the carotid arteries, elastin was evenly distributed across the media. The mass fractions of collagen and elastin were found to be very similar between the arteries, in agreement with analysis of the same types of arteries from canine specimens [22]. These findings suggest a prominent mechanical role for microstructural organization in the ECM and show that distinct microstructural differences can still exist despite apparent similarities in overall organization. These microstructural differences may help to explain the differential mechanical response between femoral and carotid arteries.

Despite the differences described previously, the hoop stress between the femoral and carotid arteries was nearly identical at physiologic pressures. This finding is consistent with the idea that hoop stress is preserved between arteries to serve as a homoeostatic target for growth and remodeling [23]. For a given pressure, the hoop stress is dependent only on the artery's thickness to diameter ratio, as shown through equation (4.2). The femoral and carotid arteries share insignificant differences in this ratio in their traction-free states; therefore the same ratio must be maintained between the arteries during inflation to yield the same hoop stress. Given the differences in circumferential distension between the femoral and carotid arteries, maintaining the same ratio would require the arteries to vary their axial stretches, in a Poisson-like effect. Indeed, this response was observed between the femoral and carotid arteries from this study in which the femoral arteries distended less circumferentially but required a greater *in-vivo* axial stretch than the carotid arteries. This behavior highlights the importance of coupling between circumferential and axial stretches in vascular mechanics.

Differences in residual deformations were found between the femoral and carotid arteries through measurements of their opening angles. The femoral arteries exhibited larger opening angles than the carotid arteries and this may be associated with histological differences in their transmural distribution of elastin. Detailed explanation and supporting computational models can be found elsewhere [24]. But it is believed that due to the deposition and cross-linking of elastin during early vascular development followed by normal arterial growth, elastin is subjected to non-uniform pre-stretches across the wall in the matured arterial state [24-26]. As a result, elastin closer to the inner wall experiences higher pre-stretch and tension in the traction-free state than elastin along

the outer wall. The higher pre-stretched elastin recovers more when a stress-free cut is made; this results in smaller opening angles in the carotid arteries where elastin is localized further along the inner wall than in the femoral arteries.

The limitations of this study should be considered when interpreting its findings. First, the ECM is a remarkably complex structure and although collagen and elastin are known to be the dominant structural constituents, the mechanical effects due to the microstructural organization of other ECM components such as proteoglycans, fibronectin, laminin, and fibrillin should be considered as well in future studies [27, 28]. The interaction between the constituents is also another area that warrants further investigation. Second, the mechanical effect of smooth muscle cell (SMC) tone was not considered in this study since measurements were made on arteries in the passive state. Under passive conditions the mechanical role of SMCs are generally not relevant [17], but when active, SMCs can alter a vessel's mechanical behavior and opening angles [29]. This is particularly true of the femoral arteries, which are considered more muscular than the carotid arteries, as seen through the MT stains. Lastly, the results were not matched to the age and gender of the animals. This demonstrates that despite age and gender differences, the mechanical and microstructural differences were still clearly evident between the femoral and carotid arteries.

In summary, this study is the first to our knowledge that identified increased circumferential collagen fiber alignment in the media of femoral arteries compared to carotid arteries from non-human primates. The increased alignment was associated with decreased physiologic compliance of the femoral arteries. Furthermore, elastin was found to be concentrated along the external elastic lamina in the femoral arteries but was evenly

distributed across the media in the carotid arteries. This difference in elastin's transmural distribution was associated with larger opening angles measured in the femoral arteries. Surprisingly, the quantitative content of collagen and elastin were very similar between the two arteries. Relating the microstructural differences to the mechanical behavior of different arteries helps to better understand normal arterial function as well as the susceptibility of certain arteries to disease. An important application of the findings is in the formulation of microstructurally motivated material models that are more physiologically relevant and artery specific. This allows for better prediction of healthy arterial behavior which than can be used for understanding arterial growth and remodeling due to age or disease.

References

1. Bergel, D., *The static elastic properties of the arterial wall.* J Physiol, 1961. **156**(3): p. 445-457.

2. Zieman, S., V. Melenovsky, and D. Kass, *Mechanisms, pathophysiology, and therapy of arterial stiffness.* Arterioscler Thromb Vasc Biol, 2005. **25**(5): p. 932-943.

3. Holzapfel, G., T. Gasser, and R. Ogden, *A new constitutive framework for arterial wall mechanics and a comparative study of material models.* J Elasticity, 2000. **61**(1): p. 1-48.

4. Cheng, J. and J. Wagenseil, *Extracellular matrix and the mechanics of large artery development.* Biomech Model Mechanobiol, 2012: p. 1-18.

5. Wolinsky, H. and S. Glagov, *A lamellar unit of aortic medial structure and function in mammals.* Circ Res, 1967. **20**(1): p. 99-111.

6. Timmins, L., et al., *Structural inhomogeneity and fiber orientation in the inner arterial media.* Am J Physiol Heart Circ Physiol, 2010. **298**(5): p. H1537-H1545.

7. Safar, M., B. Levy, and H. Struijker-Boudier, *Current perspectives on arterial stiffness and pulse pressure in hypertension and cardiovascular diseases.* Circulation, 2003. **107**(22): p. 2864-2869.

8. Hayashi, K., et al., *Stiffness and elastic behavior of human intracranial and extracranial arteries.* J Biomech, 1980. **13**(2): p. 175-179, 181-184.

9. Raninen, R., M. Kupari, and P. Hekali, *Carotid and femoral artery stiffnessin Takayasu's arteritis.* Scand J Rheumatol, 2002. **31**(2): p. 85-88.

10. Burton, A., *Relation of structure to function of the tissues of the wall of blood vessels.* Physiol Rev, 1954. **34**(4): p. 619-642.

11. Benetos, A., et al., *Arterial alterations with aging and high blood pressure. A noninvasive study of carotid and femoral arteries.* Arterioscler Thromb Vasc Biol, 1993. **13**(1): p. 90-97.

12. Armentano, R., et al., *Effects of hypertension on viscoelasticity of carotid and femoral arteries in humans.* Hypertension, 1995. **26**(1): p. 48-54.

13. Gleason, R., et al., *A multiaxial computer-controlled organ culture and biomechanical device for mouse carotid arteries.* J Biomech Eng, 2004. **126**(6): p. 787-795.

14. Zaucha, M., et al., *A novel cylindrical biaxial computer-controlled bioreactor and biomechanical testing device for vascular tissue engineering.* Tissue Eng Pt A, 2009. **15**(11): p. 3331-3340.

15. Weizsäcker, H., H. Lambert, and K. Pascale, *Analysis of the passive mechanical properties of rat carotid arteries.* J Biomech, 1983. **16**(9): p. 703-715.

16. Chuong, C. and Y. Fung, *On residual stresses in arteries.* J Biomech Eng, 1986. **108**(2): p. 189-192.

17. Humphrey, J., *Cardiovascular solid mechanics: cells, tissues, and organs*2002, New York: Springer Verlag.

18. Matsumoto, T. and K. Hayashi, *Stress and strain distribution in hypertensive and normotensive rat aorta considering residual strain.* J Biomech Eng, 1996. **118**: p. 62.

19. Nishimura, T. and M. Ansell, *Fast Fourier transform and filtered image analyses of fiber orientation in OSB.* Wood Sci and Technol, 2002. **36**(4): p. 287-307.

20. Wan, W., J. Dixon, and R. Gleason, *Constitutive modeling of mouse carotid arteries using experimentally measured microstructural parameters.* Biophys J, 2012. **102**(12): p. 2916-2925.

21. Weisstein, E., *Gaussian function.* MathWorld--A Wolfram Web Resource, 2012.

22. Fischer, G. and J. Llaurado, *Collagen and elastin content in canine arteries selected from functionally different vascular beds.* Circ Res, 1966. **19**(2): p. 394-399.

23. Humphrey, J., *Vascular adaptation and mechanical homeostasis at tissue, cellular, and sub-cellular levels.* Cell Biochem Biophys, 2008. **50**(2): p. 53-78.

24. Cardamone, L., et al., *Origin of axial prestretch and residual stress in arteries.* Biomech Model Mechanobiol, 2009. **8**(6): p. 431-446.

25. Greenwald, S., et al., *Experimental investigation of the distribution of residual strains in the artery wall.* J Biomech Eng, 1997. **119**(4): p. 438-444.

26. Wan, W., L. Hansen, and R. Gleason, *A 3-D constrained mixture model for mechanically mediated vascular growth and remodeling.* Biomech Model Mechanobiol, 2010. **9**(4): p. 403-419.

27. Intengan, H. and E. Schiffrin, *Structure and mechanical properties of resistance arteries in hypertension role of adhesion molecules and extracellular matrix determinants.* Hypertension, 2000. **36**(3): p. 312-318.

28. Carta, L., et al., *Discrete contributions of elastic fiber components to arterial development and mechanical compliance.* Arterioscler Thromb Vasc Biol, 2009. **29**(12): p. 2083-2089.

29. Rachev, A. and K. Hayashi, *Theoretical study of the effects of vascular smooth muscle contraction on strain and stress distributions in arteries.* Ann Biomed Eng, 1999. **27**(4): p. 459-468.

CHAPTER 5

THE EFFECT OF PERIVASCULAR SUPPORT ON THE MECHANCIAL BEHAVIOR OF CORONARY ARTERIES

Introduction

The mechanical behavior of an artery is determined by the material properties of the arterial wall as well as the traction forces that the artery experiences, both of which can vary significantly throughout the arterial tree [1]. While the material properties of the wall can be approximated with *in-vitro* mechanical testing and constitutive modeling [2], the traction forces must be measured under *in-vivo* or *in-vivo*-like conditions. This is particularly important for determining the physiologic mechanical environment that arterial cells are exposed to. All conduit arteries experience traction forces of luminal pressure and axial stretch, and these are normally taken into consideration with mechanical testing (i.e., cylindrical biaxial inflation-extension tests). However, certain arteries may have additional mechanical factors that are more difficult to quantify. One such factor is the perivascular support (PS), the tissue surrounding the artery, which has been largely overlooked in arterial mechanics [3]. Studies having examined PS have shown that its mechanical effect on the artery can be significant [4-9].

All blood vessels are encased in PS, but the mechanical influence of the support can vary depending on the location of the vessel along the vascular tree. For instance, aortas and cerebral arteries are minimally supported, but other disease prone arteries such as the femoral, carotid, and coronary arteries are encased in thick PS. Numerous studies have utilized *in-vitro* mechanical testing to characterize the mechanical properties of

these arteries. *In-vitro* mechanical testing requires isolating the artery from its native tissue bed, thus neglecting the mechanical role of PS and potentially inducing errors when predicting the mechanical behavior [3].

Clinically motivating factors exists as well for studying PS. Increase in coronary perivascular adipose volume has been correlated to metabolic syndrome and atherosclerotic plaque burden [10, 11]. In cases of intramyocardial bridging, where segments of the artery tunnel through the myocardium and become completely encased by the cardiac muscle, there is an absence of atherosclerotic lesions despite the presence of lesions in proximal segments [12, 13]. Quantifying the mechanical effect of PS on the coronary artery can create new insights for understanding the mechanisms behind these clinical observations.

The coronary arteries are generally embedded between soft adipose tissue and stiff cardiac muscle (**Figure 5.1**). The PS transmits the deformations of the heart to the artery, resulting in compression, twisting, and bending of the artery [14]. More importantly, numerical modeling has shown that perivascular support can significantly restrict the dilation and axial stretch of the artery [7].

The geometric boundaries of the PS are not well defined and the PS cross-section is likely not axisymmetric (**Figure 5.1**), therefore excising an appropriate and consistent tissue for mechanical testing may be difficult. As such, to accurately quantify the effects of PS in the coronary arteries, experimental measurements must be performed on the artery in its native perivascular environment (i.e., the *in-situ* state).

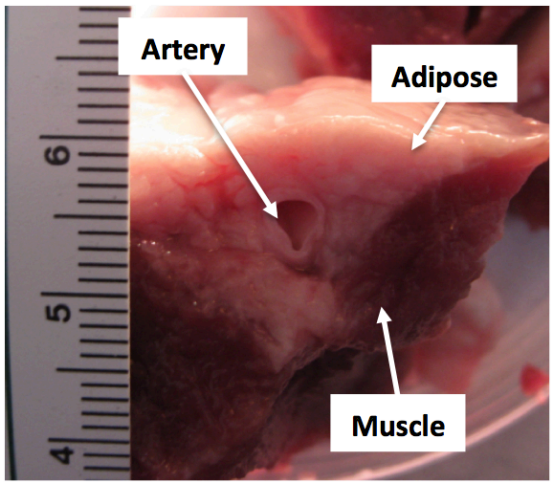

Figure 5.1: A coronary artery encased in PS. The PS consists of thick adipose tissue resting in the coronary channel. Beneath the PS lies the stiff myocardium. The PS clearly does not exhibit axisymmetry around the artery.

This study aims to determine the pressure-diameter (*p-d*) response of the coronary artery in three configurations through sequentially isolating the artery from its *in-situ* perivascular environment. These configurations are: 1) *in-situ*, in which the artery is undisturbed in its perivascular environment, 2) partially dissected, in which the perivascular support around the segment of interest is manually dissected away, exposing the artery but leaving the axial tethering intact, and 3) *in-vitro*, in which the PS is fully dissected away and the artery is removed from the heart for *in-vitro* mechanical testing using a cylindrical biaxial stretching device. Additionally, the local axial stretches between the *in-situ* and traction-free state of the artery are measured. This is compared to the *in-vivo* axial stretch predicted by *in-vitro* mechanical tests.

Methods

Tissue Harvest and Preparation

Ten intact porcine hearts of similar size and weight were freshly harvested at a local slaughterhouse (Holifield Farms, Covington, GA) from female American Yorkshire farm pigs (2 years of age). The coronary vasculature was immediately flushed with cold Ca^{+2} and Mg^{+2}-free Dulbecco's phosphate buffered saline (DPBS) through aortic cannulation. The hearts were transported in an ice-chilled environment to the laboratory. Five hearts were used for *p-d* testing and five hearts used for the local axial stretch measurements.

Measurement of Local Axial Stretches

The top surface of the left anterior descending coronary artery (LADCA) was carefully exposed with a thin incision through the perivascular tissue (**Figure 5.2**). Small spherical fiducial markers (< 1 mm) were adhered to the surface of the artery with cyanoacrylate applied through the tip of a 27-gauge needle. Six to eight markers were applied along the centerline of the artery spaced 5 – 10 mm apart starting at the root of the LADCA.

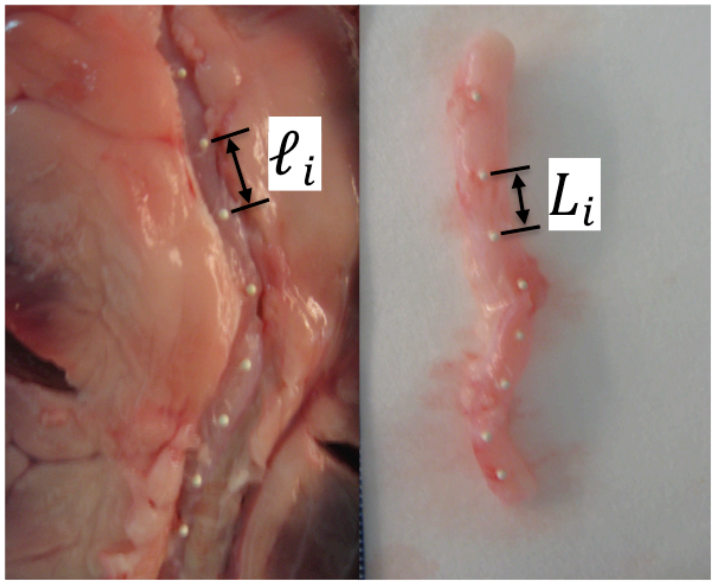

(A) **(B)**

Figure 5.2: Markers for measuring local axial stretch ratios. Fiducial markers are glued to the top surface of the coronary artery. (**A**) The artery is in its *in-situ* configuration, still embedded in the heart. (**B**) The same artery is excised from the heart after markers are applied. The marker distances are measured in both configurations to calculate local axial stretch ratios.

The actual distances (ℓ_i) between each pairs of markers, i and $i+1$, were measured manually using a digital caliper. Perivascular tissue was then completely dissected away, the artery excised from the heart and placed in a DPBS bath at 37 ^{o}C for three hours to achieve geometric equilibrium. The traction-free distances (L_i) between the same pairs of markers were then measured. The local *in-situ* axial stretch ratio is defined as $\lambda_i^* = \ell_i / L_i$.

Pressure – Diameter Measurement *In-Situ*

The *p-d* response was assessed in the LADCA sequentially with and without perivascular support. The arterial lumen was imaged noninvasively using intravascular ultrasound (IVUS) while being pressurized under controlled quasi-static loading

conditions. IVUS is a radially projecting catheter-based ultrasound imaging modality that can be inserted into the lumen. Approximately two-thirds of the LADCA was cannulated using barbed three-port polycarbonate fittings (**Figure 5.3**). Pressure transducers (PT-F/PM-4, Living Systems Instruments) were connected to an opened port on each end. The remaining open port on the aortic end was connected to a computer-controlled syringe pump (PHD2000, Harvard Apparatus), which was used pressurize the artery. The remaining open port on the apical end was connected to a one-way access sheath that allowed the IVUS transducer (Visions PV .018 20MHz, Volcano) to be inserted into the arterial lumen without losing pressure. The tubing was sufficiently large to accommodate the IVUS transducer wire while not obstructing the pressure transducer. The IVUS transducer was secured approximately equal in distant between the two pressure transducers at an axial location where the artery was noticeably encased in perivascular fat. A series of vascular clips and ligatures were used to stop outflows from peripheral branches. During testing, the heart was partially submerged in a DPBS bath maintained at 37 ^{o}C. The segment with the IVUS transducer was kept above the bath due to concerns of hydrostatic pressure compressing the artery.

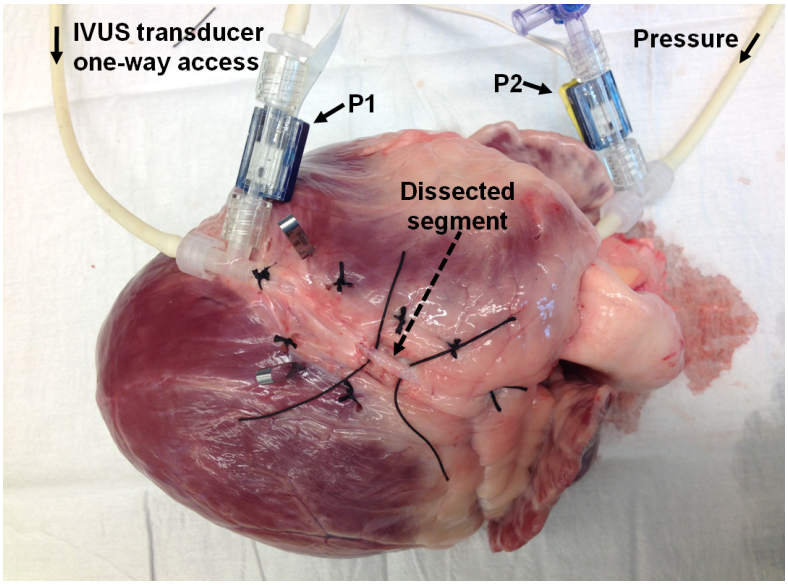

Figure 5.3: Partial experimental setup for measuring the *p-d* response of the coronary artery *in-situ*. Two pressure transducers (P1 and P2) are cannulated to the LADCA. Pressure is controlled using a computerized syringe pump (not shown). The IVUS transducer is introduced into the artery through a one-way port and rests in the center of the dissected segment. A series of ligatures and vascular clips are used to stop outflows from peripheral branches. During testing, the heart is partially submerged in a DPBS bath maintained at physiological temperature.

With the perivascular tissue intact, the artery was preconditioned with several pressurization cycles from 0 – 90 mmHg; this was followed by four additional cycles during which the lumen was imaged using IVUS. The perivascular tissue around the catheter was than carefully dissected away, leaving a 1 – 1.5 cm length of the LADCA partially exposed but still axially tethered (**Figure 5.3**). The *p-d* measurement protocol for the *in-situ* configuration was repeated for the dissected configuration. In both the *in-situ* and dissected configurations the IVUS transducer was fixed at the same axial location, this allowed for a direct comparison of diameters without the need for normalization. IVUS images were collected at 23 frames/sec.

In-Vitro Biaxial Mechanical Testing

Following the *in-situ* measurements, the PS around the entire cannulated length of the artery was removed by dissection, and the exposed peripheral branches were ligated using 6-0 silk sutures. The artery was then cut from the heart and mounted on a custom mechanical tester and subjected to biaxial loading conditions (inflation – extension). The artery underwent cyclic pressurizations between 0 – 90 mmHg at fixed axial lengths while the outer diameter and axial force were monitored. The axial length of the artery was incrementally increased until the axial force became independent of the lumen pressure. Based on established methodologies [15], this configuration is generally considered to be the *in-vivo* axial stretch of the artery. One caveat is that the *in-vitro* test measured the outer diameter of the artery while IVUS measured the inner diameter. To resolve this discrepancy, the assumption of an incompressible arterial wall was invoked to calculate the *in-vitro* inner diameter with equation (4.1):

$$d_i = \left[d_o^2 - \frac{1}{\lambda_z}(2HD_o - H^2) \right]^{1/2} \tag{4.1}$$

where d_i and d_o are the current inner and outer diameters, respectively, λ_z is the axial stretch ratio, D_o is the traction-free outer diameter, and H is the traction-free wall thickness [3].

Lumen Segmentation

A semi-automated GUI routine was developed to segment the lumen boundary using the IVUS DICOM images. To expedite the process, an image was sampled at every 20 frames. For each image, 15 equally spaced points were manually selected around the lumen boundary using an overlaid grid as reference. These points were fitted to an ellipse

using a robust least-squares regression fitting algorithm [16], and the ellipse was used to calculate a nominal lumen diameter. In general the lumen shape was circular. However, at low pressures (< 20mmHg), the arterial wall either buckled or shifted the transducer's centerline, resulting in excessive noise and the inability to accurately delineate the lumen boundary. As such, measurements below 20 mmHg were not used in the results. The IVUS images were synchronized to the measurements from the pressure transducers using the local time stamps provided by the internal clocks of the respective controlling computers.

Statistical Analysis

Multiple independent means were analyzed using ANOVA. Student's *t*-test was used to analyze significance between two means. The significance threshold was $P < 0.05$. Statistical analysis, post-processing, and plotting were performed using commercial software Excel (Microsoft) and MATLAB (MathWorks).

Results

Measurement of Local Axial Stretches

The local axial stretch ratios (λ_z^*) varied widely across the arteries, ranging from 1.01 to 1.70 (**Figure 5.4A**). Linear regression of the data revealed poor correlation between the local stretch ratios and axial locations ($R^2 = 0.05$). The mean axial stretch ratio averaged across all the arteries was 1.28 ± 0.10 (mean ± SD). Averaging the local stretch ratios for each artery revealed two arteries that exhibited significantly lower values (**Figure 5.4B**).

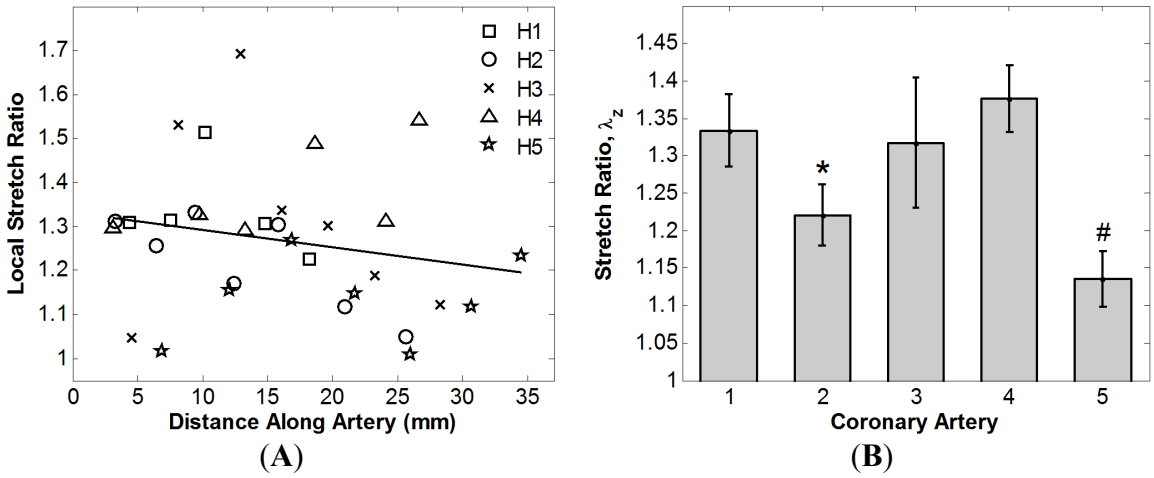

Figure 5.4: Measurements of the local axial stretch ratios. (**A**) Measurements are made along the length of the coronary artery (n = 5). The LADCA root serves as the reference point for the distance along the artery. Linear regression of the data (black line) yields goodness-of-fit of R^2 = 0.05. Each symbol type indicates the same artery. (**B**) The mean axial stretch ratios from each artery exhibit significant artery-to-artery variability (results are mean ± SEM, *P < 0.05 compared to 1, 2, and 4; #P < 0.01 compared to 1 3, and 4, ANOVA).

Pressure – Diameter Measurement *In-Situ*

Following the partial dissection of the PS, the lumen dilated more compared to the *in-situ* configuration when subjected to the same pressures (**Figure 5.5A**). The increase in the lumen diameter was significant for pressures 20 – 60 mmHg. The differences in the diameters appeared to decrease as pressure increased (**Figure 5.5B**).

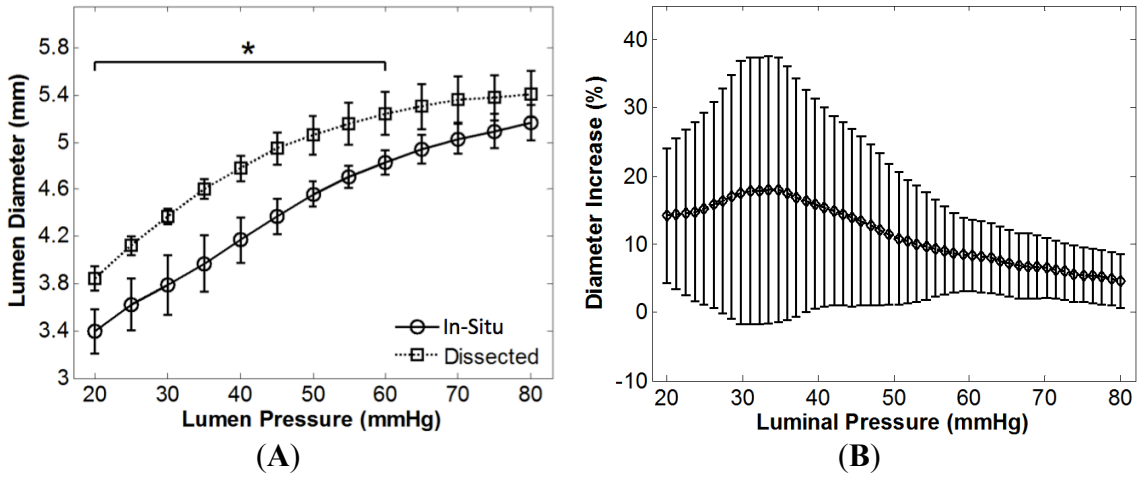

Figure 5.5: Comparison of *in-situ* and dissected responses. (**A**) The *p-d* response of the LADCA assessed *in-situ* at the same axial location with intact perivascular support (circle solid line) compared to dissected support (square dotted line). A significant increase in diameter is observed for pressures between 20 – 60 mmHg (results are mean ± SEM, $*P < 0.05$, one-tailed *t*-test). (**B**) The difference between the *in-situ* and dissected diameters appears to decrease with increasing pressure, but this trend is not statistically significant (results are mean ± SD).

In-Vitro Biaxial Mechanical Testing

The *in-vivo* axial stretch ratio determined using the *in-vitro* pressure-force response was 1.30 ± 0.08. Interesting, this was comparable to the averaged value from all the local stretch ratios (1.28 ± 0.10). The *in-vitro p-d* response exhibited appreciable differences compared to both the *in-situ* and dissected responses (**Figure 5.6A**). For comparative purposes, the diameters were normalized to the traction-free inner diameter. At high pressures, the *in-vitro* response exhibited greater strain stiffening and the compliance difference between the *in-vitro* and dissected configurations was minimized; both however were significantly less compliant than the *in-situ* configuration.

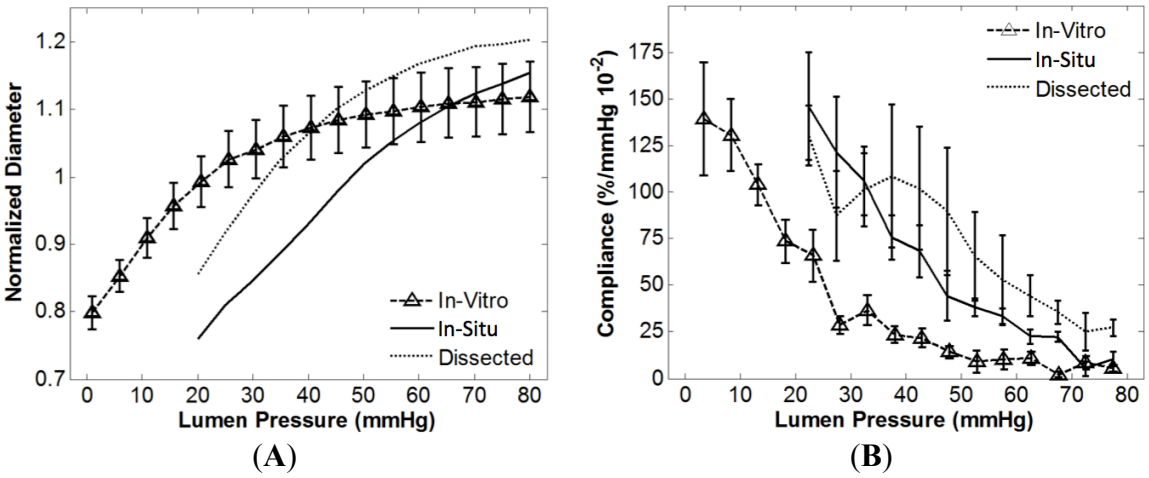

Figure 5.6: Comparison of *in-vitro* and *in-situ* mechanical responses. (**A**) The *in-vitro* *p-d* response (triangle markers) exhibits appreciable differences compared to both the *in-situ* and dissected responses (only the mean is plotted for presentation purposes). (**B**) The difference in mechanical response is confirmed in the local compliances. The *in-vitro* response is less compliant over all. However, at higher pressure, both the *in-vitro* and dissected responses are equally less compliant than the *in-situ*.

Discussion

The coronary arteries are well encased in PS. The PS can significantly modulate the mechanics of the encased artery and this study represents the first experimental measurements of those mechanical effects. The *p-d* response of the arteries was first measured in their native *in-situ* perivascular environment. The PS was then dissected away, and the *p-d* testing repeated in the dissected configuration. We found that by removing the PS, the artery distended more, confirming our hypothesis that PS does indeed restrict the dilation of the coronary artery. The difference in distension appeared to be greatest at lower pressures and decreased with increasing pressure. However, note that at high pressures, small differentials between the *in-situ* and dissected diameters can represent a significant perivascular pressure (P_p) due to the nonlinear *p-d* response (**Figure 5.7**).

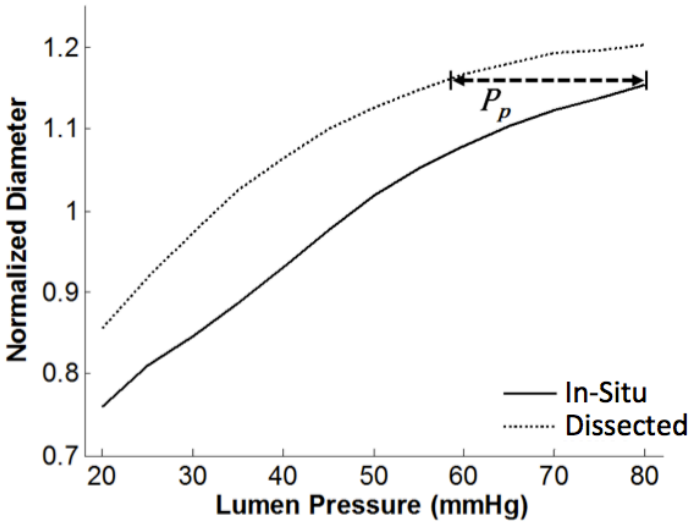

Figure 5.7: Approximation of the perivascular pressure from *p-d* responses. Note that the perivascular pressure is not constant with lumen pressure since the curves exhibit slightly different trends. At the highest pressure of 80 mmHg, the perivascular pressure is the pressure difference across the dashed line, $P_p \approx 24$ mmHg.

Transmural Pressure

This study also investigated differences in the mechanical response between the *in-situ* and *in-vitro* configurations to determine if *in-vitro* biaxial loading conditions were appropriate for reproducing *in-situ* conditions. We found that the *in-vitro* response exhibited significantly less compliance than the *in-situ*. This finding suggested that *in-vitro* testing may be over-prescribing luminal pressure or axial stretch (due to the coupling of finite stretches, axial stretch can affect the circumferential response). The *p-d* response was dependent on the artery's transmural pressure ΔP, where $\Delta P = P_i - P_p$, however *in-vitro* testing commonly assumes that the transmural pressure and luminal pressure are equal ($\Delta P = P_i$) since removing the PS for *in-vitro* testing inherently force $P_p = 0$. However, if there is significant P_p, than the *in-situ* transmural pressure is smaller than the luminal, resulting in the over-pressurization of the artery *in-vitro*. Humphrey

made this logical deduction more than a decade ago [17], and this study confirms his speculations.

Local Axial Stretches

Averaging the local stretch ratios across all the arteries resulted in a mean stretch ratio that was comparable to the estimated *in-vivo* values determined through biaxial testing [18, 19]. However, examined individually, the local axial stretch ratios exhibited wide variability along the length of the artery. Axial stretch of the artery *in-vitro* subjects the entire artery to the same stretch (assuming minimal axial variations in material property and geometry); as a result, local areas that may have experienced lower or higher axial stretches *in-situ* become over or under-stretched *in-vitro*, respectively, which can translate to an over or under-stretch response in the circumferential direction due to coupling of finite stretches. However, since the local stretch ratios of the *in-situ*/dissected segments were not measured, this assumption remains to be investigated. Spatial heterogeneity in the growth of the heart or differences in the mechanical properties of the underlying PS may be a potential mediator of the variability in the local stretches.

Low-Pressure Response

At low pressures (< 20 mmHg), the arteries collapsed around the IVUS transducer, resulting in the inability to properly identify the lumen boundary (**Figure 5.8**). This effect was consistent for all arteries in both the *in-situ* and dissected configurations. We verified that in the traction-free state the coronary arteries stay open effortlessly and the diameter of the transducer was less than the traction-free inner

diameters of the arteries. Therefore it was apparent that the PS compressed the artery around the transducer in the *in-situ* configuration. However, it was interesting to note the same effect in the dissected configuration, since removing the PS should have allowed the artery to stay open. We believe this may be due to boundary effects of the dissected section. First, since a short length (1 – 1.5 cm) of the artery was dissected, perivascular compressions of the artery at the dissected ends were not far enough from the measurement location, thereby compressing the measurement location as well. Second, there may have been PS remnants on the artery, particularly on the bottom (towards the myocardium) of the artery. The bottom was difficult to dissect cleanly without overstretching and damaging the artery.

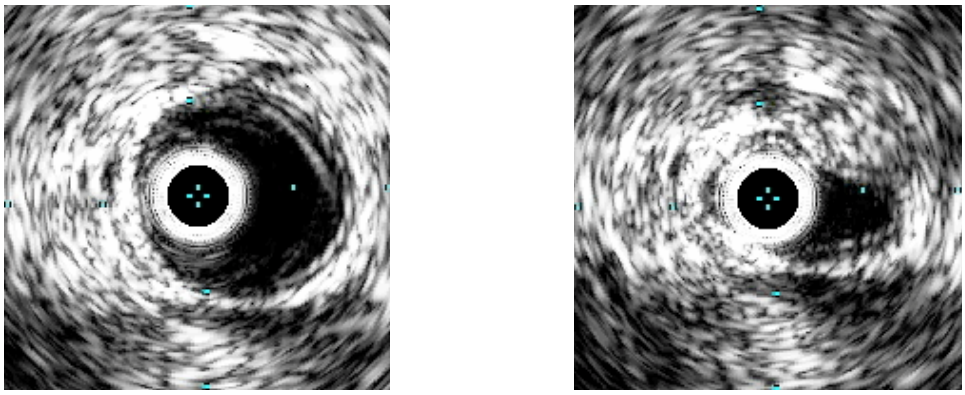

(**A**) (**B**)

Figure 5.8: Collapse of the coronary artery around the IVUS transducer. (**A**) An artery with the lumen clearly open. (**B**) As the lumen pressure decreases to below 20 mmHg, the artery begins to collapse around the transducer. The transducer diameter is smaller than the traction-free inner diameter of the artery.

With the low-pressure dissected response aside, it is evident from the *in-situ* response that an initial pressure is needed to 'open' the artery prior to inflating. By

shifting the *in-situ p-d* response to the left, this initial opening pressure can be disregarded (**Figure 5.9**). The resulting responses appear strikingly similar.

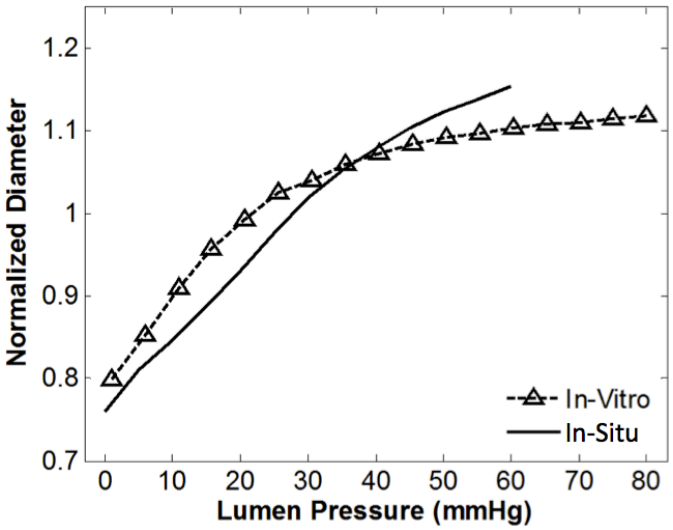

Figure 5.9: Cross-correlation of the *in-vitro* and *in-situ p-d* responses. The *in-situ* response matches well with the *in-vitro* after being shifted 20 mmHg towards 0 mmHg to eliminate the opening pressure.

The current study directly assessed the mechanical effect of PS on the coronary artery. Future studies should focus on creating models that can predict this effect utilizing material models of the PS. This approach can offer great insights on the changes in arterial mechanics due to geometric or material changes of the PS, for instance with ventricular hypertrophy or obesity-related increase in perivascular fat. In general, the immediate perivascular environment of the coronary arteries consists of adipose tissue, a very soft material. However, the adipose tissue is sandwiched between significantly stiffer materials, the visceral pericardium (epicardium [20]) and the myocardium . Thus, it is unlikely that the constrictive effect of the PS is due to the adipose tissue alone. Jobsis *et al.* showed that disabling the visceral pericardium via blunt dissection resulted in an

appreciable shift of the pressure-volume curve of the heart [21]. Therefore, the mechanics of the PS may be mediated through the material properties and interactions of several perivascular constituents. A holistic mechanical model of the PS would require the knowledge of the material properties of these individual constituents as well as their mechanical interactions.

References

1. Megens, R., et al., *Two-photon microscopy of vital murine elastic and muscular arteries.* Journal of vascular research, 2007. **44**(2): p. 87-98.

2. Stegemann, J.P., H. Hong, and R.M. Nerem, *Mechanical, biochemical, and extracellular matrix effects on vascular smooth muscle cell phenotype.* Journal of applied physiology, 2005. **98**(6): p. 2321-2327.

3. Humphrey, J., *Cardiovascular solid mechanics: cells, tissues, and organs* 2002, New York: Springer Verlag.

4. Fung, Y., B.W. Zweifach, and M. Intaglietta, *Elastic environment of the capillary bed.* Circulation research, 1966. **19**(2): p. 441-461.

5. Patel, D.J., D.L. Fry, and J.S. Janicki, *Longitudinal tethering of arteries in dogs.* Circulation research, 1966. **19**(6): p. 1011-1021.

6. Singh, S. and L.S. Devi, *A study on large radial motion of arteries in vivo.* Journal of biomechanics, 1990. **23**(11): p. 1087-1091.

7. Liu, Y., W. Zhang, and G.S. Kassab, *Effects of myocardial constraint on the passive mechanical behaviors of the coronary vessel wall.* American Journal of Physiology-Heart and Circulatory Physiology, 2008. **294**(1): p. H514.

8. Liu, Y., et al., *Surrounding tissues affect the passive mechanics of the vessel wall: theory and experiment.* American Journal of Physiology-Heart and Circulatory Physiology, 2007. **293**(6): p. H3290.

9. Steelman, S.M., et al., *Perivascular tethering modulates the geometry and biomechanics of cerebral arterioles.* Journal of biomechanics, 2010. **43**(14): p. 2717-2721.

10. Verhagen, S.N. and F.L.J. Visseren, *Perivascular adipose tissue as a cause of atherosclerosis.* Atherosclerosis, 2011. **214**(1): p. 3-10.

11. Mahabadi, A.A., et al., *Association of pericoronary fat volume with atherosclerotic plaque burden in the underlying coronary artery: a segment analysis.* Atherosclerosis, 2010. **211**(1): p. 195-199.

12. Mohlenkamp, S., et al., *Update on myocardial bridging.* Circulation, 2002. **106**(20): p. 2616-2622.

13. Noble, J., et al., *Myocardial bridging and milking effect of the left anterior descending coronary artery: normal variant or obstruction?* The American journal of cardiology, 1976. **37**(7): p. 993-999.

14. Armentano, R., et al., *Effects of hypertension on viscoelasticity of carotid and femoral arteries in humans.* Hypertension, 1995. **26**(1): p. 48-54.

15. Weizsäcker, H., H. Lambert, and K. Pascale, *Analysis of the passive mechanical properties of rat carotid arteries.* J Biomech, 1983. **16**(9): p. 703-715.

16. Fitzgibbon, A., M. Pilu, and R.B. Fisher, *Direct least square fitting of ellipses.* Pattern Analysis and Machine Intelligence, IEEE Transactions on, 1999. **21**(5): p. 476-480.

17. Humphrey, J. and K. Rajagopal, *A constrained mixture model for growth and remodeling of soft tissues.* Mathematical models and methods in applied sciences, 2002. **12**(03): p. 407-430.

18. Wang, C., et al., *Three-dimensional mechanical properties of porcine coronary arteries: a validated two-layer model.* American Journal of Physiology-Heart and Circulatory Physiology, 2006. **291**(3): p. H1200.

19. Pandit, A., et al., *Biaxial elastic material properties of porcine coronary media and adventitia.* American Journal of Physiology-Heart and Circulatory Physiology, 2005. **288**(6): p. H2581-H2587.

20. Humphrey, J., R. Strumpf, and F. Yin, *Biaxial mechanical behavior of excised ventricular epicardium.* American Journal of Physiology-Heart and Circulatory Physiology, 1990. **259**(1): p. H101-H108.

21. Jobsis, P.D., et al., *The visceral pericardium: macromolecular structure and contribution to passive mechanical properties of the left ventricle.* American Journal of Physiology-Heart and Circulatory Physiology, 2007. **293**(6): p. H3379-H3387.

CHAPTER 6

CLOSURE AND LIMITATIONS

Closure

This study is aimed at furthering the mechanistic understanding of arterial behavior and function across different length scales. Novel theoretical frameworks and experimental methodologies were utilized to investigate the intrinsic and extrinsic mechanically factors of the arterial wall.

First, we found that residual deformations, an essential link between the artery's mechanical behavior and biological adaptation, cannot be fully described using a single measurement. Longitudinal residual deformations were shown to be significant in the coronary and carotid arteries and shearing residual deformations were found to be unique to the coronary arteries. Both types of residual deformations contributed significantly to the local mechanical environment when incorporated into the stress analysis.

Second, we found significant differences in the microstructural dispersion of collagen fibers and the transmural distribution of elastin in the media of femoral and carotid arteries from non-human primates. Collagen fibers in the femoral arteries were considerably more aligned in the circumferential direction (direction of strain) than ones found in the carotid arteries. Elastin layers were evenly distributed in the carotid arteries but were concentrated along the external elastic lamina in the femoral arteries. Mechanical testing of the arteries revealed that the femoral arteries were stiffer, but quantitative assays found insignificant differences in the content of collagen and elastin between the femoral and carotid arteries. This suggested that the minute but significant

differences in medial collagen alignment might be associated with the differences in the stiffness between the arteries.

Lastly, perivascular support was found to contribute significantly to the mechanical response of the coronary arteries. This study was the first to experimentally measure the effect of coronary perivascular support by determining the pressure-diameter response of the artery *in-situ* and then again after surgical exposure of the artery. We found that the perivascular support pressure acting against the artery is equivalent to a pressure as high as 24 mmHg. Given that coronary arteries are only exposed to diastolic pressures, this perivascular pressure represents a significant amount of mechanical constriction. Furthermore, this study determined that *in-vitro* mechanical testing might be over-inflating the artery and thus observing a much stiffer response than the *in-vivo* levels.

Limitations

Several limitations have been addressed in each chapter. However, a few limitations should be reemphasized in order to properly evaluate the findings of this study.

First, vasotone was not considered. All specimens were kept in Mg^{+2} and Ca^{+2}-free solutions. Although the passive response of arteries is largely determined by the ECM milieu, the physical presence of SMC (the structural constituents and tethering of the cells) may continue to exhibit mechanical contributions. This deactivated passive response of the SMC on the overall mechanical behavior is unknown and could be significant in muscular arteries, thus warranting further investigations.

Second, the use of animal tissues is a well-accepted limitation in biomechanics. Healthy human tissues are scarce and difficult to procure. However, there should always be a concerted effort to use tissues that closely mimic their human counterparts. In this study we have utilized porcine hearts, which are very similar in geometry to human hearts, as well as non-human primate arteries. The use of these tissues allow for greater physiological relevancy, however they are still not equal to native human tissues.

Despite these limitations, this study advances the fundamental mechanical understanding of arteries and provides mathematical and experimental frameworks for future studies.

CHAPTER 7

FUTURE CONSIDERATIONS

Introduction

The mechanical behavior of arteries is determined by numerous intrinsic and extrinsic components as well as the interactions between those components, some of which have been presented in this work. Two projects that serve as exciting complements to this body of work are quantifying the uncrimping dynamics of collagen fibers and developing a device for measuring the mechanical properties of perivascular adipose tissue.

In Chapter 3, a FFT approach was utilized to extract the distribution of fiber angles from TPEM images of collagen fibers in the arterial media. FFT analysis is most effective on straight fibers and the largely chaotic nature of undulating collagen fibers is difficult to quantify. Determining the organization and in particular the engagement of undulating fibers are important for formulating physiologically relevant constitutive models [1, 2]. Currently, manual tracing is the only reported method of quantifying the undulations [3, 4]. However, this method is tedious and can only sample a limited number of discrete fibers. This preliminarily study presents an automated method of indirectly quantifying the uncrimping of collagen fibers across a region of interest (ROI) using digital image correlation (DIC).

The second project involves the development of a novel uniaxial compression tester for determining the mechanical properties of perivascular adipose tissue around the coronary arteries. We have shown in Chapter 4 that perivascular support can significantly

modulate the mechanical behavior of the artery. We also discussed the need to characterize the mechanical properties of the perivascular support in order to construct mechanical models for computationally assessing the mechanical effect of perivascular support without resorting to experimentation. Although the mechanical properties of the myocardium [5-8] and visceral pericardium [9-11] have been well investigated, little is known about perivascular adipose tissue. Perivascular adipose tissue is a very soft material and is not suited for traditional tensile testing, as it does not respond well to clamping or suturing. Numerous studies investigating other very soft tissues (VST) such as brain [12, 13], kidney, liver [14], breast, and prostate [15] have utilized uniaxial compression testing to determine the material properties. An isotropy assumption is made in many of these studies without fully validating the assumption. However, given that most soft tissues are not isotropic, mechanically testing perivascular adipose tissues would first require the understanding of the material response.

Quantifying the Uncrimping of Collagen Fibers

This study presents the use of DIC to quantify the uncrimping dynamics of collagen fibers in the arterial adventitia. DIC is an optical measurement technique that can track local displacements on a deforming surface by cross-correlating sequential image subset pairs [16, 17]. The effectiveness of the DIC algorithm is dependent on having 1) stochastic patterns on the material surface and 2) small displacements and strain-rates. The first requirement is inherently satisfied in TPEM images of arterial collagen. Furthermore, due to the acquisition time (~2 min/image) of TPEM, the artery is inflated in stepwise pressurization scheme, effectively eliminating any strain-rate. By

reducing the pressure increments between each loading point, the displacements can be controlled. Taken together, DIC can serve as a powerful tool for understanding the dynamics of collagen fibers.

Methods

A right common femoral artery was excised from a non-human primate at necropsy. The artery was first mechancically tested under biaxial loading conditions (see Chapter 4) to determine its *in-vivo* axial stretch. The artery was then mounted on a biaxial stretching device designed to fit onto the stage of a confocal microscope, where it was axially stretched to the determiend *in-vivo* stretch. Second-harmonic generation images of collagen were collected at each pressure (see Chapter 4 for settings and detailed imaging protocol). The focal plane was manually adjusted to keep a set of reference fibers in view. Pressure was increased at increments of 5 mmHg until 50 mmHg, afterwhich it was increased at 10 mmHg until 120 mmHg.

DIC was performed between consecutive image pairs using open-source software (OpenPIV). The magnitudes of the displacment vectors (pixel units) between image pairs were averaged into a into a single value. The DIC analysis was compared to the percent engagment of the three reference fibers that were manually traced using ImageJ (National Institute of Health). The engagement percentage was calculated based on a ratio of the fiber's chord length (yellow line) to total length (red line). The fiber is assumed to be fully engaged (100%) when the two lengths are equal (**Figure 7.1**). Once fully engaged, FFT analysis (see Chapter 4) was applied to the images to determine the presence of fiber rotations.

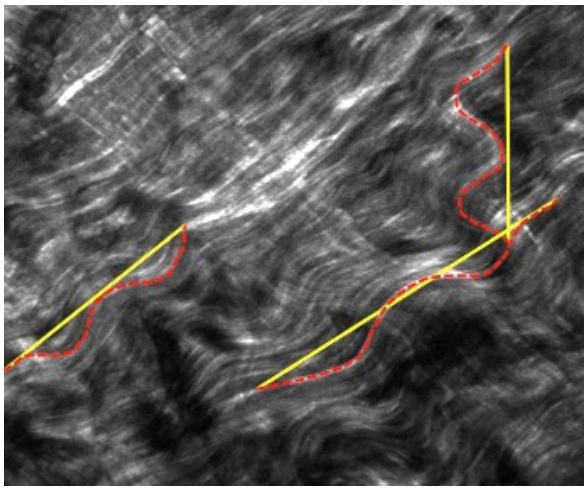

Figure 7.1: Crimped collagen fibers in the adventitia. Individual fibers are tracked while artery is being pressurized. Fiber engagements are determined based on the ratio of the chord length (solid lines) to total fiber length (dashed lines). Complete fiber engagement occurs when the ratio becomes one.

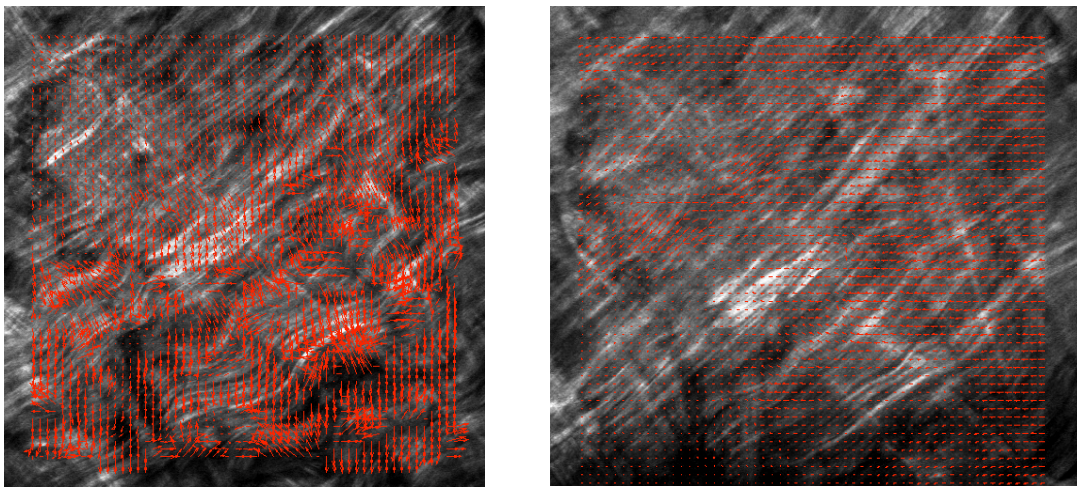

(**A**) (**B**)

Figure 7.2: Displacement vector fields of collagen fibers with loading. (**A**) at low pressures, the collagen fibers are undulating and the tissue is more elastic, therefore higher displacements are observed. (**B**) At high pressures, the tissue stiffens considerably and the displacements become very small.

Results

Initial biaxial mechanical testing determined the *in-vivo* axial stretch for the femoral artery to be $\lambda_z = 1.35$. The three fibers that were tracked manually achieved nearly 100% engagement by 20 mmHg (**Figure 7.3A**). This compared well with the DIC results, which showed large displacements up to 20 mmHg, after which displacement were maintained at a low basal level. Interestingly, the complete engagement threshold is well within the elastic region of the pressure-diameter curve (**Figure 7.3B**). FFT analysis revealed an increase in fiber rotation following complete engagement (**Figure 7.3C**).

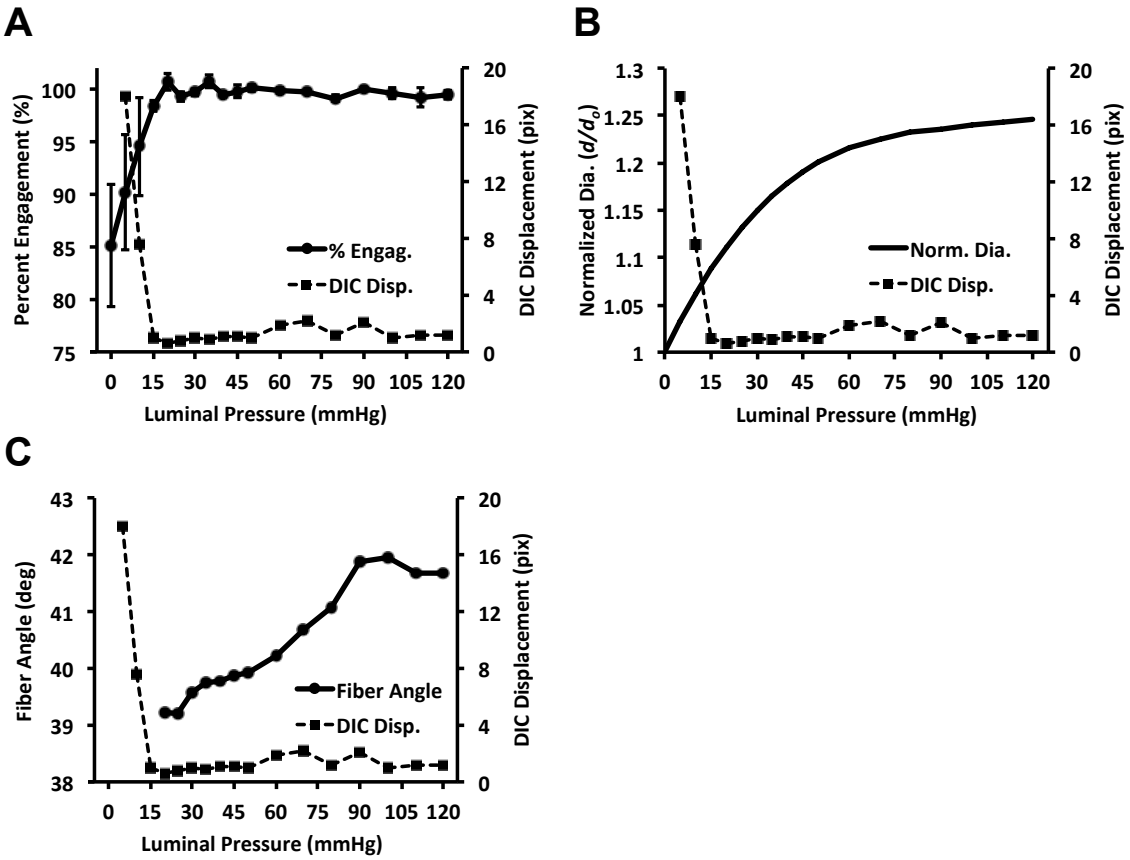

Figure 7.3: Uncrimping dynamics of collagen fibers. (**A**) DIC and manual tracing of the fibers achieved similar collagen engagement thresholds at around 20 mmHg. Peaks in the DIC displacements are observed at 60-75 mmHg and 90 mmHg due to the translation of the images. (**B**) Total engagement of collagen at 20 mmHg is within the elastin range of the pressure-diameter curve. (**C**) Following complete engagement, the fibers rotate until physiologic pressures.

Discussion

This preliminary study presented the development and initial validation of a method to assess collagen uncrimping using DIC and TPEM. The results indicate that collagen fibers became engaged at 20 mmHg, a much lower pressure than anticipated. Once engaged, the fibers exhibited rotation and some translation. There several key limitations that we have already began to address. First, the images can undergo rigid body translation if the focal point is not aligned with the centerline of the artery.

Reference points, such as implanting small fluorescent fiducial beads, can be used to eliminate the translation during post-processing. These beads can also help to maintain a consistent focal plane, which currently is accomplished by tracking fibers with unique characteristics.

Mechanical Testing of Perivascular Fat

This study presents a novel testing apparatus for use in determining the mechanical response of coronary perivascular fat subjected to uniaxial compressive loads. In addition to characterizing the uniaxial mechanical properties, the device can assess the planar anisotropic behavior of the specimen. Initial validation of the tester was performed using cardiac adipose tissue and isotropic rubber as the control.

Methods

The components of the tester (**Figure 7.4**) consist of a load cell (XLU68s, Delta Metrics, 0.1% accuracy 250 grams) coupled to a linear actuator (LTA-HS, Newport). An upper platen, which is attached to the load cell, is coated with a dark Teflon tape. The specimen bath consists of an optically clear dish filled with DPBS. The bath can either be heated to physiologic temperatures using a benchtop temperature controller (CSC32, Omega) or the entire device can be housed inside a temperature-controlled CO_2 incubator. Beneath the bath is a high-speed digital video camera (Marlin F-033, Allied Vision) with a partially-telecentric lens (55mm FL, Edmund Optics). The specimen bath is illuminated from above using two fiber optic light guides (**Figure 7.4C**). Data

collection and device control are performed through a custom LABVIEW routine and data acquisition unit (USB NI-6039, National Instruments).

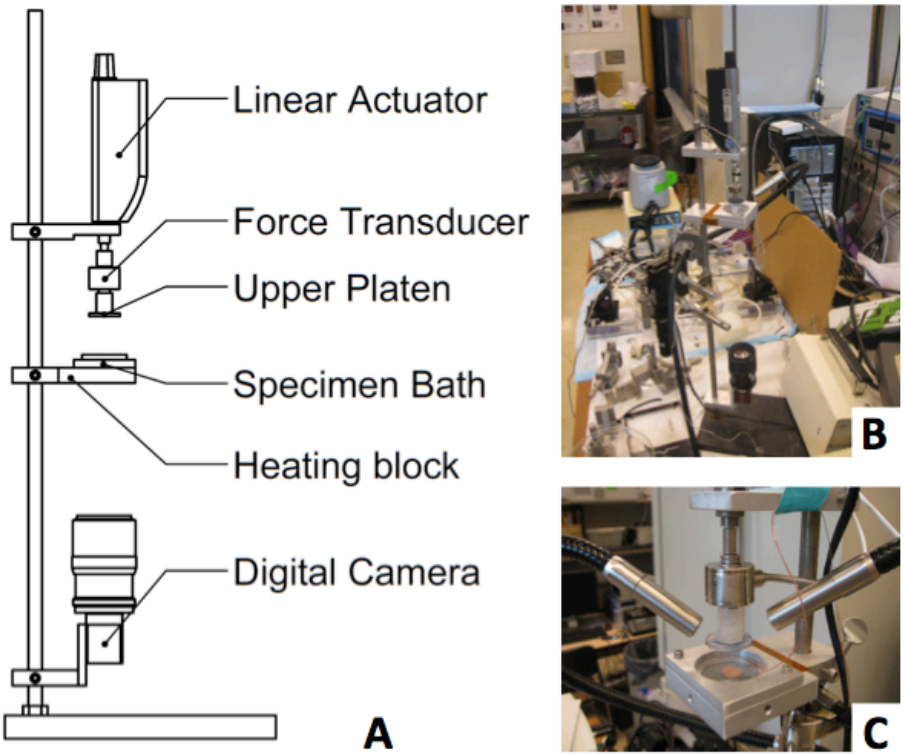

Figure 7.4: A novel uniaxial compression tester for characterizing the mechanical behavior of soft adipose tissue. (**A**) Components of the tester are labeled accordingly. The digital camera captures the compressed area of the specimen during testing. (**B**) Overall view of the actual tester. (**C**) View of the specimen bath and upper platen attached to the force transducer.

The camera monitors the compressed surface while upper platen is lowered. A LABVIEW routine implements an automated edge detection algorithm inline to determine the current perimeter and area of the specimen. A direct least squares fitting of the perimeter to an ellipse is performed during post-processing [4] (**Figure 7.5**).

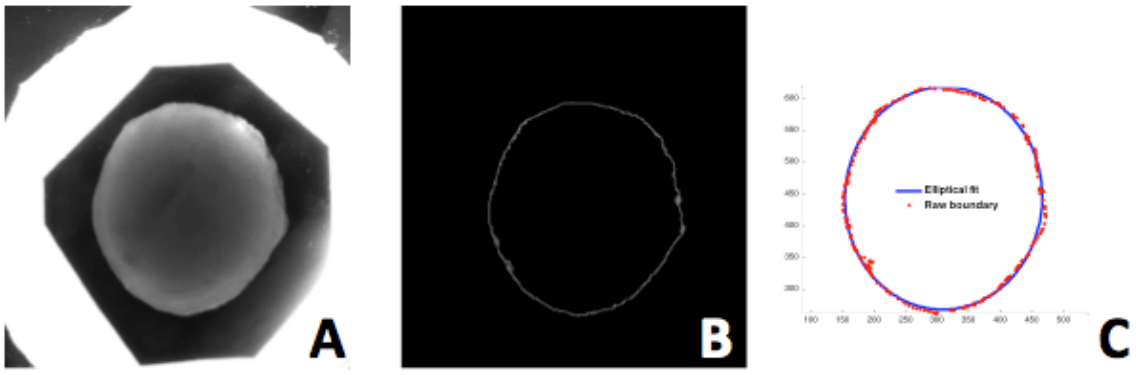

Figure 7.5: Automated edge segmentation of specimen during compression. (**A**) Grayscale images are captured by the digital video camera. (**B**) The edge of the specimen is segmented based on thresholds of the contrast. (**C**) The segmented edge (dots) is fitted to an ellipse during post-processing (solid line).

The major (r_a) and minor (r_b) radii of the ellipse are used to calculate the eccentricity, which is given by equation (7.1):

$$e = \sqrt{1 - {}^{r_a}/_{r_b}} \tag{7.1}$$

where $e = 0$ indicates a perfect circle. Changes in the eccentricity as the sample is being compressed suggest the presence of planar anisotropy, provided that the specimen maintains an elliptical shape (**Figure 7.6**).

We validated our device by testing cardiac adipose tissue. The adipose tissue was obtained at a local abattoir (Holifield Farms, Covington, GA) from porcine heart. A circular sample of the tissue was removed using a 10 mm biopsy punch. The tissue was approximately 3 mm in thickness. For the control, we tested a similar thickness circular piece of isotropic Buna-N rubber removed using the same biopsy punch.

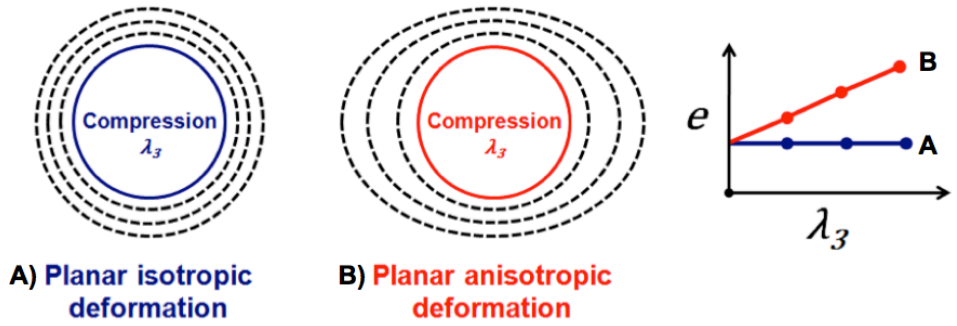

Figure 7.6: Analysis of the eccentricity. (**A**) If the material is isotropic, the eccentricity of the specimen remains constant during loading. (**B**) Otherwise, the eccentricity increases with loading. The principle stretches of an ellipse correspond to its major and minor radii.

Results

The adipose tissue exhibits non-linear loading and unloading behaviors indicative of soft biological tissues (**Figure 7.7A**). The compressive stress is calculated directly from measurements of the force and area (without the need to invoke incompressibility, since the compressed area is measured).

The eccentricity of the isotropic rubber does not change as it is being compressed (**Figure 7.7B**). This suggests equal expansion of the rubber in the principle directions confirming isotropy in the compressed plane. However, in the adipose tissue, the eccentricity increases under compression indicating more expansion in one direction. Both the rubber and adipose tissue maintained a continuous elliptical shape throughout testing.

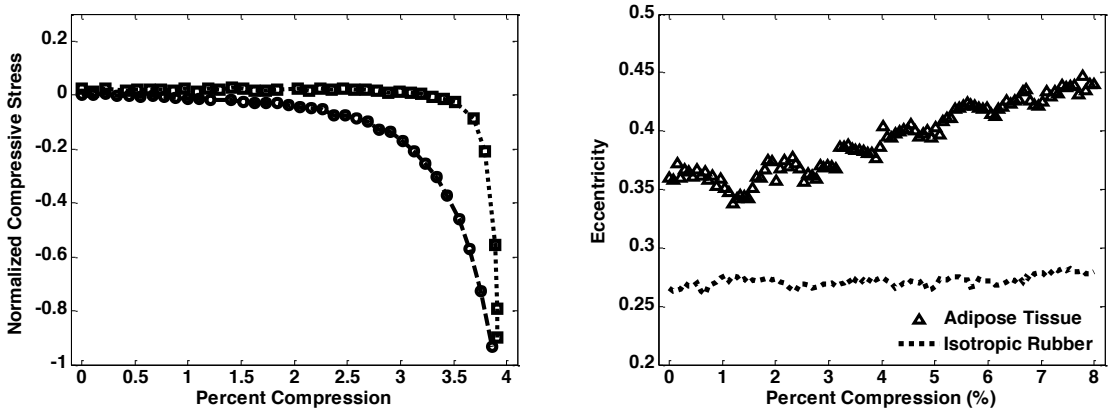

Figure 7.7: Mechanical measurements from the compression tester. (**A**) Stress-strain behavior of adipose tissue is calculated directly from the cross-sectional area and force. (**B**) The eccentricity increases during loading for the adipose tissue (triangle markers) but remains constant for the isotropic rubber (dots).

Discussion

We have presented the development of a novel uniaxial compression tester that is capable of detecting limited planar anisotropic behavior of the compressed sample. Initial validation of the device is performed using soft cardiac adipose tissue and isotropic rubber as the control. The adipose tissue exhibited anisotropic behavior as characterized by an increase in the eccentricity of the sample during compression. The eccentric of the rubber did not change, confirming isotropy. This device provides additional information on the mechanical behavior of the specimen compared to traditional uniaxial tests. However, if anisotropic behaviors are detected, additional tests are needed to characterize the material properties, including mechanical tests in the orthogonal directions and in shear.

References

1. Grytz, R. and G. Meschke, *Constitutive modeling of crimped collagen fibrils in soft tissues.* Journal of the Mechanical Behavior of Biomedical Materials, 2009. **2**(5): p. 522-533.

2. Cacho, F., et al., *A constitutive model for fibrous tissues considering collagen fiber crimp.* International Journal of Non-Linear Mechanics, 2007. **42**(2): p. 391-402.

3. Hill, M.R., et al., *A theoretical and non-destructive experimental approach for direct inclusion of measured collagen orientation and recruitment into mechanical models of the artery wall.* Journal of biomechanics, 2012.

4. Ni Annaidh, A., et al., *Automated estimation of collagen fibre dispersion in the dermis and its contribution to the anisotropic behaviour of skin.* Annals of biomedical engineering, 2012: p. 1-13.

5. Demer, L.L. and F. Yin, *Passive biaxial mechanical properties of isolated canine myocardium.* The Journal of physiology, 1983. **339**(1): p. 615-630.

6. Yin, F.C.P., et al., *Quantification of the mechanical properties of noncontracting canine myocardium under simultaneous biaxial loading.* Journal of biomechanics, 1987. **20**(6): p. 577-589.

7. Bing, O.H.L., et al., *Mechanical properties of rat cardiac muscle during experimental hypertrophy.* Circulation research, 1971. **28**(2): p. 234-245.

8. Novak, V.P., F. Yin, and J. Humphrey, *Regional mechanical properties of passive myocardium.* Journal of biomechanics, 1994. **27**(4): p. 403-412.

9. Jobsis, P.D., et al., *The visceral pericardium: macromolecular structure and contribution to passive mechanical properties of the left ventricle.* American Journal of Physiology-Heart and Circulatory Physiology, 2007. **293**(6): p. H3379-H3387.

10. Kang, T., J. Humphrey, and F. Yin, *Comparison of biaxial mechanical properties of excised endocardium and epicardium.* American Journal of Physiology-Heart and Circulatory Physiology, 1996. **270**(6): p. H2169-H2176.

11. Humphrey, J., R. Strumpf, and F. Yin, *Biaxial mechanical behavior of excised ventricular epicardium.* American Journal of Physiology-Heart and Circulatory Physiology, 1990. **259**(1): p. H101-H108.

12. Miller, K. and K. Chinzei, *Constitutive modelling of brain tissue: experiment and theory.* Journal of biomechanics, 1997. **30**(11-12): p. 1115-1121.

13. Miller, K., *Method of testing very soft biological tissues in compression.* Journal of biomechanics, 2005. **38**(1): p. 153-158.

14. Farshad, M., et al., *Material characterization of the pig kidney in relation with the biomechanical analysis of renal trauma.* Journal of biomechanics, 1999. **32**(4): p. 417-425.

15. Krouskop, T.A., et al., *Elastic moduli of breast and prostate tissues under compression.* Ultrasonic imaging, 1998. **20**(4): p. 260-274.

16. Bruck, H., et al., *Digital image correlation using Newton-Raphson method of partial differential correction.* Experimental mechanics, 1989. **29**(3): p. 261-267.

17. Peters, W. and W. Ranson, *Digital imaging techniques in experimental stress analysis.* Optical Engineering, 1982. **21**(3): p. 213427-213427-.